THEORETICAL ASPECTS OF ULTRA-COLD FERMIONS IN THE PRESENCE OF ARTIFICIAL SPIN-ORBIT COUPLING

A Thesis
Presented to
The Academic Faculty

by

Doga Murat Kurkcuoglu

In Partial Fulfillment
of the Requirements for the Degree
Doctor of Philosophy in the
School of Physics

Georgia Institute of Technology
August 2015

Copyright © 2015 by Doga Murat Kurkcuoglu

THEORETICAL ASPECTS OF ULTRA-COLD FERMIONS IN THE PRESENCE OF ARTIFICIAL SPIN-ORBIT COUPLING

Approved by:

Professor Carlos Sá de Melo, Advisor
School of Physics
Georgia Institute of Technology

Professor Michael Chapman
School of Physics
Georgia Institute of Technology

Professor Shina Tan
School of Physics
Georgia Institute of Technology

Professor Jean Bellissard
School of Mathematics & Physics
Georgia Institute of Technology

Professor Markus Kindermann
School of Physics
Georgia Institute of Technology

Date Approved: 05/15/2015

To Derya,

For everything,

And my Family,

For showing me the importance to pursue imagination.

PREFACE

The interest in ultra-cold fermions has consistently grown over the years, in particular because of the direct connection to condensed matter physics, and the ability to control, essentially at the turn of a knob, many properties of the system including its geometry, particle densities and atom-atom interactions. These knobs act as tools used to investigate fermionic physics, but these tools are not readily available in condensed matter, thus making ultra-cold fermions ideal simulators of fundamental physics involving fermions. The use of these tools is particularly suited to reach regimes that are simply not possible in condensed matter physics.

One of the big success stories of ultra-cold fermions as simulators of condensed matter phenomena was the study of the evolution from Bardeen-Cooper-Schrieffer (BCS) to Bose-Einstein-Condensate (BEC) superfluidity by tuning atom-atom interactions, which was performed last decade. The tool that made these studies possible was the existence of tunable scattering resonances between fermionic atoms, the so-called Feshbach resonances. In this decade, another important research discovery was achieved via the experimental realization of a new tool, the so-called artificial spin-orbit coupling. The creation of synthetic spin-orbit coupling allowed for the simulation of the effects of real spin-orbit coupling in electronic systems, with the advantage that the artificial spin-orbit coupling itself can be widely tuned in cold atoms. This tunability again facilitates reaching regimes that are just not easily accessible or impossible to reach in condensed matter systems. The engineering of artificial spin-orbit coupling was realized first in bosonic systems, but very recently the same effect was achieved for fermionic atoms.

In this thesis, I investigate the combined effects of the two aforementioned tools,

artificial spin-orbit coupling and atom-atom interactions, on ultra-cold Fermi atoms. By taking advantage of the experimental tunability of these tools, I study a few theoretical aspects of ultra-cold fermions in the presence of artificial spin-orbit coupling. The first aspect covers the formation of two-body bound states for fermions with two relevant hyperfine states, and the second aspect covers spectroscopic and thermodynamic properties of fermions with three relevant hyperfine states, as well as the emergence of superfluidity.

ACKNOWLEDGEMENTS

There are many people that deserves acknowledgement during my PhD journey here in Georgia Tech, however, when one individiual is included, list grows exponentially. Thus, I am going to keep the list as short as I can, and apply a "mean field" approximation to my thank list around School of Physics.

First, I would like to thank my PhD advisor Carlos Sá de Melo for his years of continual support, excellent guiding as well as his patient and friendly attitude which motivated me in hard times. His expertise in both many-body theory and experiment, and the ability to merge these two disciplines when needed was extremely helpful and have broadened my physics perspective. I thank Shina Tan, Kurt Wiesenfeld, Roman Grigoriev, Alex Kuzmich, Michael Pustilnik and Carlos Sá de Melo for their excellent teaching throughout my PhD journey in Georgia Institute of Technology. I have also learned a lot from personal discussions with Shina Tan, Predrag Cvitanovic throughout the years. I thank my group members Li Han and Kangjun Seo for their valuable collaborations. I also thank ARO for their support.

I would like to thank many people in Atlanta to make my life enjoyable during my Ph.D. program, thanks to Atalay Atasu, Maya Cakmak, Jeroen Devreese, Scott Douglas, Evren Gul, Serife Tol Gul, Serhat Gul, Adam Kamor, Altug Kasali, Alex Lesov, Chris Marcotte, Arkadas Ozakin, Can Ozuretmen, Hakan Toreyin, Enya Vermeyen, Murat Yildirim.

I would like to specially thank Turgay Uzer for his support and his friendship over the years. I express my other special thanks to Zikri Altun for helping me to follow my dreams.

The most special thanks go to my wife Derya Senlik Kurkcuoglu, for everything.

TABLE OF CONTENTS

LIST OF FIGURES

SUMMARY

In this thesis I present a few theoretical aspects of ultra-cold fermions in the presence of artificial spin-orbit coupling, which are of direct experimental relevance. The first aspect investigated is the formation of two-body bound states of fermions when artificial spin-orbit coupling and artificial Zeeman fields are present. These bound-states are analyzed for two-hyperfine-state fermions in free space and in a harmonically confining potential. The second aspect explored is the study of spectroscopic and thermodynamic properties of three-hyperfine-state fermions. These properties are investigated as a function of spin-orbit coupling and Zeeman fields for non-interacting atoms, but when atom-atom interactions are also included, the many-body system consisting of three-hyperfine-state fermions can exhibit exotic superfluid phases.

CHAPTER I

INTRODUCTION

My main goal in this thesis is to present a discussion of the effects of artificial spin-orbit coupling and Zeeman fields in fermionic ultra-cold atoms. Part of the work described here is inspired by the experimental realization of artificial spin-orbit coupling (SOC) in the fermionic isotope ^{40}K using a Raman technique [1]. The word artificial is explicit here, because the emergent spin-orbit coupling is not due to relativistic effects, but rather due to some clever coupling of center of mass of the atoms to light fields via Raman processes that connect different hyperfine states of the atom. These atoms (^{40}K) have several hyperfine states that can be trapped in a light field using optical techniques. Once ^{40}K atoms in different hyperfine states are trapped, it is possible to control atom-atom interactions using scattering resonances, the so-called Feshbach resonances [2]. The external control of interactions using scattering resonaces lead to the formation of large diatomic molecules K_2, also known as Feshbach molecules. These molecules (paired fermions) can form a superfluid state at sufficiently low temperatures [3].

I discuss in the introduction (chapter II) some general aspects of spin-orbit coupling, and then I particularize to the case of artificial spin-orbit coupling created experimentally in ^{40}K. Then, in chapters II and III, I discuss the effects of artificial spin-orbit coupling and Zeeman fields during the formation of Feshbach molecules, when atom-atom interactions are changed. The results obtained are in good agreement with recent experiments [1] involving two-hyperfine states of fermionic ^{40}K. In chapter IV, I investigate the effects of artificial spin-orbit coupling and Zeeman fields in three-hyperfine states of fermionic atoms, first when atom-atom interactions are

negligible, and then when atom-atom interactions are present.

1.1 Generic aspects of spin-orbit coupling

Ultra-cold atomic gases are extremely versatile systems that can be controlled with great precision. They can be composed of bosons (particles with integer spin) or fermions (particles with half-integer spin). And, similarly to electron gases, atomic gases can be confined in a variety of environments, including harmonic potentials and crystalline lattices. Furthermore, atom-atom interactions can be controlled, by modifying atomic collisions, to mimic real solid-state systems, but with the added control of interactions, which is not possible in standard condensed matter systems. Using these tools, many experimental groups [4] were able to explore the fundamental quantum physics of several standard condensed-matter phenomena, including superfluidity, quantum magnetism and insulating behavior.

However, exploring some of the remaining uncharted territory in condensed-matter physics using cold atomic gases will require additional tools. One of the tools that was missing from the toolbox until recently is the existence of controllable artificial spin-orbit coupling, which was first created in bosonic atoms [5] and later with fermionic atoms [1, 6]. The artificial spin-orbit created in these systems involves the coupling between the momentum of the center of mass of a neutral atom and internal hyperfine state of state, which is labeled by the word *spin*.

In order to appreciate this effect in the context of neutral ultra-cold atoms, it is useful to review briefly how real spin-orbit coupling arises for charged particles. Let me consider the simple example of the Hydrogen atom and recall that the motion of electron orbiting the atom's nucleus: the motion is altered by the spin of the electrons owing to the electric field of the nucleus, and this gives rise to the atom's fine structure. Similar effects occur in free electrons moving through electric fields in solids, for example the fields generated by the underlying crystalline lattice.

In the case of the Hydrogen atom, from the point of view of the nucleus, the electron orbits the nucleus. However, from the electron's point of view, the proton orbits the electron and produces a magnetic field that couples with the electron's spin and alters its orbital motion [12]. It is this simple relativistic effect that leads to the internal spin-orbit coupling of atoms. In the case of condensed matter crystalline lattices, if the electron is travelling freely through a group of ions, from the electron's point of view it is the ions that move. The ions' motion generates a magnetic field that couples to the electron's spin. In real solids, the coupling between the electron's spin and its motion is more complex, but the essence of the interaction is the same as that depicted here.

The spin-orbit coupling found in condensed matter materials can take many forms depending on the exact type of crystalline lattice, however there are two very common forms of the magnetic fields, created by distribution of ions, that couple directly to the electron's spin. One of the types is called Rashba spin-orbit field [7]

$$\mathbf{h}_R = v_R \left(\hat{k}_x \mathbf{e}_y - \hat{k}_y \mathbf{e}_x \right), \tag{1.1}$$

and the other is the Dresselhaus spin-orbit field [8]

$$\mathbf{h}_D = v_D \left(\hat{k}_x \mathbf{e}_y + \hat{k}_y \mathbf{e}_x \right), \tag{1.2}$$

where $\hat{k}_x, \hat{k}_y$ are momentum operators, v_R, v_D are characteristic velocities, and $\mathbf{e}_x, \mathbf{e}_y$ are unit vectors along the x and y directions of the crystal.

These types of spin-orbit fields are two-dimensional in nature, and a more general Rasha-Dresselhaus field has the form

$$\mathbf{h}_{RD} = \mathbf{h}_R + \mathbf{h}_D = (v_R + v_D)\, \hat{k}_x \mathbf{e}_y + (v_D - v_R)\, \hat{k}_y \mathbf{e}_x, \tag{1.3}$$

corresponding to a general linear combination of Rashba $\mathbf{h}_R$ and Dresselhaus $\mathbf{h}_D$ fields, where the velocities v_R and v_D are different from each other. A very special

linear combination of these two fields is the equal-Rashba-Dresselhaus (ERD) case

$$\mathbf{h}_{ERD} = v\hat{k}_x \mathbf{e}_y, \tag{1.4}$$

where the two velocities v_R and v_D are equal to $v/2$. In this case, the spin-orbit field points along the y direction, and is therefore one-dimensional. As it will be seen shortly, it is this special ERD field that has been generated experimentally in the context of ultra-cold atoms. The Rashba, Dresselhaus, general mixture and equal mixture of Rashba and Dresselhaus fields are shown in Fig. 1.1.

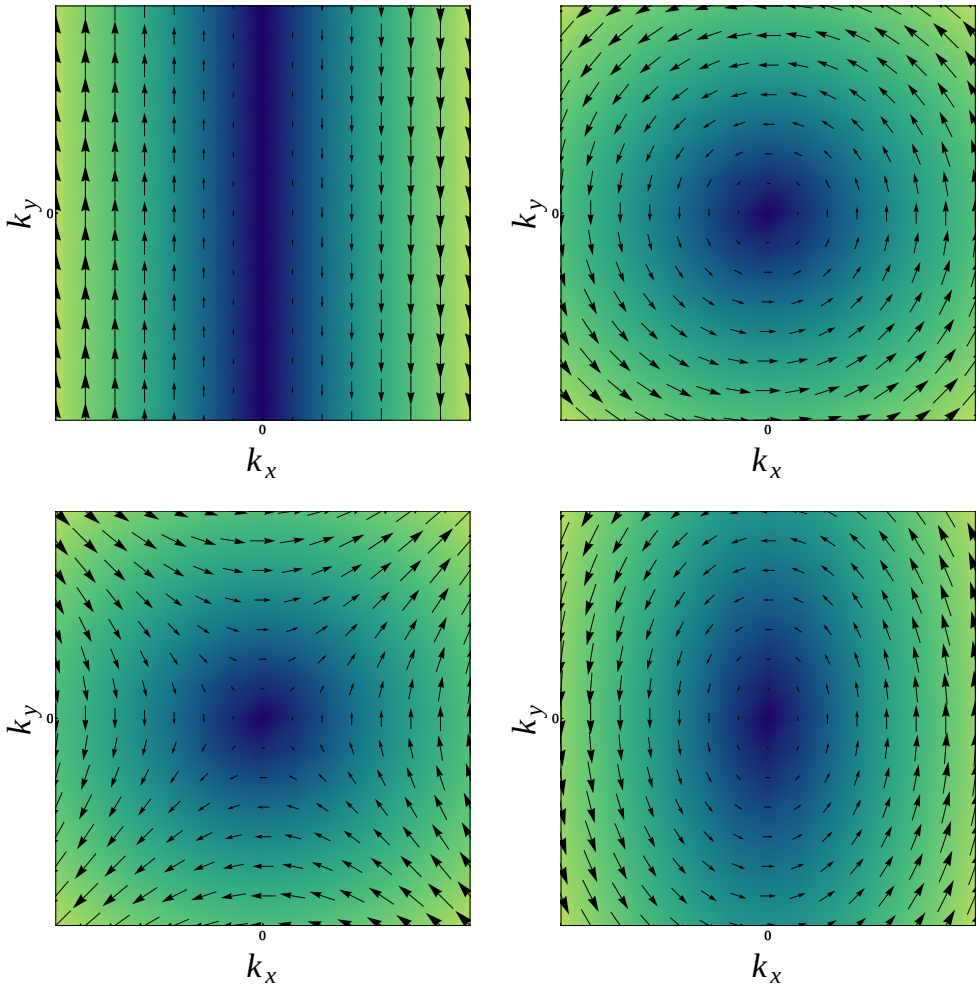

Figure 1.1: Spin-orbit fields for various type of couplings, Equal Rashba-Dresselhaus (top left), Rashba (top right), Dresselhaus (bottom left) and arbitrary mixture of Rashba and Dresselhaus (bottom right).

There has been a revival of interest in spin-orbit coupling phenomena for condensed matter systems related due to the discovery of topological insulators [9, 10]. This revival occured in large due to theoretical proposals showing that Rashba type spin-orbit fields could lead to the existence of Majorana fermions at the surface of some insulating materials. These Majorana fermions are self-adjoint, that is, they are their own anti-particle, and are believed to be topologically protected. This topological protection supposedly can prevent decoherence effects and preserve a very high fidelity of the quantum information carried by such a state, therefore it is a feature highly desirable in a quantum computer.

Having discussed briefly the emergence of spin-orbit fields in the context of condensed matter physics, I will discuss next the creation of artificial spin-orbit coupling in ultra-cold fermions.

1.2 Spin-orbit Coupling in Ultra-Cold Fermions

The creation of artificial spin-orbit coupling in ultra-cold atoms was accomplished first in bosonic atoms ^{87}Rb at the NIST group [5] using Raman processes. The same technique was used by the NIST [1] and Chinese [6] groups to produce artificial spin-orbit coupling in fermionic atoms, more specifically in ^{40}K.

Here, I will describe briefly the Raman process that produces this artificial spin-orbit coupling between the center of mass motion of the atom and its *spin* degree of freedom. There is an important difference between the real spin-orbit coupling and the artificial spin-orbit coupling created in ultra-cold atoms, which is important to emphasize. Artificial spin-orbit coupling for cold atoms is not due to relativistic effects, instead it arises due to the light-induced coupling of the center of mass momentum of the atom and its internal hyperfine states, which I will also call *pseudo-spin* or even more loosely simply *spin* states.

To see how this artificial spin-orbit coupling arises in fermionic atoms, let me

discuss briefly the fermionic isotope ^{40}K, which has a nuclear spin $\mathbf{I}$, with magnitude $I = 4$ and and electronic spin $\mathbf{S}$, with magnitude $S = 1/2$. The total spin of the atom is $\mathbf{F} = \mathbf{I} + \mathbf{S}$, with magnitude $F = 9/2$, where two of its hyperfine states ($|F = 9/2, m_F = -9/2\rangle = |1\rangle$ and $|F = 9/2, m_F = -7/2\rangle = |2\rangle$) are shown in the level diagram of Fig. 1.2a, where a two-photon Raman transition is also indicated by the red and blue lines.

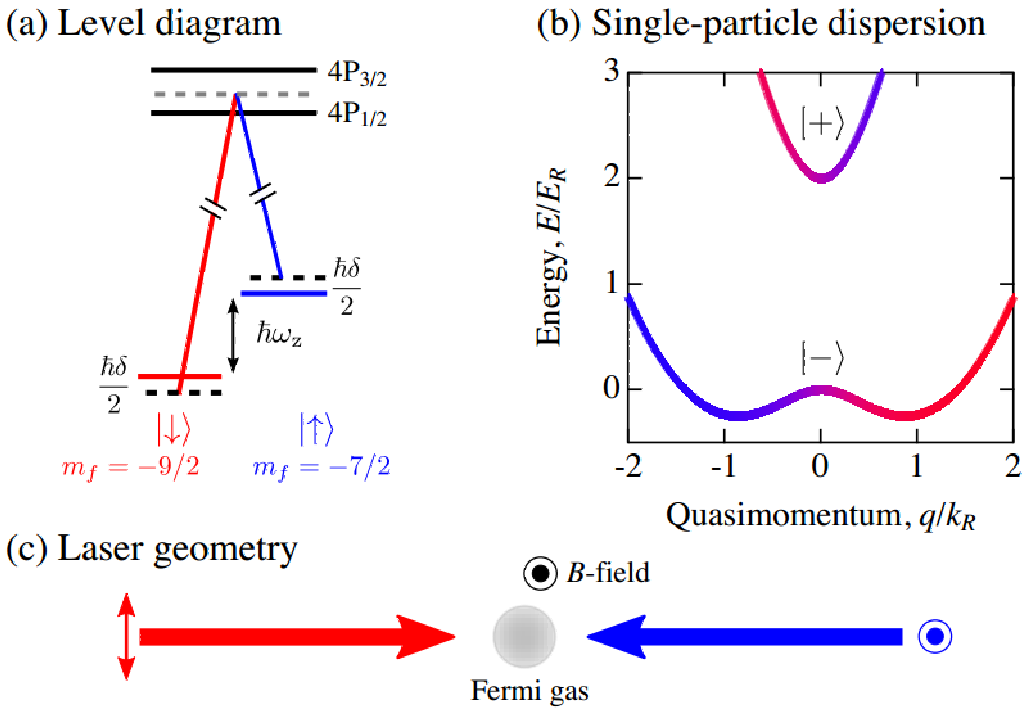

Figure 1.2: The schematic of the NIST experiment. Taken from reference [1].

In what follows, I will just describe physically the light-atom Hamiltonian created by the Raman process shown in Fig. 1.2 and leave out the more detailed mathematical analysis, which can be found in the literature [11, 12]. In the Raman process shown there are two photons involved in the transition between hyperfine states 1 and 2. In the transitions, there is the absorption of one photon and the second photon emerges from induced emission, which implies that a net momentum is transferred to the atom given that the total momentum of the system is conserved. The momentum transferred from the photons to the atom in hyperfine state $|1\rangle$ is $-\mathbf{k_T}$ and that the

momentum transferred to to the atom in hyperfine state $|2\rangle$ is $+\mathbf{k}_T$. This means that the diagonal matrix elements of the light-atom Hamiltonian $\mathbf{H}_{LA}$ matrix are

$$\langle \mathbf{k}-\mathbf{k}_T, 1|\mathbf{H}_{LA}|\mathbf{k}-\mathbf{k}_T, 1\rangle = \frac{(\mathbf{k}-\mathbf{k}_T)^2}{2m} + \delta \tag{1.5}$$

and

$$\langle \mathbf{k}+\mathbf{k}_T, 2|\mathbf{H}_{LA}|\mathbf{k}+\mathbf{k}_T, 2\rangle = \frac{(\mathbf{k}+\mathbf{k}_T)^2}{2m} - \delta, \tag{1.6}$$

where the state $|\mathbf{k}-\mathbf{k}_T, 1\rangle$ describes the Fermi atom in hyperfine state 1 with momentum $\mathbf{k}-\mathbf{k}_T$, and $|\mathbf{k}+\mathbf{k}_T, 2\rangle$ describes the Fermi atom in hyperfine state 2 with momentum $\mathbf{k}+\mathbf{k}_T$. The energy $\delta = \widetilde{\delta}/2$ is the detuning parameter, with $\widetilde{\delta}$ being the energy detuning between the photon energies and the atomic energy difference between the two hyperfine states.

The transition matrix element connecting the states $|\mathbf{k}-\mathbf{k}_T, 1\rangle$ and $|\mathbf{k}+\mathbf{k}_T, 2\rangle$, is defined to be $\Omega = \widetilde{\Omega}/2$, where $\widetilde{\Omega}$ is the conventional Rabi frequency, which is proportional to the product of the two-photon electric field amplitudes. The variable Ω is also called the time-averaged Rabi frequency or sometimes simply the Rabi frequency. Throughout my thesis, I will make the choice of calling Ω the Rabi frequency. This means that the off-diagonal terms of the light-atom Hamitonian matrix are simply

$$\langle \mathbf{k}+\mathbf{k}_T, 2|\mathbf{H}_{LA}|\mathbf{k}-\mathbf{k}_T, 1\rangle = \Omega \tag{1.7}$$

and

$$\langle \mathbf{k}-\mathbf{k}_T, 1|\mathbf{H}_{LA}|\mathbf{k}+\mathbf{k}_T, 2\rangle = \Omega, \tag{1.8}$$

since Ω is real. This means that the light-atom Hamiltonian matrix in the basis of states $\{|\mathbf{k}-\mathbf{k}_T, 1\rangle, |\mathbf{k}+\mathbf{k}_T, 2\rangle\}$ becomes simply

$$\mathbf{H}_{LA} = \begin{pmatrix} \frac{(\mathbf{k}-\mathbf{k}_T)^2}{2m} + \delta & \Omega \\ \Omega & \frac{(\mathbf{k}+\mathbf{k}_T)^2}{2m} - \delta \end{pmatrix}. \tag{1.9}$$

A direct inspection of the diagonal matrix elements of this matrix already reveals the presence of an artificial spin-orbit coupling, since the momentum transfer to the

atom depends on the hyperfine (*spin*) state of the atom. This becomes more explicit by writing

$$\mathbf{H}_{LA} = \left(\frac{\mathbf{k}^2}{2m} + \frac{\mathbf{k}_T^2}{2m}\right)\mathbf{1} + \Omega\boldsymbol{\sigma}_x + \left(\delta - \frac{k_T}{m}k_x\right)\boldsymbol{\sigma}_z, \tag{1.10}$$

where the momentum transfer $\mathbf{k}_T$ is along the direction of the Raman beams taken to be along the x-axis, that is, $\mathbf{k}_T = k_T\mathbf{e}_x$. Here, $\mathbf{1}$ represents the identity matrix, and $\boldsymbol{\sigma}_x$ and $\boldsymbol{\sigma}_z$ represent Pauli matrices along the x and z directions. It is now evident that the momentum dependent term appearing in front of $\boldsymbol{\sigma}_z$ is an artificial spin-orbit coupling.

To make the connection to the real spin-orbit coupling, betwen the electron momentum and its spin, which is found in condensed matter physics, it is useful to perform an SU(2) rotation in spin-space $\boldsymbol{\sigma}_x \to \widetilde{\boldsymbol{\sigma}}_z$; $\boldsymbol{\sigma}_z \to \widetilde{\boldsymbol{\sigma}}_y$; $\boldsymbol{\sigma}_y \to \widetilde{\boldsymbol{\sigma}}_x$; and write the light-atom Hamiltonian in a rotated or *dressed* basis corresponding to appropriate linear combinations of states of the original basis. The resulting light-atom Hamitonian-matrix becomes of the form

$$\widetilde{\mathbf{H}}_{LA} = \left(\frac{\mathbf{k}^2}{2m} + \frac{\mathbf{k}_T^2}{2m}\right)\mathbf{1} + \Omega\widetilde{\boldsymbol{\sigma}}_z + \left(\delta - \frac{k_T}{m}k_x\right)\widetilde{\boldsymbol{\sigma}}_y, \tag{1.11}$$

where the artificial spin-orbit field becomes

$$\mathbf{h}_{ERD} = \frac{k_T}{m}k_x\mathbf{e}_y, \tag{1.12}$$

just like the equal-Rashba-Dresselhaus (ERD) field shown in Eq. (1.4). Notice that the system is simultaneously under the presence of an artificial Zeeman field

$$\mathbf{h}_{Zee} = -\delta\mathbf{e}_y - \Omega\mathbf{e}_z. \tag{1.13}$$

The component along $\mathbf{e}_y$ can be turned off by having a resonant Raman transition, where the detuning parameter $\delta = 0$. The component along $\mathbf{e}_z$ can be reduced to small values, but if $\Omega = 0$, then there is no Raman transition, and the momentum transfer $\mathbf{k}_T$ is also zero.

The eigenvalues of $\widetilde{\mathbf{H}}_{LA}$ can be easily obtained analytically. In the simpler case of zero-detuning, that is, $h_y = -\delta = 0$, the eigenvalues are

$$E_{\pm}(\mathbf{k}) = \epsilon(\mathbf{k}) \pm \sqrt{v^2 k_x^2 + h_z^2}, \tag{1.14}$$

where $v = k_T/m$ and $h_z = -\Omega$ and

$$\epsilon(\mathbf{k}) = \frac{\mathbf{k}^2}{2m} + \frac{\mathbf{k}_T^2}{2m}. \tag{1.15}$$

Notice that, when the Zeeman field and the spin-orbit coupling are turned off ($h_z = v = 0$), the energy dispersions of the fermions are degenerate. But when only the spin-orbit field is turned on, the parabolic bands $\epsilon(\mathbf{k})$ are shifted along the k_x direction, leading to $E_+ = \epsilon(\mathbf{k}) + |vk_x|$ and $E_- = \epsilon(\mathbf{k}) - |vk_x|$. As the Zeeman field h_z is turned on, the energy crossing at zero momentum is split, and the two bands acquire the dispersion shown in Eq. (1.14) and illustrated in Fig. 1.3.

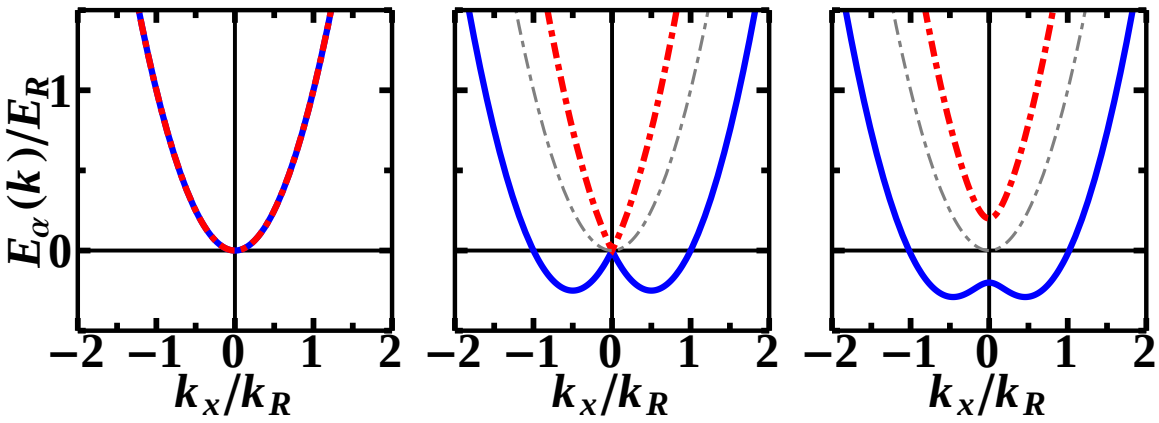

Figure 1.3: Energy dispersions $E_{\pm}(\mathbf{k})$ versus momentum k_x when $v = 0$ and $h_z = 0$ (left panel); $v \neq 0$ and $h_z = 0$ (middle panel); and $v \neq 0$ and $h_z \neq 0$ (right panel). The gray curve in the middle and right panels represents the same degenerate energy dispersion illustrated in the left panel.

Having provided a simple introduction to the field of artificial spin-orbit coupling in the context of ultra-cold atoms, I will present next a brief overview of chapters II, III and IV of my thesis.

1.2.1 Overview of the Thesis

In the remainder of this thesis, I will describe few-body and many-body aspects of ultra-cold fermions in the presence of artificial spin-orbit and Zeeman fields. The problems that I will tackle are motivated by experiments already performed [1], where bounds states of two ultra-cold atoms of ^{40}K were found in the presence of artificial spin-orbit coupling, and by some experiments which are currently in the drawing board to study a more complex system involving three-hyperfine-state fermions [13, 15].

In Chapter II, I describe the emergence of two-body bound states between two-hyperfine-state fermions interacting via s-wave interactions and in the presence of artificial spin-orbit coupling and Zeeman fields. I used a first quantization approach to solve for the eigenvalues associated with bound-states of the resulting Schroedinger equation. The only type of artificial spin-orbit coupling that has been created so far is the ERD-type, but I also analyse the more complex case of Rashba, Dresselhaus or a general linear combination of the two, given that it may be possible to create these types of coupling using a more ellaborate arrangement of Raman beams [14].

In Chapter III, I discuss the emergence of bound states between two-hyperfine state fermions in the presence of an ERD type of spin-orbit coupling in a harmonic potential. The presence of the harmonic potential is an important element of the problem, because ultra-cold atoms are typically harmonically trapped by laser beams, rather than moving in free space. Analytical solutions of the corresponding two-fermion Schroedinger's equation are obtained in simpler situations where only the spin-orbit field is present, and further approximate solutions are obtained when an artificial Zeeman field is present but it is sufficiently small.

While light-atom Hamiltonians for two-hyperfine-state fermions, such as the one described Eq. (1.11, provide the backbone for the analysis performed in Chapters II and III, in Chapter IV, I describe a different system involving three-hyperfine-state

fermions. In this last chapter, I study ultra-cold fermions with three hyperfine states, under the influence of artificial ERD spin-orbit coupling and Zeeman fields. From the light-atom Hamiltonian for three-hyperfine-state fermions, I analyse several spectroscopic properties, such as the resulting energy dispersion relations, Fermi surfaces, momentum distributions and density of states of the system, when atom-atom interactions are neglected. Furthermore, when atom-atom interactions are included, I discuss the emergence superfluid phases and obtain a set of self-consistency relations that can be used to obtain the phase diagram of such exotic three-hyperfine-state superfluid.

CHAPTER II

TWO-BODY BOUND STATES IN THE PRESENCE OF ARTIFICIAL SPIN-ORBIT COUPLING

2.1 Introduction

In chapter I, I gave a brief introduction to the creation of artificial spin-orbit coupling (SOC) for non-interacting Fermi atoms with two relevant hyperfine states. The Hamiltonian for light-atom interactions in the presence of artificial spin-orbit and Zeeman fields was explicitly given in Eq. (1.9). In that same chapter, I also discussed a few different types of SOC in the context of fermions with two-internal spin states.

In this chapter, I will discuss the emergence of two-body bound states between two Fermi atoms in the presence of spin-orbit coupling and Zeeman fields. The fermions are assumed to have only two internal states and to have attractive contact (zero-ranged) interactions. For such a system, I will describe the bound-state energies and the effective mass of the bound-states as a function of spin-orbit and Zeeman fields, and how these properties affect the Bose-Einstein condensation of such molecular bound states. The natural momentum scale is the recoil momentum k_R, which is determined by the wavelength of the two counter-propagating Raman beams, and the natural energy scale is the recoil energy $E_R = k_R^2/2m$, where m is the mass of the atom.

In this and in the following chapters, I will, on occasions, either use the word *pseudospin* or even more loosely use simply the word *spin* when referring to hyperfine states of an atom. Thus, when I refer to a *pseudospin*-1/2 or *spin*-1/2 fermions in the context of cold atoms, I will have in mind fermions with two relevant hyperfine states.

Currently, the only type of spin-orbit coupling that has been created artificially in the context of cold atoms it the type equal-Rashba-Dresselhaus (ERD), realized both in bosonic [5] and fermionic [1, 6]. However, more general optical methods for constructing Rashba or Dresselhaus spin-orbit couplings have been proposed [14]. With that in mind, I will discuss the case of an arbitrary mixture of Rashba and Dresselhaus terms, which can be particularized to Rashba-only, Dresselhaus-only and equal-Rashba-Dresselaus (ERD).

In the context of ultra-cold atoms two-body bound states emerge, when scattering resonances, the so-called Feshbach resonances, are used to change the scattering length of colliding atoms. These resonances arise due to the dependence of the interatomic potentials on the hyperfine states of the atoms, and can be tuned via an external real magnetic field that couples to the hyperfine states of the atoms. When only two hyperfine states are relevant, the atom-atom interactions can be tuned via the external magnetic field and the s-wave scattering length can change dramatically. When the scattering length is tuned to positive values then two-body bound states emerge. These states are also called Feshbach molecules due to the use Feshbach resonances to produce them.

Having provided a brief introduction, I will discuss next the two-body Hamiltonian in the presence of spin-orbit and Zeeman fields when s-wave contact interactions are considered.

2.2 Two-particle Hamiltonian

To address the formation of two-body bound states (Feshbach molecules) in the presence of artificial spin-orbit coupling and Zeemans fields, I start from the Hamiltonian matrix for two non-interacting fermions

$$\mathbf{H}_0 = \mathbf{H}_0^{(1)} + \mathbf{H}_0^{(2)}, \tag{2.1}$$

where $\mathbf{H}_0^{(j)}$ represents the Hamiltonian matrix for particle j taking the form

$$\mathbf{H}_0^{(j)} = -\frac{\nabla_j^2}{2m}\mathbf{1} + \beta i\partial_{y_j}\boldsymbol{\sigma}_x + \gamma i\partial_{x_j}\boldsymbol{\sigma}_y - h_y\boldsymbol{\sigma}_y - h_z\boldsymbol{\sigma}_z. \tag{2.2}$$

In the expression above, the terms involving the coefficients β and γ represent generic a spin-orbit field involving Rashba and Dresselhaus contributions written in real space, while the components $\{h_y, h_z\}$ represent Zeeman fields. Notice that one can define the spin-orbit field

$$\mathbf{h}_{RD} = -\beta i\partial_{y_j}\mathbf{e}_x - \gamma i\partial_{x_j}\mathbf{e}_y = \beta\hat{k}_{y_j}\mathbf{e}_x + \gamma\hat{k}_{x_j}\mathbf{e}_y, \tag{2.3}$$

with $\beta = v_D - v_R$, and $\gamma = v_D + v_R$, where v_R is the Rashba velocity and v_D is the Dresselhaus velocity, as described in chapter I.

In passing, I would like to comment that when both β and γ are non-zero the spin-orbit field $\mathbf{h}_{RD}$ resembles a non-Abelian gauge field. This can be seen by completing the squares of the momentum operator giving

$$\begin{aligned}\mathbf{H}_0^{(j)} = &-\frac{\left(\partial_{x_j}\mathbf{1} - im\gamma\boldsymbol{\sigma}_y\right)^2}{2m} - \frac{\left(\partial_{y_j}\mathbf{1} - im\beta\boldsymbol{\sigma}_x\right)^2}{2m} + ... \\ &... - \frac{\partial_{z_j}^2}{2m}\mathbf{1} - \frac{1}{2}m\gamma^2\mathbf{1} - \frac{1}{2}m\beta^2\mathbf{1} - h_y\boldsymbol{\sigma}_y - h_z\boldsymbol{\sigma}_z,\end{aligned} \tag{2.4}$$

where it can be noticed that the terms $\mathbf{A}_x = -im\gamma\boldsymbol{\sigma}_y$ and $\mathbf{A}_y = -im\beta\boldsymbol{\sigma}_x$ resemble the components of a gauge field $\mathbf{A} = (\mathbf{A}_x, \mathbf{A}_y, 0)$, but since the matrices $\boldsymbol{\sigma}_x$ and $\boldsymbol{\sigma}_y$ are non-commutative, the gauge field $\mathbf{A}$ is non-Abelian.

For calculational purposes, I will use the form of the single-particle Hamiltonian matrix defined in Eq. (2.2), and from them construct the two-particle Hamiltonian matrix

$$\begin{aligned}\mathbf{H}_2 = &-\frac{\nabla_1^2}{2m}\mathbf{1}\otimes\mathbf{1} + i\gamma\partial_{x_1}\boldsymbol{\sigma}_y\otimes\mathbf{1} + i\beta\partial_{y_1}\boldsymbol{\sigma}_x\otimes\mathbf{1} - h_z\sigma_z\otimes\mathbf{1} - h_y\boldsymbol{\sigma}_y\otimes\mathbf{1} + ... \\ &-\frac{\nabla_2^2}{2m}\mathbf{1}\otimes\mathbf{1} + i\gamma\partial_{x_2}\mathbf{1}\otimes\boldsymbol{\sigma}_y + i\beta\partial_{y_1}\mathbf{1}\otimes\boldsymbol{\sigma}_x - h_z\mathbf{1}\otimes\boldsymbol{\sigma}_z - h_y\mathbf{1}\otimes\boldsymbol{\sigma}_y,\end{aligned} \tag{2.5}$$

where the symbol $\otimes$ indicate Kronecker direct products, which are explicitly given in Appendix I.

The Hamiltonian matrix for two non-interacting fermions becomes

$$\begin{pmatrix} \hat{T}-2h_z & ih_y+\beta i\partial_{y_2}+\gamma\partial_{x_2} & ih_y+\beta i\partial_{y_1}+\gamma\partial_{x_1} & 0 \\ -ih_y+\beta i\partial_{y_2}-\gamma\partial_{x_2} & \hat{T} & 0 & ih_y+\beta i\partial_{y_1}+\gamma\partial_{x_1} \\ -ih_y+\beta i\partial_{y_1}-\gamma\partial_{x_1} & 0 & \hat{T} & ih_y+\gamma\partial_{x_2}+\beta i\partial_{y_2} \\ 0 & -ih_y+\beta i\partial_{y_1}-\gamma\partial_{x_1} & -ih_y-\gamma\partial_{x_2}+\beta i\partial_{y_2} & \hat{T}+2h_z \end{pmatrix} \tag{2.6}$$

with the kinetic energy operator defined as

$$\hat{T} = -\frac{\nabla_1^2}{2m} - \frac{\nabla_2^2}{2m}. \tag{2.7}$$

When a zero-ranged attractive s-wave interaction $H_I = -g\delta(\mathbf{r}_1 - \mathbf{r}_2)\delta_{s,-s}$ between fermions with opposite *spins* is added to the Hamiltonian matrix in Eq. (2.1), it acquires the two-particle extended matrix form

$$\mathbf{H}_I = -\frac{g}{\sqrt{2}}\delta_{1,2}\begin{pmatrix} 0 & 0 & 0 & 0 \\ 0 & -1 & 1 & 0 \\ 0 & 1 & -1 & 0 \\ 0 & 0 & 0 & 0 \end{pmatrix}. \tag{2.8}$$

The abbreviation $\delta_{1,2} \equiv \delta(\mathbf{r_1} - \mathbf{r_2})$ is used to represent the contact interaction. The bare coupling constant g can be expressed in terms of the experimentally relevant s-wave scattering length [24] via the relation

$$\frac{L^3}{g} = -\frac{m}{4\pi a_s} + \sum_{\mathbf{k}} \frac{1}{2\epsilon_{\mathbf{k}}} \tag{2.9}$$

where L^3 is the volume of free space, $a_s = a_{bg}\left[1 + \Delta B/(B - B_0)\right]$ is three-dimensional s-wave scattering length expressed in terms of the backgroung scattering length, the real magnetic field B, the width ΔB of the Feshbach resonance, and the field B_0 where the resonance is located.

To find the two-body bound state energies, it is necessary to solve the Schrodinger equation

$$\left(\mathbf{H}_2 + \mathbf{H}_I\right)\mathbf{\Psi}(\mathbf{r_1}, \mathbf{r_2}) = E\mathbf{\Psi}(\mathbf{r_1}, \mathbf{r_2}), \tag{2.10}$$

where $\mathbf{\Psi}(\mathbf{r}_1, \mathbf{r}_2)$ is a spinor (four-component vector wave function) in real space with components

$$\mathbf{\Psi}^\dagger(\mathbf{r_1}, \mathbf{r_2}) = \left[\psi^*_{\uparrow\uparrow}(\mathbf{r_1}, \mathbf{r_2}), \psi^*_{\uparrow\downarrow}(\mathbf{r_1}, \mathbf{r_2}), \psi^*_{\downarrow\uparrow}(\mathbf{r_1}, \mathbf{r_2}), \psi^*_{\downarrow\downarrow}(\mathbf{r_1}, \mathbf{r_2})\right]. \tag{2.11}$$

In each of the components of this spinor, the first *spin* index refers to particle "1", while the second spin index refers to particle "2".

The first step to solve the Schroedinger's equation defined in Eq. (2.10) is to convert the two-particle Hamiltonian matrix $\mathbf{H}_2$ into the momentum space matrix $\widetilde{\mathbf{H}}_2(\mathbf{k}_1, \mathbf{k}_2)$

$$\begin{pmatrix} \epsilon_{\mathbf{k}_1\mathbf{k}_2} - 2h_z & ih_y - \beta k_{y_2} + i\gamma k_{x_2} & ih_y - \beta k_{y_1} + i\gamma k_{x_1} & 0 \\ -ih_y - \beta k_{y_2} - i\gamma k_{x_2} & \epsilon_{\mathbf{k}_1\mathbf{k}_2} & 0 & ih_y - \beta k_{y_1} + i\gamma k_{x_1} \\ -ih_y - \beta k_{y_1} - i\gamma k_{x_1} & 0 & \epsilon_{\mathbf{k}_1\mathbf{k}_2} & ih_y - \beta k_{y_2} + i\gamma k_{x_2} \\ 0 & -ih_y - \beta k_{y_1} - i\gamma k_{x_1} & -ih_y - \beta k_{y_2} - i\gamma k_{x_2} & \epsilon_{\mathbf{k}_1\mathbf{k}_2} + 2h_z \end{pmatrix} \tag{2.12}$$

and at the same time perform the same conversion in the two-particle interaction matrix

$$\widetilde{\mathbf{H}}_I = -\frac{g}{\sqrt{2}} \begin{pmatrix} 0 & 0 & 0 & 0 \\ 0 & -1 & 1 & 0 \\ 0 & 1 & -1 & 0 \\ 0 & 0 & 0 & 0 \end{pmatrix} \frac{1}{L^3} \sum_{\mathbf{k}}. \tag{2.13}$$

The corresponding Fourier-transformed spinor is

$$\mathbf{\Psi}^\dagger(\mathbf{k_1}, \mathbf{k_2}) = \left[\psi^*_{\uparrow\uparrow}(\mathbf{k_1}, \mathbf{k_2}), \psi^*_{\uparrow\downarrow}(\mathbf{k_1}, \mathbf{k_2}), \psi^*_{\downarrow\uparrow}(\mathbf{k_1}, \mathbf{k_2}), \psi^*_{\downarrow\downarrow}(\mathbf{k_1}, \mathbf{k_2})\right], \tag{2.14}$$

whereas the two-particle kinetic energy in Eq. (2.12) is

$$\epsilon_{\mathbf{k}_1\mathbf{k}_2} = \frac{\mathbf{k}_1^2}{2m} + \frac{\mathbf{k}_2^2}{2m}. \tag{2.15}$$

Both the two-particle Hamiltonian for non-interacting particles $\widetilde{\mathbf{H}}_2$ shown in Eq. (2.12) and the interaction Hamiltonian $\widetilde{\mathbf{H}}_I$ in Eq. (2.13) are written in the standard spin-basis $\{|\uparrow,\uparrow\rangle, |\uparrow,\downarrow\rangle, |\downarrow,\uparrow\rangle |\downarrow,\downarrow\rangle\}$ where the first entry (s) in the ket $|s, s'\rangle$ refers to particle 1, and the second entry s' refers to particle 2.

However, to make further progress, it is very convenient to change the basis into two-particle spin-singlet ket $|0,0\rangle$, and two-particle spin-triplet kets $|1,1\rangle$, $|1,0\rangle$, and $|1,-1\rangle$). This is achieved via the unitary matrix

$$\mathbf{U} = \begin{pmatrix} 1 & 0 & 0 & 0 \\ 0 & 1/\sqrt{2} & 1/\sqrt{2} & 0 \\ 0 & 0 & 0 & 1 \\ 0 & 1/\sqrt{2} & -1/\sqrt{2} & 0 \end{pmatrix}, \tag{2.16}$$

which transforms the spinor $\mathbf{\Psi}(\mathbf{k}_1, \mathbf{k}_2)$ into a new spinor in the singlet/triplet basis defined by

$$\mathbf{U}\mathbf{\Psi}(\mathbf{k}_1, \mathbf{k}_2) = \mathbf{\Phi}(\mathbf{k}_1, \mathbf{k}_2) = \begin{pmatrix} \phi_{1,1}(\mathbf{k}_1, \mathbf{k}_2) \\ \phi_{1,0}(\mathbf{k}_1, \mathbf{k}_2) \\ \phi_{1,-1}(\mathbf{k}_1, \mathbf{k}_2) \\ \phi_{0,0}(\mathbf{k}_1, \mathbf{k}_2) \end{pmatrix} \tag{2.17}$$

Notice that singlet/triplet wave functions are connected to the up/down wave functions in the usual way, that is via the symmetric or antisymmetric combination of the products of the up/down wavefunctions.

Additional progress can be made by writing down the wavefunctions of the spinor $\mathbf{\Phi}(\mathbf{k}_1, \mathbf{k}_2)$ as a function of the relative and center of mass momentum of the two particle given respectively by $\mathbf{k} = (\mathbf{k}_1 - \mathbf{k}_2)/2$, and $\mathbf{K} = \mathbf{k}_1 + \mathbf{k}_2$. Such a transformation results in the spinor components

$$\phi_{1,1}(\mathbf{K}/2 + \mathbf{k}, \mathbf{K}/2 - \mathbf{k}) \equiv \phi_{1,1}(\mathbf{k}, \mathbf{K}) = \psi_{\uparrow\uparrow}(\mathbf{k}, \mathbf{K}) \tag{2.18}$$

$$\phi_{1,0}(\mathbf{K}/2 + \mathbf{k}, \mathbf{K}/2 - \mathbf{k}) \equiv \phi_{1,0}(\mathbf{k}, \mathbf{K}) = \frac{1}{\sqrt{2}}\left[\psi_{\uparrow\downarrow}(\mathbf{k}, \mathbf{K}) + \psi_{\downarrow\uparrow}(\mathbf{k}, \mathbf{K})\right] \tag{2.19}$$

$$\phi_{1,-1}(\mathbf{K}/2 + \mathbf{k}, \mathbf{K}/2 - \mathbf{k}) \equiv \phi_{1,-1}(\mathbf{k}, \mathbf{K}) = \psi_{\downarrow\downarrow}(\mathbf{k}, \mathbf{K}) \tag{2.20}$$

$$\phi_{0,0}(\mathbf{K}/2 + \mathbf{k}, \mathbf{K}/2 - \mathbf{k}) \equiv \phi_{0,0}(\mathbf{k}, \mathbf{K}) = \frac{1}{\sqrt{2}}\left[\psi_{\uparrow\downarrow}(\mathbf{k}, \mathbf{K}) - \psi_{\downarrow\uparrow}(\mathbf{k}, \mathbf{K})\right]. \tag{2.21}$$

Next, I apply the unitary matrix $\mathbf{U}$ to the two-particle Hamiltonian matrix $\widetilde{\mathbf{H}}_2(\mathbf{k}_1, \mathbf{k_2})$ to obtain the new Hamiltonian matrix $\mathbf{H}_0(\mathbf{k}_1, \mathbf{k}_2) = \mathbf{U}\widetilde{\mathbf{H}}_2(\mathbf{k}_1, \mathbf{k}_2)\mathbf{U}^\dagger$, which can be

expressed in terms of the relative momentum $\mathbf{k}$ and center of mass momentum $\mathbf{K}$ as

$$\mathbf{H}_0(\mathbf{k},\mathbf{K}) = \begin{pmatrix} \epsilon_{\mathbf{k},\mathbf{K}} - 2h_z & h_{1,2} & 0 & p_{1,2} \\ h_{1,2}^* & \epsilon_{\mathbf{k},\mathbf{K}} & h_{1,2} & 0 \\ 0 & h_{1,2}^* & \epsilon_{\mathbf{k},\mathbf{K}} + 2h_z & -p_{1,2}^* \\ p_{1,2}^* & 0 & -p_{1,2} & \epsilon_{\mathbf{k},\mathbf{K}} \end{pmatrix}. \tag{2.22}$$

The off-diagonal matrix elements in Eq. (2.22) are characterized by the effective fields

$$h_{1,2} = h(\mathbf{k_1}) + h(\mathbf{k_2})/\sqrt{2} = i\gamma K_x/\sqrt{2} - \beta K_y/\sqrt{2} + i\sqrt{2}h_y, \tag{2.23}$$

which involve only the center of mass momentum $\mathbf{K}$, and the additional effective fields

$$p_{1,2} = h(\mathbf{k_1}) - h(\mathbf{k_2})/\sqrt{2} = -i\sqrt{2}\gamma k_x + \sqrt{2}\beta k_y \tag{2.24}$$

that depend only on the relative momentum $\mathbf{k}$. In the expressions above, I used the relation $h(\mathbf{k}_i) = ih_y - \beta k_{y_i} + i\gamma k_{x_i}$ to obtain the final forms of $h_{1,2}$ and $p_{1,2}$. The diagonal terms in Eq. (2.22) contain the two-particle kinetic energies

$$\epsilon_{\mathbf{k},\mathbf{K}} = \epsilon_{\mathbf{k}_1,\mathbf{k}_2} = \mathbf{k}_1^2/2m + \mathbf{k}_2^2/2m = \mathbf{k}^2/m + \mathbf{K}^2/4m. \tag{2.25}$$

The application of the same unitary transformation to the interaction matrix matrix $\widetilde{\mathbf{H}}_I$ leads to

$$\mathbf{H}_I = \mathbf{U}\widetilde{\mathbf{H}}_I\mathbf{U}^\dagger = \begin{pmatrix} 0 & 0 & 0 & 0 \\ 0 & 0 & 0 & 0 \\ 0 & 0 & 0 & 0 \\ 0 & 0 & 0 & -\frac{g}{L^3}\sum_{\mathbf{k}} \end{pmatrix}, \tag{2.26}$$

which explicitly shows that the interactions between the two fermions only occurs in the singlet channel corresponding to the last diagonal entry of the matrix $\mathbf{H}_I$ above.

Now that all the terms of the two-particle Hamiltonian in the presence of spin-orbit coupling, Zeeman fields and attractive contact interactions are written in a useful form, I will discuss next the emerge of two-particle bound states (Feshbach molecules) in the presence of an arbitrary mixture of Rashba and Dresselhaus spin-orbit fields.

2.3 Bound State Energies

In this section, I will discuss the binding energy of two-body bound states (Feshbach molecules) and their dependence on spin-orbit coupling strength, Zeeman field and s-wave scattering length. I will present first the results for the case of equal-Rashba-Dresselhaus (ERD) spin-orbit coupling, which is currently the most relevant type for ultra-cold Fermi atoms. Second, I will analyse the Rashba case, and lastly, I will investigate a more general mixture of Rashba and Dresselhaus spin-orbit fields.

2.3.1 Equal Rashba-Dresselhaus Case

Thus far, the experimentally relevant spin-orbit coupling type for ultracold atoms is the equal Rashba-Dresselhaus (ERD) type. The ERD case corresponds to setting $\gamma = v$ and $\beta = 0$ in the Hamiltonian shown in Eq. (2.22), producing the ERD Hamiltonian

$$\mathbf{H}_0 = \begin{pmatrix} \epsilon_{\mathbf{k},\mathbf{K}} - 2h_z & i\frac{v}{\sqrt{2}}K_x + i\sqrt{2}h_y & 0 & -i\sqrt{2}vk_x \\ -i\sqrt{2}h_y - i\frac{v}{\sqrt{2}}K_x & \epsilon_{\mathbf{k},\mathbf{K}} & i\frac{v}{\sqrt{2}}K_x + i\sqrt{2}h_y & 0 \\ 0 & -i\sqrt{2}h_y - i\frac{v}{\sqrt{2}}K_x & \epsilon_{\mathbf{k},\mathbf{K}} + 2h_z & -i\sqrt{2}vk_x \\ i\sqrt{2}vk_x & 0 & i\sqrt{2}vk_x & \epsilon_{\mathbf{k},\mathbf{K}} \end{pmatrix} \quad (2.27)$$

where the kinetic energies are again $\epsilon_{\mathbf{k},\mathbf{K}} = \mathbf{k}^2/m + \mathbf{K}^2/4m$, and the momentum vectors three-dimensional $\mathbf{k} = (k_x, k_y, k_z)$, and $\mathbf{K} = (K_x, K_y, K_z)$.

Notice that the off-diagonal terms depending on the center of mass momentum variable K_x have also a similar dependence on the Zeeman field h_y. This means that for finite h_y it is always possible to find a value of K_x that makes the off-diagonal term $i\frac{v}{\sqrt{2}}K_x + i\sqrt{2}h_y = 0$. The value is is $K_x = -2h_y/v$ for all the equivalent off-diagonal terms. This property of Hamiltonian will have interesting consequences later on, and I will bring this property into discussion at the appropriate time.

To solve for the two-body bound states, I need to find the corresponding energy

eigenvalues of the Schroedinger's equation

$$(\mathbf{H}_0 + \mathbf{H}_I)\,\mathbf{\Phi}(\mathbf{k},\mathbf{K}) \;\; = \;\; E\mathbf{\Phi}(\mathbf{k},\mathbf{K}), \tag{2.28}$$

where $\mathbf{H}_0$ is Hamiltonian of two non-interacting particles described in Eq. (2.27) and $\mathbf{H}_I$ is the attractive contact interaction with strength g in the singlet channel shown in Eq. (2.26).

Notice that the action of the $\mathbf{H}_I$ on the spinor Φ leads to

$$\mathbf{H}_I\mathbf{\Phi}(\mathbf{k},\mathbf{K}) = \begin{pmatrix} 0 \\ 0 \\ 0 \\ -\frac{g}{L^3}\Sigma_{\mathbf{k}}\phi_{0,0}(\mathbf{k},\mathbf{K}) \end{pmatrix}, \tag{2.29}$$

which shows explicitly that only the singlet channel is included in the attractive interaction term.

In order to obtain a formal solution of Eq. (2.28) and find the bound states eigenvalues E, it is useful to take advantage of the knowledge of eigenvalues of $\mathbf{H}_0$, which give the eigenenergies of two free fermions, that is, these eigenvalues give the free continuum spectrum of two particles. When bound states emerge, their energy E has to be lower the threshold energy of the two free particle continuum. For this purpose, I introduce the unitary matrix $\mathbf{V}$ that diagonalizes $\mathbf{H}_0$, and define the diagonal matrix

$$\mathbf{H}_0' = \mathbf{V}\mathbf{H}_0\mathbf{V}^\dagger \tag{2.30}$$

to describe the eigenergies corresponding to the continuum spectrum of two free particles. The resulting diagonal matrix is

$$\mathbf{H}_0' = \begin{pmatrix} E_{\Downarrow\Downarrow} & 0 & 0 & 0 \\ 0 & E_{\Downarrow\Uparrow} & 0 & 0 \\ 0 & 0 & E_{\Downarrow\Uparrow} & 0 \\ 0 & 0 & 0 & E_{\Uparrow\Uparrow} \end{pmatrix}, \tag{2.31}$$

where the eigenvalues $E_{\alpha\beta}(\mathbf{k},\mathbf{K})$ are labeled by $\{\alpha,\beta\}=\{\Uparrow,\Downarrow\}$ representing a generalized helicity spin. The four eigenvalues are as follows

$$E_{\Downarrow\Downarrow}(\mathbf{k},\mathbf{K}) = \epsilon_{\mathbf{k},\mathbf{K}}+|\mathbf{h}_1-\mathbf{h}_2| = \frac{\mathbf{k}^2}{m}+\frac{\mathbf{K}^2}{4m}+\sqrt{4v^2k_x^2+4h_z^2} \quad (2.32)$$

$$E_{\Downarrow\Uparrow}(\mathbf{k},\mathbf{K}) = \epsilon_{\mathbf{k},\mathbf{K}}+|\mathbf{h}_1+\mathbf{h}_2| = \frac{\mathbf{k}^2}{m}+\frac{\mathbf{K}^2}{4m}+\sqrt{(vK_x+2h_y)^2+4h_z^2} \quad (2.33)$$

$$E_{\Uparrow\Downarrow}(\mathbf{k},\mathbf{K}) = \epsilon_{\mathbf{k},\mathbf{K}}-|\mathbf{h}_1+\mathbf{h}_2| = \frac{\mathbf{k}^2}{m}+\frac{\mathbf{K}^2}{4m}-\sqrt{(vK_x+2h_y)^2+4h_z^2} \quad (2.34)$$

$$E_{\Uparrow\Uparrow}(\mathbf{k},\mathbf{K}) = \epsilon_{\mathbf{k},\mathbf{K}}-|\mathbf{h}_1-\mathbf{h}_2| = \frac{\mathbf{k}^2}{m}+\frac{\mathbf{K}^2}{4m}-\sqrt{4v^2k_x^2+4h_z^2}, \quad (2.35)$$

where $\mathbf{h}_i$ is the effective field experienced by particle i. For the ERD case, these fields are $\mathbf{h}_1=(h_y+vk_{x_1})\mathbf{e}_y+h_z\mathbf{e}_z$ and $\mathbf{h}_2=(h_y+vk_{x_2})\mathbf{e}_y+h_z\mathbf{e}_z$. Let me remind the reader that h_y represents the detuning, and h_z represents the Rabi frequency in the starting *spin* basis that used in this chapter. Also it is important to notice that the labelling of the eigenvalues by $\{\Uparrow,\Downarrow\}$ used above is correct only when $|vK_x+2h_y|\leq|2vk_x|$, such the order of eigenvalues in this case is $E_{\Downarrow\Downarrow}\geq E_{\Downarrow\Uparrow}\geq E_{\Uparrow\Downarrow}\geq E_{\Uparrow\Uparrow}$.

The energy eigenvalues $E_{\alpha\beta}(\mathbf{k},\mathbf{K})$ have parabolic dependences on the relative momentum components k_y and k_z, as well as parabolic behavior for the center of mass momenta momentum components K_y and K_z. However, they present non-trivial dependence as function of either the relative momentum component k_x or as function of the center of mass momentum component K_x. This non-trivial dependence on the relative momentum k_x is plotted and Zeeman fields h_z are plotted in Fig. 2.1 for various choices of parameters.

A formal solution of the Schroedinger's equation

$$(\mathbf{H}_0+\mathbf{H}_I)\,\mathbf{\Phi}(\mathbf{k},\mathbf{K}) = E\mathbf{\Phi}(\mathbf{k},\mathbf{K}) \quad (2.36)$$

can be obtained by rearranging its terms as

$$(\mathbf{H}_0-E\mathbf{1})\,\mathbf{\Phi}(\mathbf{k},\mathbf{K}) = -\mathbf{H}_I\mathbf{\Phi}(\mathbf{k},\mathbf{K}) \quad (2.37)$$

and inverting the relation above to obtain

$$\mathbf{\Phi}(\mathbf{k},\mathbf{K}) = -(\mathbf{H}_0-E\mathbf{1})^{-1}\,\mathbf{H}_I\mathbf{\Phi}(\mathbf{k},\mathbf{K}). \quad (2.38)$$

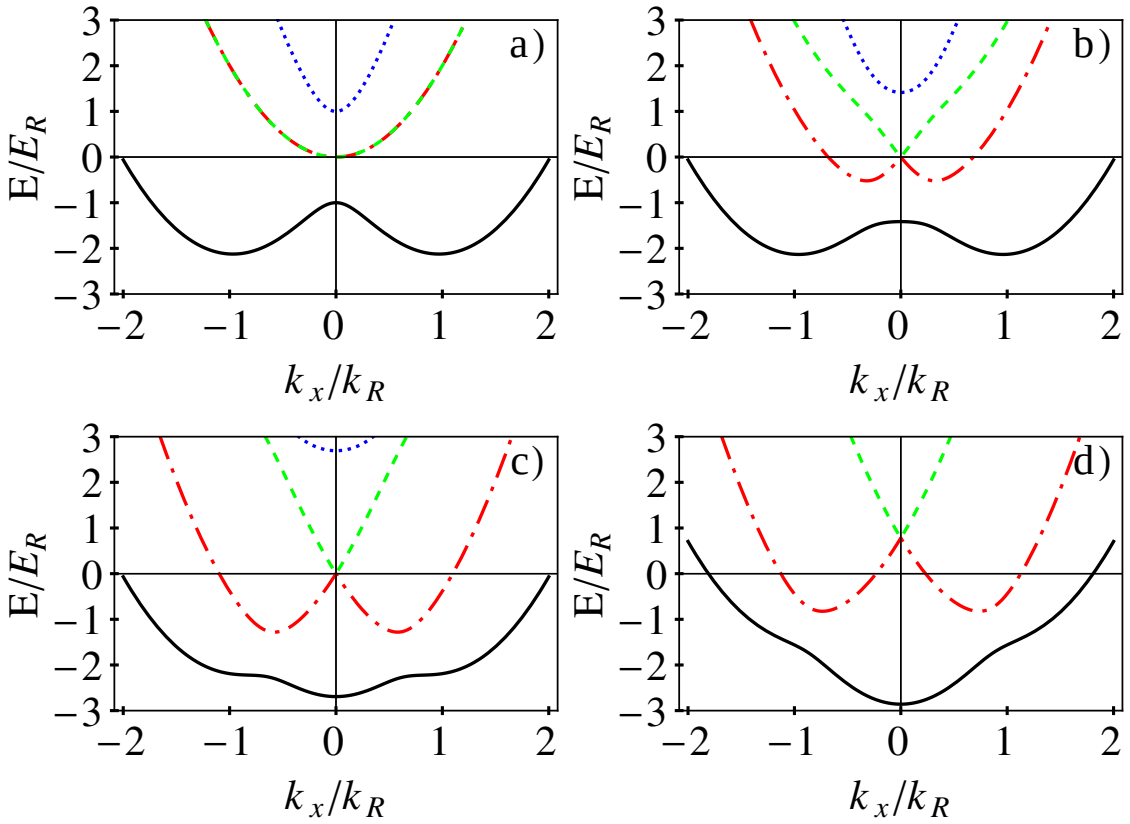

Figure 2.1: Plots of the generalized two-particle helicity bands $E_{\Uparrow\Uparrow}(\mathbf{k},\mathbf{K})$ (black solid), $E_{\Uparrow\Downarrow}(\mathbf{k},\mathbf{K})$ (red dotdashed), $E_{\Downarrow\Uparrow}(\mathbf{k},\mathbf{K})$ (green dashed), and $E_{\Downarrow\Downarrow}(\mathbf{k},\mathbf{K})$ (blue dotted) along the direction of relative momentum $(0,\ 0,\ k_x)$, for ERD spin-orbit coupling $v = k_R/m$, various values of detuning h_y and Raman intensity h_z, and specific values of the center of mass momentum $(0, 0, K_x)$. The parameters used are a) $h_y = 0$, $h_z = 0.5E_R$, and $K_x = 0$; b) $h_y = 0.5E_R$, $h_z = 1.0E_R$, and $K_x = 0$; c) $h_y = 1.25E_R$, $h_z = 0.5E_R$, and $K_x = 0$; and d) $h_y = 0.5E_R$, $h_z = 0.5E_R$, and $K_x = 1.25k_R$. Notice the change in location of the minimum of $E_{\Downarrow\Downarrow}(\mathbf{k},\mathbf{K})$ from finite k_x in a) and b) to $k_x = 0$ in c) and d).

In order to take advantage of the eigenvalues $E_{\alpha\beta}(\mathbf{k},\mathbf{K})$, it is useful to convert the expression the inverse matrix $(\mathbf{H}_0 - E\mathbf{1})^{-1}$ in terms of the adjugate matrix and the determinant of $\mathbf{H}_0 - E\mathbf{1}$. Such standard tranformation leads to the formal solution

$$\mathbf{\Phi}(\mathbf{k},\mathbf{K}) \;=\; -\frac{\mathrm{Adj}\,[\mathbf{H}_0 - E\mathbf{1}]}{\mathrm{Det}\,[\mathbf{H}_0 - E\mathbf{1}]}\mathbf{H}_I\mathbf{\Phi}(\mathbf{k},\mathbf{K}), \tag{2.39}$$

which makes it explicit the eigenvalues $E_{\alpha\beta}(\mathbf{k},\mathbf{K})$, since $\mathrm{Det}\,[\mathbf{H}_0 - E\mathbf{1}]$ is nothing but the characteristic polynomial $(E_{\Uparrow\Uparrow} - E)(E_{\Uparrow\Downarrow} - E)(E_{\Downarrow\Uparrow} - E)(E_{\Downarrow\Downarrow} - E)$.

To gain insight, let me obtain the explicit form of the eigenvalue equation by

setting the center of mass momentum to zero ($\mathbf{K} = \mathbf{0}$), setting both Zeeman fields ($h_y = h_z = 0$), and integrating Eq, (2.40) over relative momenta $\mathbf{k}$. The explicit derivation of the eigenvalue equation below can be found in Appendix II, the result is

$$\frac{1}{g} = \frac{1}{L^3}\sum_{\mathbf{k}} \frac{\epsilon_{\mathbf{k},0} - E}{\left(\epsilon_{\mathbf{k},0} - E\right)^2 - 4v^2k_x^2}. \tag{2.40}$$

Using the relation between the attractive interaction strength g and the s-wave scattering length a_s shown in Eq. (2.9), the eigenvalue equation above can be solved exactly to give

$$E = E_B = -\frac{1}{ma_s^2} - mv^2, \tag{2.41}$$

where E_B is the bound state energy. The derivation is given in Appendix III. This result is not surprising, since the extra term present $-mv^2$ is just the total Galilean boost due to the existence of spin-orbit coupling. This boost is present because the system is Galilean invariant when $h_y = h_z = 0$ and the spin-orbit coupling can be *gauged* away. This means that the binding energy E_{Bin} defined as the energy difference between the bound-state energy E_B and the minimum of the two-particle continuum of free particles $-mv^2$ is simply

$$E_{Bin} = E_B + mv^2 = -\frac{1}{ma_s^2}. \tag{2.42}$$

Having discussed the case of $h_z = h_y = 0$ and $\mathbf{K} = \mathbf{0}$ with finite ERD coupling $v \neq 0$, let me add a non-zero Zeeman field h_z corresponding to a finite Rabi frequency, but still keep $h_y = 0$ and $\mathbf{K} = \mathbf{0}$. Using the same procedure into the formal solution described in Eq. (2.39), I obtain the integral equation

$$\frac{1}{g} = \frac{1}{L^3}\sum_{\mathbf{k}} \frac{\left(E - \epsilon_{\mathbf{k},0}\right)^2 - 4h_z^2}{\left(E - \epsilon_{\mathbf{k},0}\right)^3 - \left(E - \epsilon_{\mathbf{k},0}\right)\left(4v^2k_x^2 + 4h_z^2\right)}. \tag{2.43}$$

Numerical results regarding the bound state energy E_B, the binding energy E_{Bin}, the threshold binding energy $E_{B,th}$ and the threshold scattering length $a_{s,th}$, which emerge by solving Eq. (2.43), are shown in Fig. 2.2.

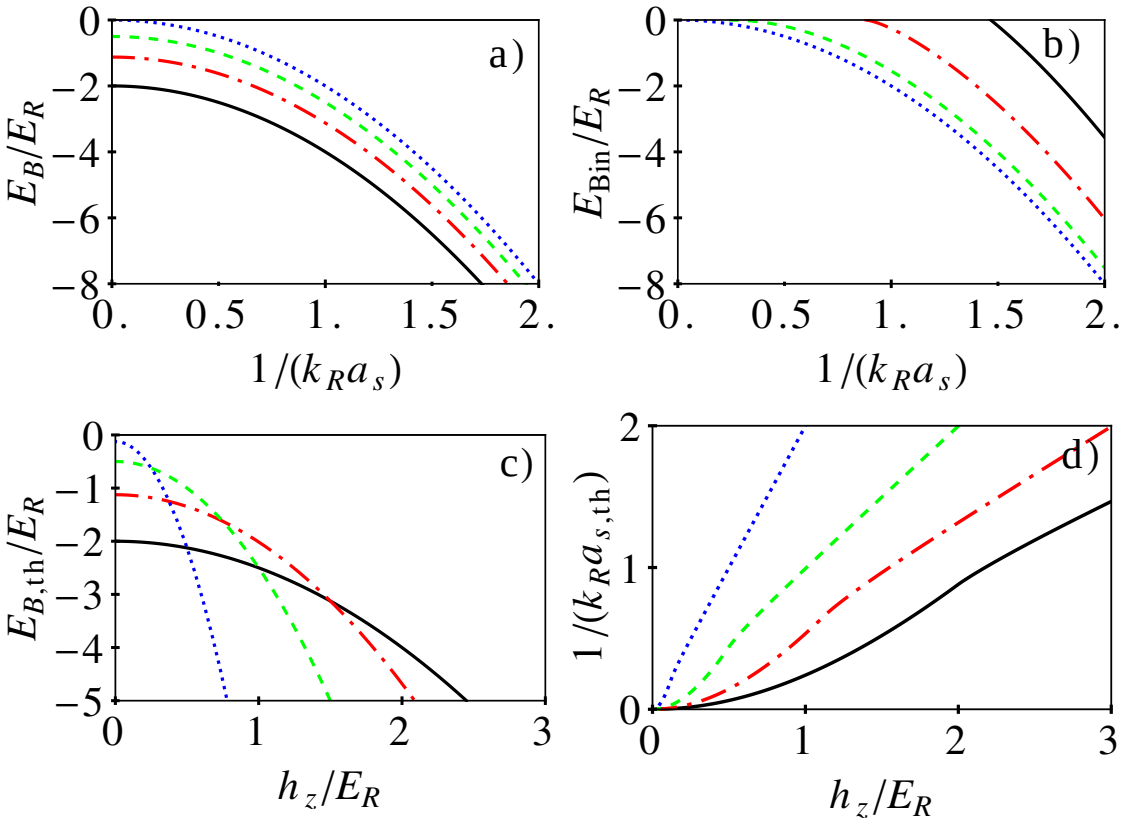

Figure 2.2: Plots of bound state energy E_B/E_R versus $1/(k_R a_s)$ in ERD case with $\mathbf{K} = \mathbf{0}$, $h_z = 0$, $h_y = 0$ (a) for $mv = 0$ (blue dotted), $mv = 0.5k_R$ (red dot-dashed), $mv = 0.75k_R$ (green dashed), $mv = k_R$ (black solid). Binding energy E_{Bin}/E_R versus $1/(k_R a_s)$ with $\mathbf{K} = \mathbf{0}$, $h_y = 0$, $mv = k_R$ are shown in (b) for $h_z = 0$ (blue dotted), $h_z = E_R$ (green dashed), $h_z = 2E_R$ (red dot-dashed), $h_z = 3E_R$ (black solid). Plots of the bound state energy threshold $E_{B,th}/E_R$ and the scattering parameter threshold $1/(k_R a_{s,th})$ versus h_z/E_R are shown in (c) and (d), respectively, for parameters $\mathbf{K} = \mathbf{0}$ and $h_y = 0$ with $mv = 0.25k_R$ (blue dotted), $mv = 0.5k_R$ (red dot-dashed), $mv = 0.75k_R$ (green dashed), $mv = k_R$ (black solid)

In Fig. 2.2a, I show plots of the bound state energy E_B, solution to Eq. (2.43), in units of the recoil energy E_R versus the scattering parameter $1/(k_R a_s)$. The parameters used in Fig. 2.2a, are $\mathbf{K} = \mathbf{0}$, $h_z = 0$, $h_y = 0$, with the different curves corresponding to the following values of the spin-orbit coupling parameter $mv = 0$ (blue dotted), $mv = 0.5k_R$ (red dot-dashed), $mv = 0.75k_R$ (green dashed), $mv = k_R$ (black solid). These curves just show the unit shift of the bound state energy by the amount of $-mv^2$. All these curves collapse into the binding energy curve E_{Bin}/E_R

shown in Fig. 2.2b corresponding to the for $h_z = 0$ (blue dotted), because the minimum of the free two-particle continuum is substracted.

In Fig. 2.2b, I show plots of the the binding energy curve E_{Bin}/E_R versus the scattering parameter $1/(k_R a_s)$, where the minimum of the free two-particle continuum is substracted. The binding energy measures how much energy is gained to form a two-body bound state in comparison to the energy of two free particles. The parameters used in Fig. 2.2b are $\mathbf{K} = \mathbf{0}$, $h_y = 0$, $mv = k_R$ with the different curves corresponding to the following values of the Zeeman field $h_z = 0$ (blue dotted), $h_z = E_R$ (green dashed), $h_z = 2E_R$ (red dot-dashed), $h_z = 3E_R$ (black solid). Notice that as the Zeeman field h_z is increased it becomes more difficult to form two-body bound states in the presence of singlet s-wave attractive interactions, thus requiring a stronger attraction, that is, larger scattering parameter $1/(k_R a_s)$ for fermions to bind.

In Fig. 2.2c, I show plots of the bound state energy threshold $E_{B,th}$ in unit of E_R versus the Zeeman field h_z also in units of E_R. The parameters used in this figure are $\mathbf{K} = \mathbf{0}$ and $h_y = 0$, with different curves corresponding to $mv = 0.25k_R$ (blue dotted), $mv = 0.5k_R$ (red dot-dashed), $mv = 0.75k_R$ (green dashed), $mv = k_R$ (black solid). These plots reveal that for fixed spin-orbit coupling parameter mv an increasing Zeeman field tends to make the two-body bound state more difficult to form in the singlet s-wave channel. However, they also reveal that two-body bound state formation is facilitated for fixed h_z and increasing mv. This effect can be understood due to spin-flip capability of the spin-orbit coupling, which counteracts the tendency that the Zeeman field h_z has to align the spins. It is this competition between the Zeeman field h_z and the spin-orbit coupling that leads to substantial changes in the required conditions for the emergence of two-body bound states (Feshbach molecules).

In Fig. 2.2d, I show plots of the the scattering parameter threshold $1/(k_R a_{s,th})$ versus h_z/E_R The parameters used in this figure are $\mathbf{K} = \mathbf{0}$ and $h_y = 0$, with different curves corresponding to $mv = 0.25k_R$ (blue dotted), $mv = 0.5k_R$ (red dot-dashed),

$mv = 0.75k_R$ (green dashed), $mv = k_R$ (black solid). This figure tells again a similar story. The threshold scattering parameter $1/(k_R a_{s,th})$ is an increasing function of h_z/E_R, meaning that it becomes more difficult to form a two-body bound state from singlet s-wave interactions, thus requiring stronger interactions as h_z grows. However, if spin-orbit coupling mv increases, it becomes easier to form these two-body bound states because spin-orbit can always flip spins increasing the singlet component of the spinor wavefunction of the bound-state. I note in passing that $1/(k_R a_{s,th})$ initially grows quadratically with h_z/E_R for $h_z < mv^2$ and then linearly with h_z/E_R for $h_z > mv^2$. This qualitative difference in behavior is due to the fact that the minimum of the lowest band of the two-particle continuum $E_{\Uparrow\Uparrow}(\mathbf{k}, \mathbf{K} = \mathbf{0})$ shifts from $\mathbf{k} \neq 0$ when $h_z < mv^2$ to $\mathbf{k} = \mathbf{0}$ when $h_z > mv^2$. See Fig. (2.1) for this qualitative change in the lowest eigenvalue $E_{\Uparrow\Uparrow}(\mathbf{k}, \mathbf{K} = \mathbf{0})$.

Lastly, the eigenvalue equation for $\mathbf{K} \neq 0$, $h_z \neq 0$ and $h_y \neq 0$ can be obtained from the formal solution described in Eq. (2.39), upon integration over the relative momentum coordinate $\mathbf{k}$, leading to

$$\frac{1}{g} = \frac{1}{L^3} \sum_{\mathbf{k}} \frac{\mathcal{E}_{\mathbf{k},\mathbf{K}} \left(\mathcal{E}^2_{\mathbf{k},\mathbf{K}} - (vk_x + 2h_y)^2 - 4h_z^2 \right)}{\mathcal{E}^4_{\mathbf{k},\mathbf{K}} + 4k_x^2 v^2 (vk_x + 2h_y)^2 - \mathcal{E}^2_{\mathbf{k},\mathbf{K}} \left[(vk_x + 2h_y)^2 + 4v^2 k_x^2 + 4h_z^2 \right]}, \quad (2.44)$$

where $\mathcal{E}_{\mathbf{k},\mathbf{K}} = E - \epsilon_{\mathbf{k},\mathbf{K}}$. Again, g can be replaced in favor of the s-wave scattering length a_s, and the integral equation can be solved numerically to find the bound-state energy E_B as a function of $\mathbf{K}$, h_z, h_y, v and a_s.

The main results for ERD coupling with $\mathbf{K} = \mathbf{0}$, $h_z \neq 0$ and $h_y \neq 0$ are shown in Figs. 2.3, while the main results for ERD coupling with with $\mathbf{K} \neq \mathbf{0}$, $h_z \neq 0$ and $h_y \neq 0$ are shown in Fig. 2.4.

In Fig. 2.3a the bound state energy E_B/E_R is shown for $\mathbf{K} = 0$, $h_z = 0.5E_R$ and $h_y = 0.25E_R$ with spin-orbi coupling parameters $mv = 0.05k_R$ (blue dotted), $mv = 0.25k_R$ (green dashed), $mv = 0.75k_R$ (red dot-dashed), $mv = k_R$ (black solid). Notice the expected shift downward in E_B with increasing mv.

In Fig. 2.3b the binding energy E_{Bin}/E_R is shown as a function of the scattering

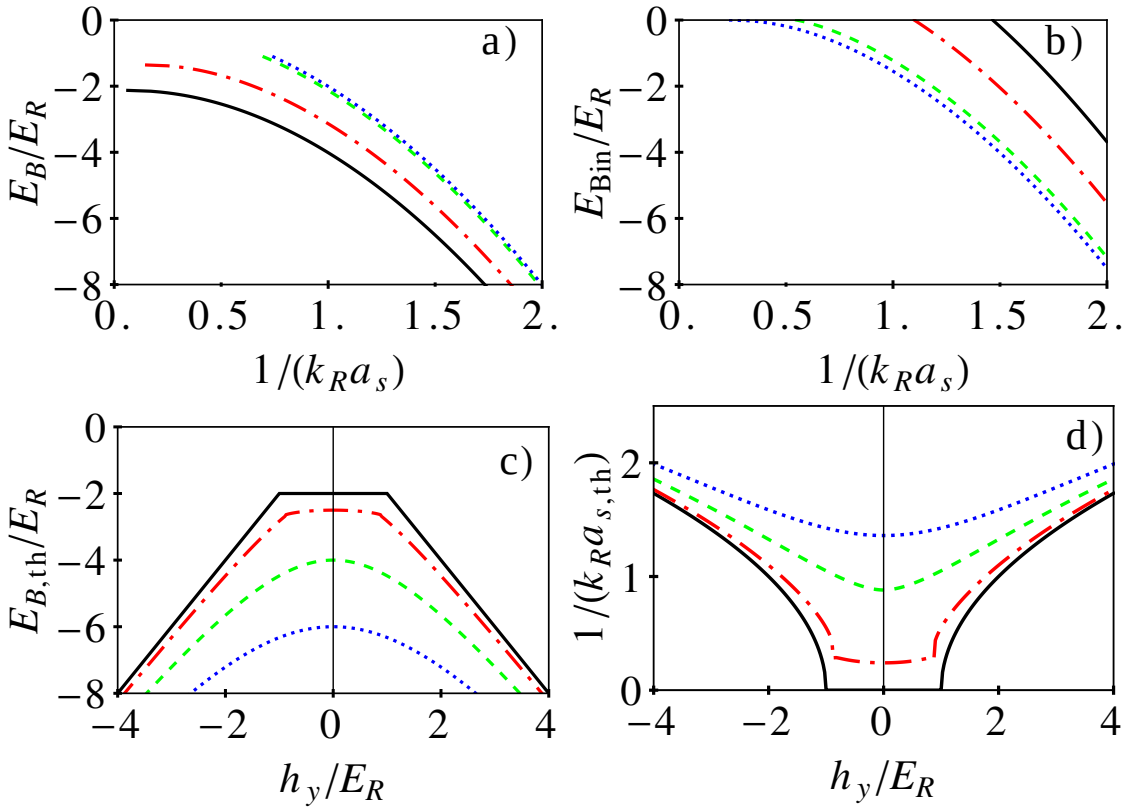

Figure 2.3: Bound state properties for ERD spin-orbit coupling with $\mathbf{K} = 0$, but with $h_z \neq 0$ and $h_y \neq 0$. a) Two-body bound state energy E_B/E_R for $h_z = 0.5E_R$ and $h_y = 0.25E_R$ with $mv = 0.05k_R$ (blue dotted), $mv = 0.25k_R$ (green dashed), $mv = 0.75k_R$ (red dot-dashed), $mv = k_R$ (black solid). b) Plots of E_{Bin}/E_R versus $1/(k_R a_s)$ with $h_z = E_R$, and $mv = k_R$ for $h_y = 0$ (blue dotted), $h_y = E_R$ (green dashed), $h_y = 2E_R$ (red dot-dashed), $h_y = 3E_R$ (black solid). Plots of $E_{B,th}/E_R$ and $1/(k_R a_s, th)$ versus h_y/E_R with $v = k_R/m$ are shown respectively in c) and d) for $h_z = 0$ (black solid); $h_z = E_R$ (red dot-dashed); $h_z = 2E_R$ (green dashed); $h_z = 3E_R$ (blue dotted).

parameter $1/(k_R a_s)$ with $h_z = E_R$, and $mv = kR$ for $h_y = 0$ (blue dotted), $h_y = E_R$ (green dashed), $h_y = 2E_R$ (red dot-dashed), $h_y = 3E_R$ (black solid). Notice, the clear trends shown in the plots. First, for fixed h_y, increasing the scattering parameter $1/(k_R a_S)$ (increasing attractive interactions) leads to a lowering of binding energy E_{Bin}, as physically expected. Second, for fixed E_{Bin}, an increasing Zeeman field h_y (detuning) requires a stronger attractive interaction [larger $1/(k_R a_s)$] to produce the same binding energy. This result is also expected physically, because the Zeeman field

h_y tends to supress the emergence of s-wave singlet bound states.

In Fig. 2.3c the bound-state energy threshold $E_{B,th}/E_R$ versus h_y/E_R is shown for fixed $mv = k_R/m$ and varying $h_z = 0$ (black solid); $h_z = E_R$ (red dot-dashed); $h_z = 2E_R$ (green dashed); $h_z = 3E_R$ (blue dotted). Notice that the larger the Zeeman field h_z (Rabi frequency) the more difficult to form two-body bound states with zero center of mass momentum $\mathbf{K} = \mathbf{0}$, and the situation is made worse whenever h_y is turned on, that is whenever $h_y \neq 0$. Again, this is somewhat expected, as Zeeman fields tend to suppress the formation of s-wave single bound states.

In Fig. 2.3d the threshold scattering parameter $1/(k_R a_{s,th})$ versus h_y/E_R is shown for fixed $mv = k_R/m$ and varying $h_z = 0$ (black solid); $h_z = E_R$ (red dot-dashed); $h_z = 2E_R$ (green dashed); $h_z = 3E_R$ (blue dotted). Notice that these plots provide essentially the same information as the plots shown in Fig. 2.3c, that is the larger the Zeeman field h_z (Rabi frequency) the more difficult to form two-body bound states with zero center of mass momentum $\mathbf{K} = \mathbf{0}$ leading to a large threshold value $1/(k_R a_{s,th})$. The situation is only made worse whenever h_y is turned on, that is whenever $h_y \neq 0$. This is the expected physical behavior as Zeeman fields tend to suppress the formation of s-wave single bound states.

The problem gets more interesting when the center of mass momentum is allowed to be non-zero, that is, $\mathbf{K} \neq \mathbf{0}$, while at the same $h_y \neq 0$ and $h_z \neq 0$. The new effect that arises is that the binding energy dispersion $E_B(\mathbf{K})$ is no longer parity even in $\mathbf{K}$, or to more specific, does not have well defined parity in K_x. In Fig. 2.4 plots of bound state threshold energies (solid black curves) and bound-state (Feshbach molecule) energies (blue dotted curves) with $1/(k_R a_s) = 0.75$; (green dashed curves) with $1/(k_R a_s) = 1.25$; and (red dot-dashed curves) with $1/(k_R a_s) = 1.75$) are shown versus the center of mass momentum $\mathbf{K} = (K_x, 0, 0)$ for $mv = k_R$ and $h_z = 0.5E_R$, with a) $h_y = 0$; b) $h_y = 0.5E_R$; c) $h_y = 1.5E_R$; and c) $h_y = 2.5E_R$. Notice the absence of inversion symmetry (parity) when $h_y \neq 0$, and, in addition, that for h_y

sufficiently large and for $1/(k_R a_s)$ sufficiently small, no bound-states with zero center mass of mass momentum exist. This can be clearly seen in the blue dotted curve of Fig. 2.4d with parameters $1/(k_R a_s) = 0.75$ and $h_y = 2.5E_R$, where only bound states with $K_x < 0$ are allowed.

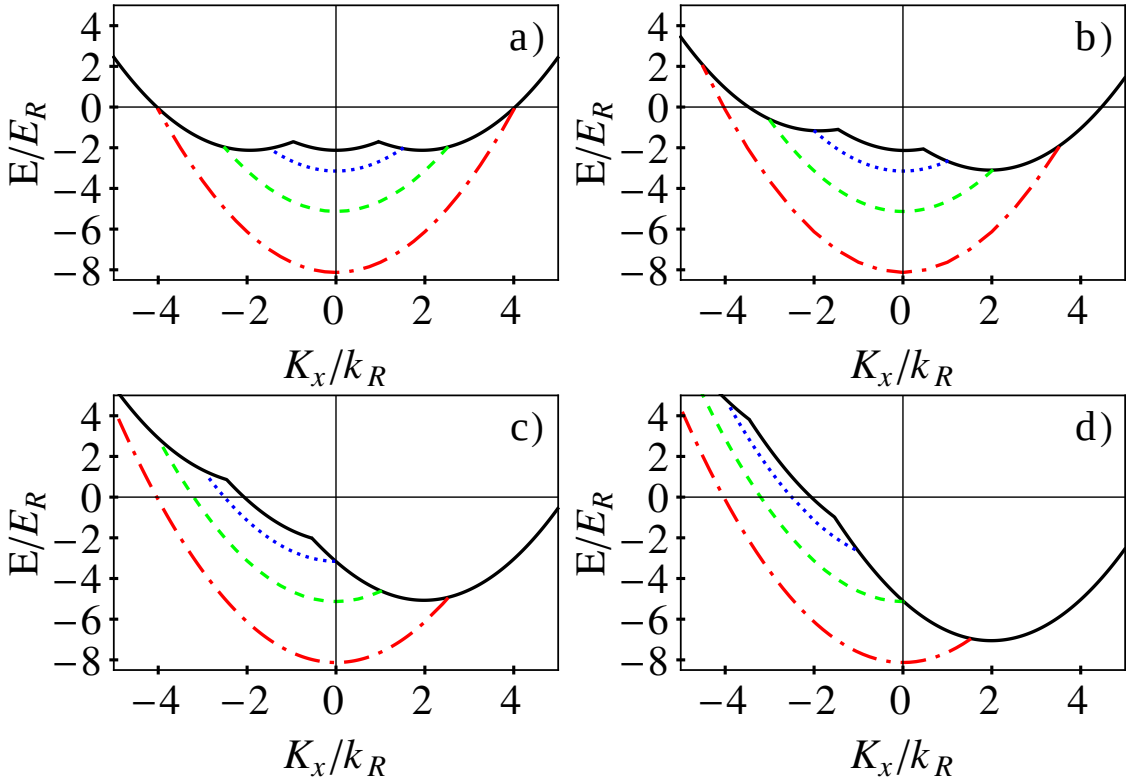

Figure 2.4: All graphs refer to the ERD case. Plots of bound state threshold energies (solid black curves) and bound-state (Feshbach molecule) energies (blue dotted curves) with $1/(k_R a_s) = 0.75$; (green dashed curves) with $1/(k_R a_s) = 1.25$; and (red dot-dashed curves) with $1/(k_R a_s) = 1.75$) are shown versus the center of mass momentum $\mathbf{K} = (K_x, 0, 0)$ for $mv = k_R$ and $h_z = 0.5E_R$, with a) $h_y = 0$; b) $h_y = 0.5E_R$; c) $h_y = 1.5E_R$; and c) $h_y = 2.5E_R$. Notice the absence of inversion symmetry (parity) when $h_y \neq 0$.

Having discussed the emergence of two-body bound states for the experimentally relevant ERD spin-orbit coupling, I will discuss next the existence of two-body bound-states for the case Rashba spin-orbit coupling.

2.3.2 Rashba Case

The Rashba type of spin-orbit coupling is the relevant case for condensed matter physics, as it can be encountered on a variety of semiconductor materials. In condensed matter systems the Rashba type of spin-orbit coupling arises due to the interplay between relativistic corrections of the motion of conduction/valence electrons and the underlying crystallographic symmetry of the material. In the case of ultracold atoms, however, the creation of artificial spin-orbit coupling of the Rashba-type has been proposed theoretically [14], but has not been realized yet experimentally. Nevertheless, it is possible that such a situation will arise in future experiments, and thus I address the emergence of two-body bound states between fermions interacting via s-wave singlet attractive interactions, and in the presence of artificial Rashba-type spin-orbit coupling and Zeeman fields.

The emergence of two-body found states (Feshbach molecules) for the Rashba type spin-orbit coupling can be studied by setting $\gamma = \beta = v_R$ in the Hamiltonian described in Eq. (2.22), leading to

$$\mathbf{H}_0(\mathbf{k},\mathbf{K}) = \begin{pmatrix} \epsilon_{\mathbf{k},\mathbf{K}} - 2h_z & h_R & 0 & p_R \\ h_R^* & \epsilon_{\mathbf{k},\mathbf{K}} & h_R & 0 \\ 0 & h_R^* & \epsilon_{\mathbf{k},\mathbf{K}} + 2h_z & -p_R^* \\ p_R^* & 0 & -p_R & \epsilon_{\mathbf{k},\mathbf{K}} \end{pmatrix}, \tag{2.45}$$

where, $h_R = v_R\left(iK_x - K_y\right)/\sqrt{2} + i\sqrt{2}h_y$ and $p_R = \sqrt{2}v_R\left(-ik_x + k_y\right)$.

The integral equation for the bound-state energies, can be obtained from the formal solution described in Eq. 2.39 using the same technique as in the ERD case, that is, upon eliminating all the other spinor-components, except for $\phi_{0,0}(\mathbf{k},\mathbf{K})$.

The simplest example to explore is the case where the center of mass momentum $\mathbf{K} = 0$, and the Zeeman fields $h_z = 0$ and $h_y = 0$. The corresponding integral equation and the actual method to solve it is outlined in Appendix IV. Here, I just quote the

result

$$\exp\left[\frac{1}{mv_R}\left(2\sqrt{-mE}-\frac{2}{a_s}\right)\right]=\frac{\sqrt{-mE}+mv_R}{\sqrt{-mE}-mv_R} \tag{2.46}$$

which gives an implicit relation between the bound-state energy E, the scattering length a_s and the Rashba velocity v_R. The expression above is an agreement with an independent derivation [17].

The main difference contained in Fig. 2.5 describing the Rashba case and Fig. 2.2 describing the ERD case in Fig. 2.2, is that there is no threshold for the formation of two-body bound states in the Rashba case when $h_y = h_z = 0$ and $\mathbf{K} = \mathbf{0}$.

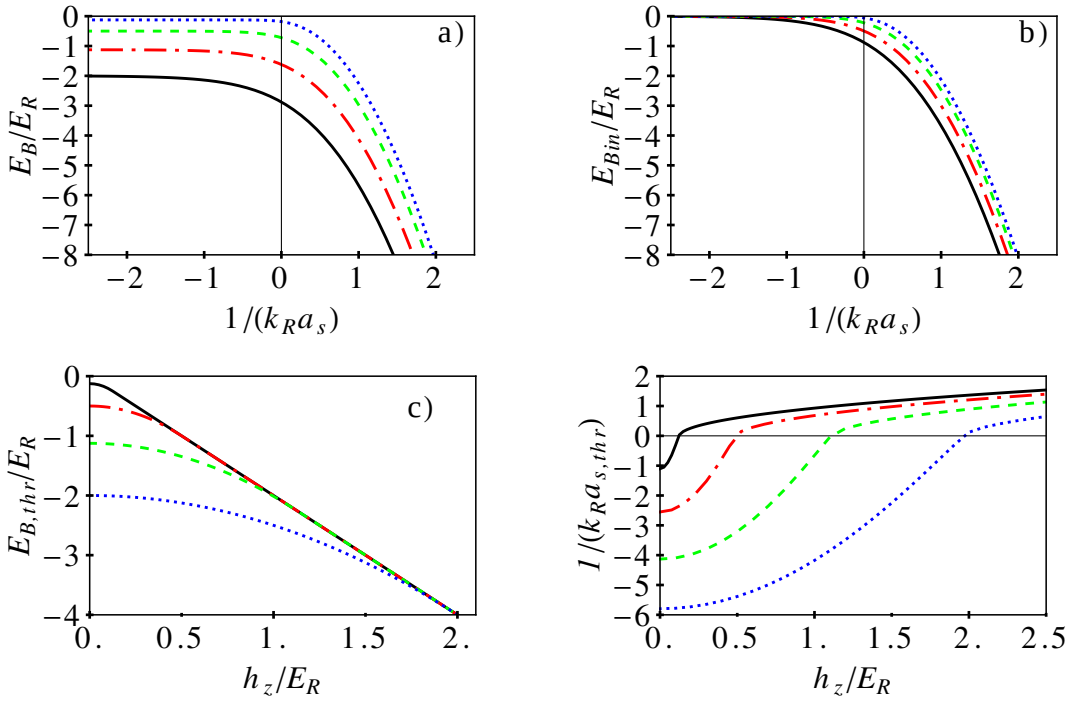

Figure 2.5: Plots of various quantities in related to the emergence of two-body bound state in the case of Rashba spin-orbit coupling with $h_z = h_y = 0$ and $\mathbf{K} = 0$. Plots of Bound state energy are shown in (a) and Binding energy in (b) versus $1/(k_R a_s)$ for $v_R = k_R/m$ (black solid), $v_R = 0.75k_R/m$ (red dot-dashed), $v_R = 0.5k_R/m$ (green dashed), $v_R = 0.25k_R/m$ (blue dotted). Threshold energies bound state energies are shown in (c) and threshold s-wave scattering parameter are shown in (d) versus h_z/E_R for $v_R = k_R/m$ (black solid), $v_R = 0.75k_R/m$ (red dot-dashed), $v_R = 0.5k_R/m$ (green dashed), $v_R = 0.25k_R/m$ (blue dotted)

If the Zeeman field $h_z \neq 0$, but $h_y = 0$ the integral equation for the bound-state

energy is given by

$$\frac{1}{g}=\frac{1}{L^3}\sum_{\mathbf{k}}\frac{\left(E-\epsilon_{\mathbf{k},0}\right)^2-4h_z^2}{\left(E-\epsilon_{\mathbf{k},0}\right)\left(\left(E-\epsilon_{\mathbf{k},0}\right)^2-4v_R^2k^2-4h_z^2\right)} \tag{2.47}$$

The main results the bound state energy, binding energy, bound state energy and scattering parameter thresholds are shown in Fig. 2.6. The main trends are exactly the same as in the ERD case, that is, Zeeman fields tends to suppress the formation of two-body bound states created by s-wave singlet interactions, while the presence of spin-orbit coupling and its spin-flipping ability tends to counter the trend imposed by the Zeeman fields. Therefore, Fig. 2.6 reflecting the Rashba case tells a qualitatively similar story as the ERD case.

The integral equation for the bound-state eigenvalue when $h_z \neq 0$, and $h_y \neq 0$ is

$$\frac{L^3}{g}= \sum_{\mathbf{k}}\frac{\mathcal{E}_{\mathbf{k},\mathbf{K}}\left(\mathcal{E}_{\mathbf{k},\mathbf{K}}^2-K_y^2v_R^2-4h_z^2-b^2\right)}{\mathcal{E}_{\mathbf{k},\mathbf{K}}^4+4v_R^2\left(k_xb+v_Rk_yK_y\right)^2-\mathcal{E}_{\mathbf{k},\mathbf{K}}^2\left(b^2+4h_z^2+v_R^2K_y^2+4v_R^2k_\perp^2\right)} \tag{2.48}$$

where, $b=v_RK_x+2h_y$ and $\mathcal{E}_{\mathbf{k},\mathbf{K}}=E-\epsilon_{\mathbf{k},\mathbf{K}}$.

Results for bound state energies for Rashba spin-orbit coupling with $h_z \neq 0$ and $h_y \neq 0$ versus the center of mass momentum component K_x are shown in Fig. 2.7. The main trends are exactly the same as in the ERD case, that is, when $h_y = 0$ the bound state dispersions have a well defined parity along the K_x direction, but when $h_y \neq 0$ parity is lost. Furthermore, when h_y is sufficiently large and the scattering parameter is sufficiently $1/(k_Ra_s)$ is sufficiently small, eventually there is no two-body bound state at zero center of mass momentum. This again the same trend found in the ERD case.

Having briefly discussed the case of artificial spin-orbit coupling for the Rashba case, I will present next a few results regarding the more general case of an arbitrary mixture of Rashba and Dresselhaus terms.

2.3.3 Arbitrary Mixture of Rashba and Dresselhaus Fields

An arbitrary mixture of Rashba and Dresselhaus terms can be tuned using the parameters β and γ in the Hamiltonian described in Eq 2.12. The integral equation for

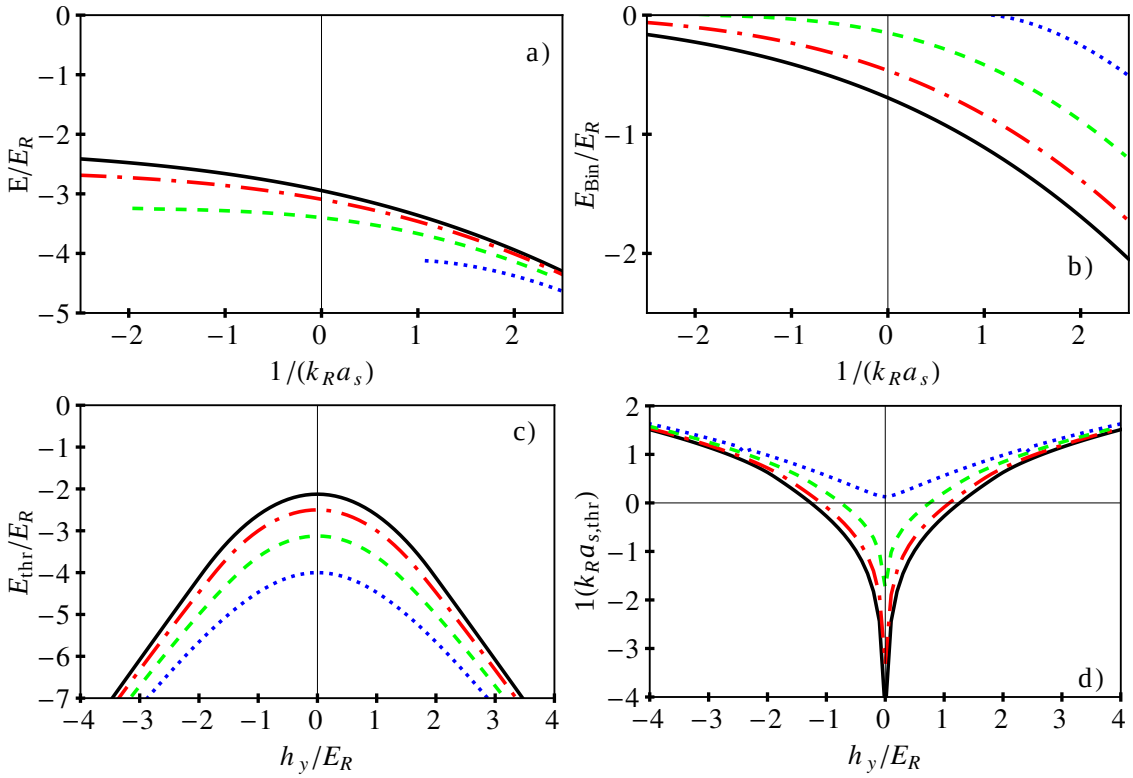

Figure 2.6: All graphs refer to the Rashba case, with $\mathbf{K} = \mathbf{0}$ and $mv_R = k_R$. The bound state energy is shown in (a), the binding energy is shown in (b) versus $1/(k_R a_s)$ with $h_y = 0.5E_R$ for $h_z = 0.5E_R$ (black solid), $h_z = E_R$ (red dot-dashed), $h_z = 1.5E_R$ (green dashed), $h_z = 2E_R$ (blue dotted). The threshold energy is shown in (c) and the threshold s-wave scattering length is shown in (d) versus h_y/E_R for $h_z = 0.5E_R$ (black solid), $h_z = E_R$ (red dot-dashed), $h_z = 1.5E_R$ (green dashed), $h_z = 2E_R$ (blue dotted)

the two-body bound states can be obtained again via row reduction leading to the intermediate relation

$$\frac{\mathcal{E}^4_{\mathbf{k},\mathbf{K}} - \mathcal{E}^2_{\mathbf{k},\mathbf{K}}\left(4\mathbf{a}^2 + \mathbf{b}^2 + 4h_z^2\right) + 4\left(\mathbf{a}\cdot\mathbf{b}\right)}{\mathcal{E}_{\mathbf{k},\mathbf{K}}\left(\mathcal{E}^2_{\mathbf{k},\mathbf{K}} - 4h_z^2 - \mathbf{b}^2\right)}\phi_{0,0}(\mathbf{k},\mathbf{K}) = \frac{g}{L^3}\sum_{\mathbf{k}'}\phi_{0,0}(\mathbf{k}',\mathbf{K}), \qquad (2.49)$$

where the vectors appearing in the expression above are $\mathbf{a} = \gamma k_x \mathbf{e}_x + \beta k_y \mathbf{e}_y$ and $\mathbf{b} = (2h_y + \gamma K_x)\,\mathbf{e}_x + \beta K_y \mathbf{e}_y$.

This integral equation can be solved by isolating the wave function $\phi_{0,0}(\mathbf{k},\mathbf{K})$ on the left hand side and then integrating the resulting expression over relative momenta

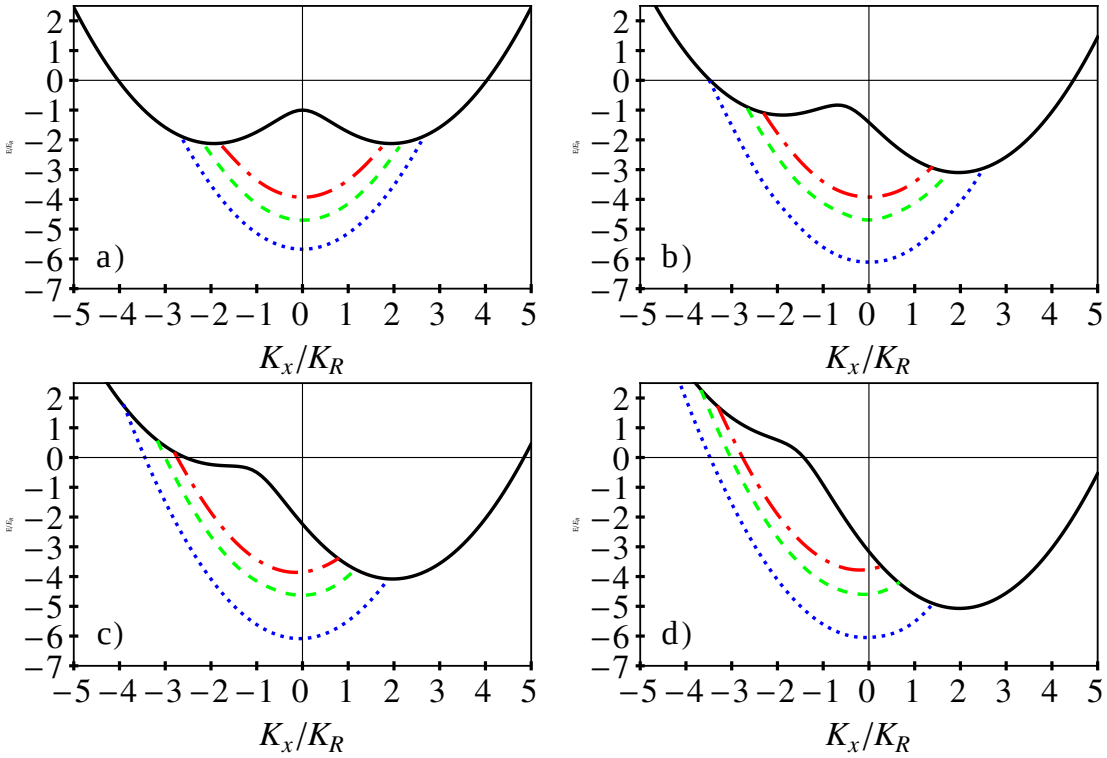

Figure 2.7: All graphs refer to the Rashba case with $mv_R = k_R$ and $h_z = 0.5E_R$. Plots of bound state threshold energies (solid black) and various bound state energy curves [blue dotted with $1/(k_R a_s) = 1$; green dashed with $1/(k_R a_s) = 0.75$; red dotdashed with $1/(k_R a_s) = 0.5$] versus center of mass momentum $\mathbf{K} = (K_x, 0, 0)$ with (a) $h_y = 0$; (b) $h_y = 0.5E_R$; (c) $h_y = 1E_R$; and (d)$h_y = 1.5E_R$. Notice the absence of inversion symmetry (parity) when $h_y \neq 0$.

$\mathbf{k}$. The resulting eigenvalue equation is

$$\frac{L^3}{g} = \sum_{\mathbf{k}} \frac{\mathcal{E}_{\mathbf{k},\mathbf{K}} \left(\mathcal{E}^2_{\mathbf{k},\mathbf{K}} - 4h_z^2 - \mathbf{b}^2\right)}{\mathcal{E}^4_{\mathbf{k},\mathbf{K}} - \mathcal{E}^2_{\mathbf{k},\mathbf{K}} \left(4\mathbf{a}^2 + \mathbf{b}^2 + 4h_z^2\right) + 4\left(\mathbf{a}\cdot\mathbf{b}\right)}, \tag{2.50}$$

corresponding to the most general case of $\mathbf{K} \neq \mathbf{0}$, $h_z \neq 0$ and $h_y \neq 0$.

I discuss first the simplest situation corresponding to $\mathbf{K} = \mathbf{0}$, $h_z = 0$ and $h_y = 0$, in which case the general relation above simplifies to

$$\frac{L^3}{g} = \sum_{\mathbf{k}} \frac{\mathcal{E}_{\mathbf{k},0}}{\mathcal{E}^2_{\mathbf{k},0} - 4\mathbf{a}\cdot\mathbf{a}}. \tag{2.51}$$

This integral equation is solved analytically in Appendix V, where a transcendental equation between the bound state energy and the spin-orbit coupling parameters γ and β is found.

When the Zeeman field $h_z \neq 0$, but still with $\mathbf{K} = \mathbf{0}$ and $h_y \neq 0$, the integral equation for the eigenvalues can be obtained from the general form shown in Eq. (2.50) leading to

$$\frac{L^3}{g} = \sum_{\mathbf{k}} \frac{\left(E - \epsilon_{\mathbf{k},0}\right)^2 - 4h_z^2}{\left(E - \epsilon_{\mathbf{k},0}\right)^3 - \left(E - \epsilon_{\mathbf{k},0}\right)\left(4h_z^2 + 4\mathbf{a}^2\right)}. \tag{2.52}$$

In Fig. 2.8 the bound state energy is shown in (a) and the binding energy is shown in (b) versus the scattering parameter $1/(k_R a_s)$ with $h_z = h_y = 0$, $\mathbf{K} = \mathbf{0}$ and Rashba parameter $mv_R = 0.5k_R$ for various Dresselhaus parameters $mv_D = 0.0001k_R$ (black solid), $mv_D = 0.1k_R$ (red dot-dashed), $mv_D = 0.2k_R$ (green dashed), $mv_D = k_R$ (blue dotted). While the bound state threshold energy is shown in (c) and the threshold scattering length $1(k_R a_s)$ is shown in (d) versus h_z/E_R with $h_y = 0$, $\mathbf{K} = \mathbf{0}$ and Rashba parameter $mv_R = 0.5k_R$ for various Dresselhaus parameters $mv_D = 0.0001k_R$ (black solid), $mv_D = 0.1k_R$ (red dot-dashed), $mv_D = 0.2k_R$ (green dashed), $mv_D = k_R$ (blue dotted). The main information to be extracted from all the graphs in Fig. 2.8 is that the behaviour of the system is intermediate between the ERD and the Rashba cases. But again the same qualitative trends are observed: Zeeman fields tend to suppress the formation of two-body states due to s-wave singlet interactions, and spin-orbit coupling tends to counter the detrimental effects of Zeeman fields due to its spin-flipping ability.

In Fig. 2.9, the bound state energy is shown in (a) and the binding energy is shown in (b) versus $1/(k_R a_s)$ with $h_z = E_R$, $h_y = 0.5E_R$, $\mathbf{K} = 0$ and Rashba parameter $mv_R = 0.5k_R$ for various Dresselhaus parameters $mv_D = 0.0001k_R$ (black solid), $mv_D = 0.1k_R$ (red dot-dashed), $mv_D = 0.2k_R$ (green dashed), $mv_D = k_R$ (blue dotted). The bound state energy threshold is shown in (c) and the threshold scattering parameter $1/(k_R a_s)$ is shown in (d) versus h_y/E_R for fixed values of $h_z = 0.5E_R$, $\mathbf{K} = 0$ and Rashba parameter $mv_R = 0.5k_R$ and varying Dresselhaus parameters $v_D = 0.0001k_R/m$ (black solid), $v_D = 0.1k_R/m$ (red, dot-dashed), $v_D = 0.2k_R/m$ (green, dashed), $v_D = k_R/m$ (blue, dotted). The main information to be extracted

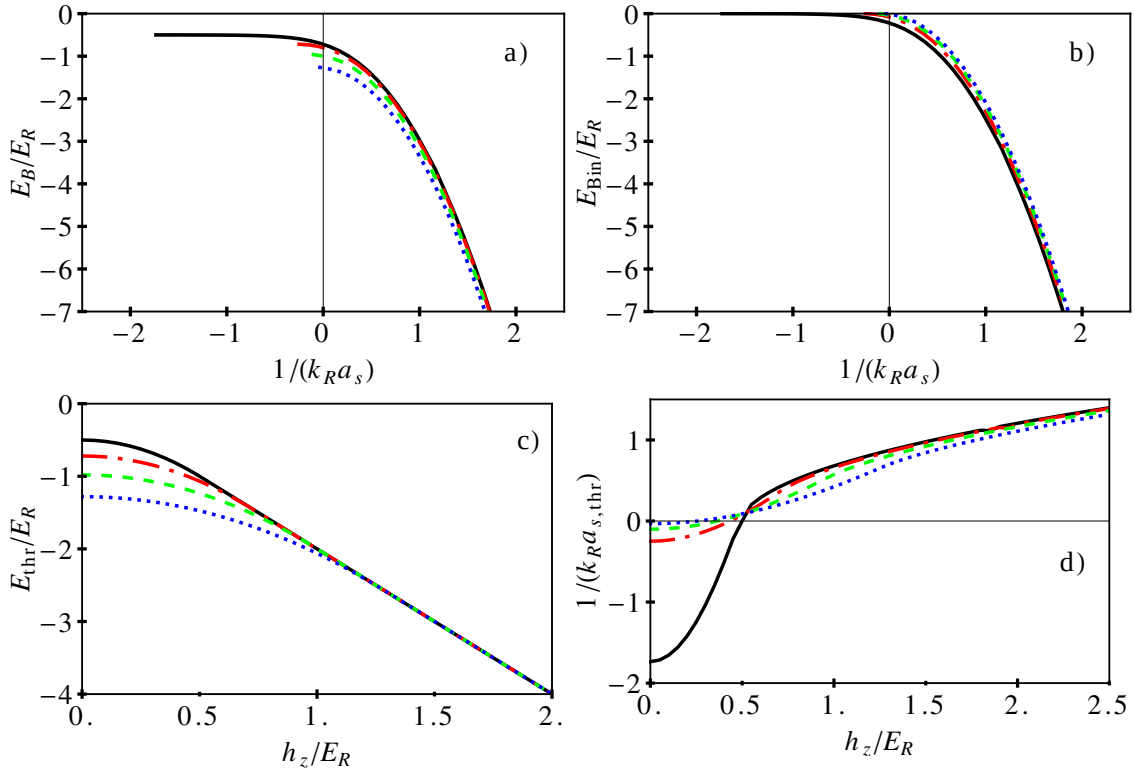

Figure 2.8: All figures refer to the case of an arbitrary mixture of Rashba and Dresselhaus fields. The bound state energy is shown in (a) and the binding energy is shown in (b) versus the scattering parameter $1/(k_R a_s)$ with $h_z = h_y = 0$, $\mathbf{K} = \mathbf{0}$ and Rashba parameter $mv_R = 0.5k_R$ for various Dresselhaus parameters $mv_D = 0.0001k_R$ (black solid), $mv_D = 0.1k_R$ (red dot-dashed), $mv_D = 0.2k_R$ (green dashed), $mv_D = k_R$ (blue dotted). The bound state threshold energy is shown in (c) and the threshold scattering length $1(k_R a_s)$ in shown in (d) versus h_z/E_R with $h_y = 0$, $\mathbf{K} = \mathbf{0}$ and Rashba parameter $mv_R = 0.5k_R$ for various Dresselhaus parameters $mv_D = 0.0001k_R$ (black solid), $mv_D = 0.1k_R$ (red dot-dashed), $mv_D = 0.2k_R$ (green dashed), $mv_D = k_R$ (blue dotted)

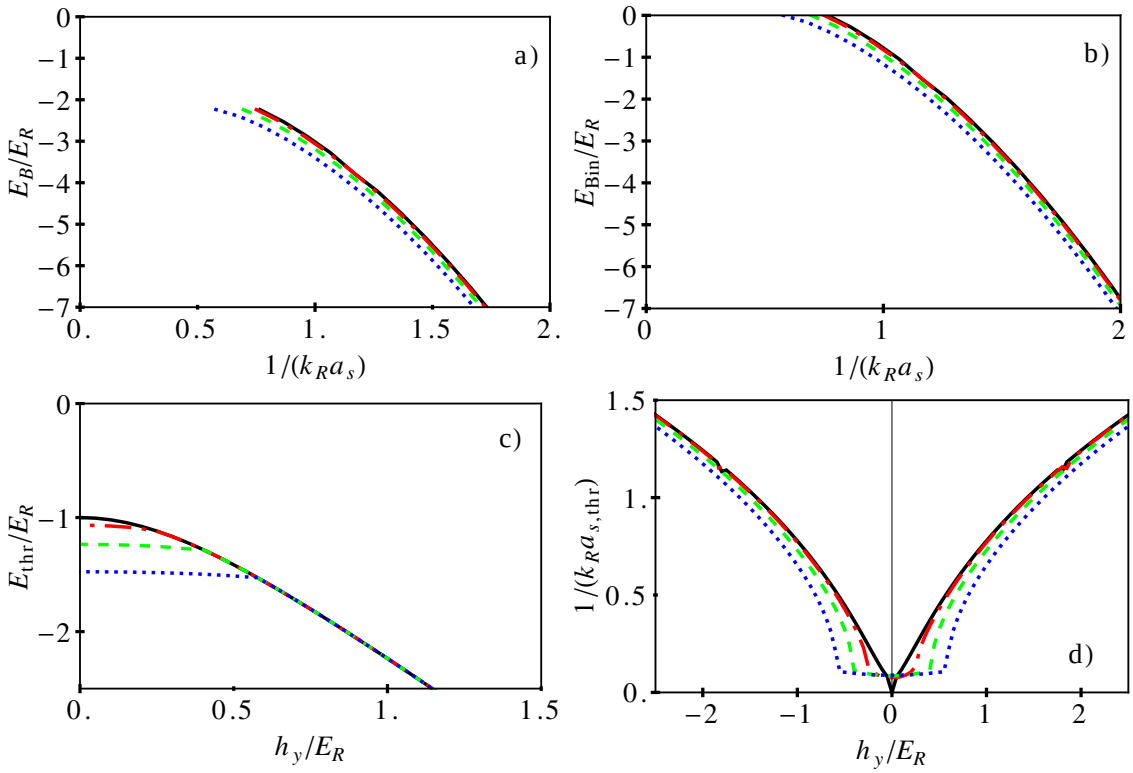

Figure 2.9: All figures refer to the case of an arbitrary mixture of Rashba and Dresselhaus fields. The bound state energy is shown in (a) and the binding energy is shown in (b) versus $1/(k_R a_s)$ with $h_z = E_R$, $h_y = 0.5E_R$, $\mathbf{K} = 0$ and Rashba parameter $mv_R = 0.5k_R$ for various Dresselhaus parameters $mv_D = 0.0001k_R$ (black solid), $mv_D = 0.1k_R$ (red dot-dashed), $mv_D = 0.2k_R$ (green dashed), $mv_D = k_R$ (blue dotted). The bound state energy threshold is shown in (c) and the threshold scattering parameter $1/(k_R a_s)$ is shown in (d) versus h_y/E_R for fixed values of $h_z = 0.5E_R$, $\mathbf{K} = 0$ and Rashba parameter $mv_R = 0.5k_R$ and varying Dresselhaus parameters $v_D = 0.0001k_R/m$ (black solid), $v_D = 0.1k_R/m$ (red, dot-dashed), $v_D = 0.2k_R/m$ (green, dashed), $v_D = k_R/m$ (blue, dotted)

from all the graphs in Fig. 2.9 is that the behaviour of the system is intermediate between the ERD and the Rashba cases. But possesses the same qualitative trends as found both in the ERD and Rashba cases, that is, Zeeman fields tend to suppress the formation of two-body states due to s-wave singlet interactions, and spin-orbit coupling tends to counter the detrimental effects of Zeeman fields due to its spin-flipping ability.

Having discussed the emergence of two-body bound states (Feshbach molecules) in the presence of artificial spin-orbit coupling of the ERD, Rashba and arbitrary

mixtures of Rashba and Dresselhaus fields, I will discuss next how these spin-orbit couplings affect the effective masses of the two-body bound states.

2.4 Effective Mass Tensor

In this section I will discuss the effective mass tensor for the two-body bound states (Feshbach molecules) as a function of the artificial spin-orbit coupling, Zeeman fields and interaction parameter.

The effective mass tensor can be easily found via the knowledge of the bound state energy dispersion $E_B(\mathbf{K})$ by performing a Taylor expansion of this function near its minimum. In this section, I will confine myself to the expansion near zero center of mass momentum $\mathbf{K} = \mathbf{0}$, meaning that the expansion will be justified so long as the minimum of $E_B(\mathbf{K})$ indeed happens at $\mathbf{K} = \mathbf{0}$. Whenever this is not the case, the new minimum at finite $\mathbf{K}$ needs to be found, and the effective mass tensor needs to be redefined in the neighboorhood of that finite $\mathbf{K}$ minimum.

With the caveat described in the preceeding paragraph, I perform the expansion

$$E_B(\mathbf{K}) \approx E_B(\mathbf{K}=0) + K_i \left.\frac{\partial E_B(\mathbf{K})}{\partial K_i}\right|_{\mathbf{K}=\mathbf{0}} + \frac{1}{2} K_i K_j \left.\left(\frac{\partial^2 E_B(\mathbf{K})}{\partial K_i \partial K_j}\right)\right|_{\mathbf{K}=\mathbf{0}} \quad (2.53)$$

$$\equiv E_B(\mathbf{K}=\mathbf{0}) + K_i v_i + \frac{1}{2} K_i D_{ij} K_j, \quad (2.54)$$

where $E_B(\mathbf{K} = \mathbf{0})$ is the bound state energy found previously, the Einstein summation of repeated indices is understood, and the derivatives are defined as $v_i = \partial E_B(\mathbf{K})/\partial K_i|_{\mathbf{K}=\mathbf{0}}$ and $D_{ij} = \partial^2 E_B(\mathbf{K})/\partial K_i \partial K_j$. When $v_i = 0$, then the dispersion $E_B(\mathbf{K})$ is quadratic and $D_{ij} = (m^{-1})_{ij}$, meaning that the effective mass tensor is just $m_{ij} = (D^{-1})_{ij}$, with the indices $\{i, j\}$ spanning the spatial directions $\{x, y, z\}$.

If the expression for $E_B(\mathbf{K})$ where known analytically, the task of determining the effective mass tensor would be easy. However, the momentum dependence of $E_B(\mathbf{K})$ is only known implicitly via the integral equations for the bound-state eigenvalue, which I derived in the previous sections. Therefore, to obtain the effective mass tensor in

the ERD, Rashba and more generally arbitrary mixture of Rashba and Dresselhaus spin-orbit fields, I will make use of their respective eigenvalue equations.

The remainder of this effective mass section will follow a similar structure as the one utilized in the previous section regarding the bound state energy. I will discuss first the ERD case, then the Rashba case, and last the case of arbitrary mixture of Rashba and Dresselhaus terms. The Mathematica codes to calculate effective mass components are given in Appendix VI.

2.4.1 Equal Rashba-Dresselhaus Case

In order to calculate the effective mass tensor, it is important to obtain the derivatives v_i and D_{ij}, by using the bound state eigenvalue integral equation from Eq. (2.44) for the most general case of $\mathbf{K} \neq \mathbf{0}$, $h_z \neq 0$ and $h_y \neq 0$, which I repeat here by defining the function

$$F(\mathbf{K}, E) = \frac{L^3}{g} - \sum_{\mathbf{k}} \frac{\mathcal{E}_{\mathbf{k},\mathbf{K}} \left(\mathcal{E}_{\mathbf{k},\mathbf{K}}^2 - b^2 - 4h_z^2\right)}{\mathcal{E}_{\mathbf{k},\mathbf{K}}^4 + 4k_x^2 v^2 b^2 - \mathcal{E}_{\mathbf{k},\mathbf{K}}^2 \left(b^2 + 4v^2 k_x^2 + 4h_z^2\right)}, \tag{2.55}$$

where, $b = vK_x + 2h_y$. When the implicit function $F(\mathbf{K}, E) = F(K_x, K_y, K_z, E)$ is set equal to zero, then the bound state energy $E_B(\mathbf{K})$ is the solution of $F(\mathbf{K}, E) = 0$.

The first derivative of $E_B(\mathbf{K})$ is then

$$v_i = \left.\frac{\partial E(\mathbf{K})}{\partial K_i}\right|_{\mathbf{K}=\mathbf{0}} = -\left.\frac{\partial F(\mathbf{K}, E)/\partial K_i}{\partial F(\mathbf{K}, E)/\partial E}\right|_{\mathbf{K}=0} \equiv -\left.\frac{F_i}{F_E}\right|_{\mathbf{K}=0}, \tag{2.56}$$

while the second derivative tensor is diagonal having the form

$$D_{ii} = \left.\frac{\partial^2 E\left(\mathbf{K}\right)}{\partial K_i \partial K_i}\right|_{\mathbf{K}=\mathbf{0}} = -\frac{\partial}{\partial K_i}\left(F_i F_E^{-1}\right)\Big|_{\mathbf{K}=0} = -\left(F_{ii}F_E^{-1} - F_i F_{Ei} F_E^{-2}\right)\big|_{\mathbf{K}=0}, \tag{2.57}$$

but in the limit of zero center-of-mass momentum, the derivative F_{Ei} in the second term vanishes. This leads to the effective mass tensor

$$m_{ii} = (D^{-1})_{ii} = -\frac{F_E}{F_{ii}} \tag{2.58}$$

Now, I will start analyzing the effective mass tensor for the simplest case where $h_y = 0$, and $h_z = 0$. In this case, the function

$$F(\mathbf{K}, E) = \frac{L^3}{g} - \sum_{\mathbf{k}} \frac{(\epsilon_{\mathbf{k},\mathbf{K}} - E)}{(\epsilon_{\mathbf{k},\mathbf{K}} - E)^2 - 4v^2 k_x^2} \tag{2.59}$$

and the effective mass expressions can be found straightforwardly. The first derivative v_i vanishes for all directions, and the effective mass tensor is diagonal $m_{ii} = -F_E/F_{ii}$ and has all components equal to $2m$ in the limit large scattering parameter. Furthermore, m_{ii} is independent of spin-orbit coupling. This is not surprising, because the ERD spin orbit coupling field can be *gauged away* when Zeeman fields are absent.

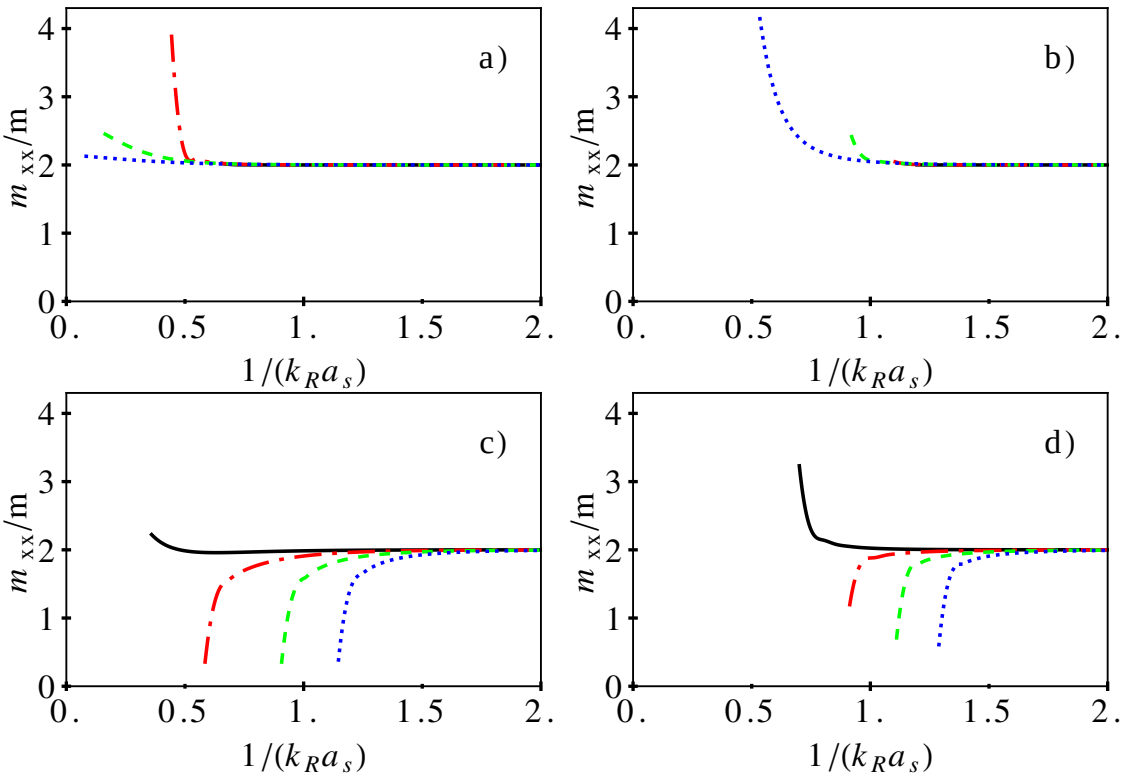

Figure 2.10: Effective mass tensor m_{xx}/m plots for ERD type of spin-orbit coupling $mv = 0.25k_R$ (black solid), $mv = 0.5k_R$ (red dot-dashed), $mv = 0.75k_R$ (green dashed), $mv = k_R$ (blue dotted) with $h_y = 0$, for (a) $h_z = 0.5E_R$ and (b) $h_z = E_R$. Effective mass m_{xx}/m plots with $mv = k_R$ when $h_y = 0.5E_R$ (black solid), $h_y = E_R$ (red dot-dashed), $h_y = 1.5E_R$ (green dashed), $h_y = 2E_R$ (blue dotted) for (c) $h_z = 0.5E_R$ and (d) $h_z = 1.5E_R$.

Next, I will look at the effective mass tensor for case where $h_y = 0$, but $h_z \neq 0$. In this case, the function v_i also vanishes, and the effective mass tensor remains diagonal,

with the components $m_{yy} = m_{zz} = 2m$ both independent of spin-orbit coupling and scattering parameter. Non-trivial behavior occurs only in m_{xx} and it is illustrated on the top panels of Fig.2.10, where m_{xx} remains always larger than twice the mass of an individual fermion, that is $m_{xx} \geq 2m$, for any value of the scattering parameter.

Finally, I briefly discuss the effective mass tensor for case where $h_y \neq 0$, but $h_z \neq 0$. In this case, the function v_i does not vanish, but the effective mass tensor remains diagonal, with the components $m_{yy} = m_{zz} = 2m$ both independent of spin-orbit coupling and scattering parameter. Non-trivial behavior occurs again only in m_{xx} and it is illustrated on the bottom panels of Fig.2.10, where $m_{xx} \geq 2m$ as as the scattering parameter is varied for smaller values of h_y/E_R, but becomes $m_{xx} \geq 2m$ as the scattering parameter is varied for larger values of h_y/E_R.

Having discussed the behaviour of the effective masses of the two-body bound states in the presence of ERD spin-orbit coupling and Zeeman fields h_z, h_y, I will next discuss next the effective mass tensor for the Rashba case.

2.4.2 Rashba Case

The effective masses for the Rashba case are obtained using the same general method outlined at the beginning of section 2.4.

When Zeeman fields are zero $h_y = h_z = 0$, but the Rashba velocity $v_R \neq 0$, the integral describing the bound state eigenvalue is

$$F(\mathbf{K}, E) = \frac{L^3}{g} - \sum_{\mathbf{k}} \frac{(\epsilon_{\mathbf{k},\mathbf{K}} - E)\left((\epsilon_{\mathbf{k},\mathbf{K}} - E)^2 - v_R^2 \mathbf{K}_\perp^2\right)}{(\epsilon_{\mathbf{k},\mathbf{K}} - E)^4 + 4v_R^2 (\mathbf{k}_\perp \cdot \mathbf{K}_\perp) - (\epsilon_{\mathbf{k},\mathbf{K}} - E)^2 v_R^2 (\mathbf{K}_\perp^2 + k_\perp^2)} \quad (2.60)$$

where the two-dimensional momentum $\mathbf{K}_\perp = (K_x, K_y)$ and $k_\perp^2 = k_x^2 + k_y^2$.

In this simpler case, the expressions for the effective masses can be calculated analytically using the method developed in the introduction of section 2.4, and agree with recent accounts [17]. The effective mass tensor is diagonal, with the effective

masses $m_{xx} = m_{yy} = m_\perp$ given by

$$m_\perp = 2m\left[1 + \frac{-E_0 - \sqrt{-mv_R^2 E_0}}{(-E_0)(-\widetilde{E}_0)}\left(-mv_R^2 - \widetilde{E}_0 \ln\left(\frac{-E_0}{-\widetilde{E}_0}\right)\right)\right], \tag{2.61}$$

where $\widetilde{E}_0 = E_0 + mv_R^2$, with E_0 being the bound state energy at $\mathbf{K} = 0$.

In the case where $v_R \neq 0$, $h_z \neq 0$ and $h_y = 0$, the effective mass tensor remains diagonal, and since the x and y directions remain equivalent, it is not too difficult to shown that the effective masses $m_{xx} = m_{yy} = m_\perp$. This case is illustrated on the top panels of Fig. 2.7.

In the case where $v_R \neq 0$, $h_z \neq 0$ and $h_y \neq 0$, the effective mass tensor remains diagonal, but the x and y directions are no longer equivalent, in which case the effective masses $m_{xx} \neq m_{yy}$. This case is illustrated on the bottom panels of Fig, 2.7. Notice in Fig. 2.11 that the effective mass m_{xx}/m diverges and becomes negative, indicating for those values of parameters that the minimum of the bound-state energy dispersion does not occur at zero center mass momentum $\mathbf{K} = 0$, but rather at some finite momentum $\mathbf{K} \neq \mathbf{0}$.

Having discussed the effective mass for the Rashba case, when both artificial Zeemans fields (detuning and Rabi frequency) are present, I discuss next the more general case of arbitrary mixture of Rashba and Dresselhaus terms.

2.4.3 Arbitrary Mixture of Rashba & Dresselhaus Case

The effective masses for arbitrary mixtures of Rashba and Dresselhaus types of spin-orbit coupling fields is interesting for both for ultra-cold Fermions and condensed matter physics. But it is more likely that it can studied in a controlled way in ultra-cold fermions, and that are already methods outlined that could artificialy engineer such a mixture.

The function $F(\mathbf{K}, E)$ for this case is obtained directly from the integral equation for the bound state energy given in Eq. 2.50. The Mathematica code to calculate the effective mass tensor in this case is given in Appendix VI.

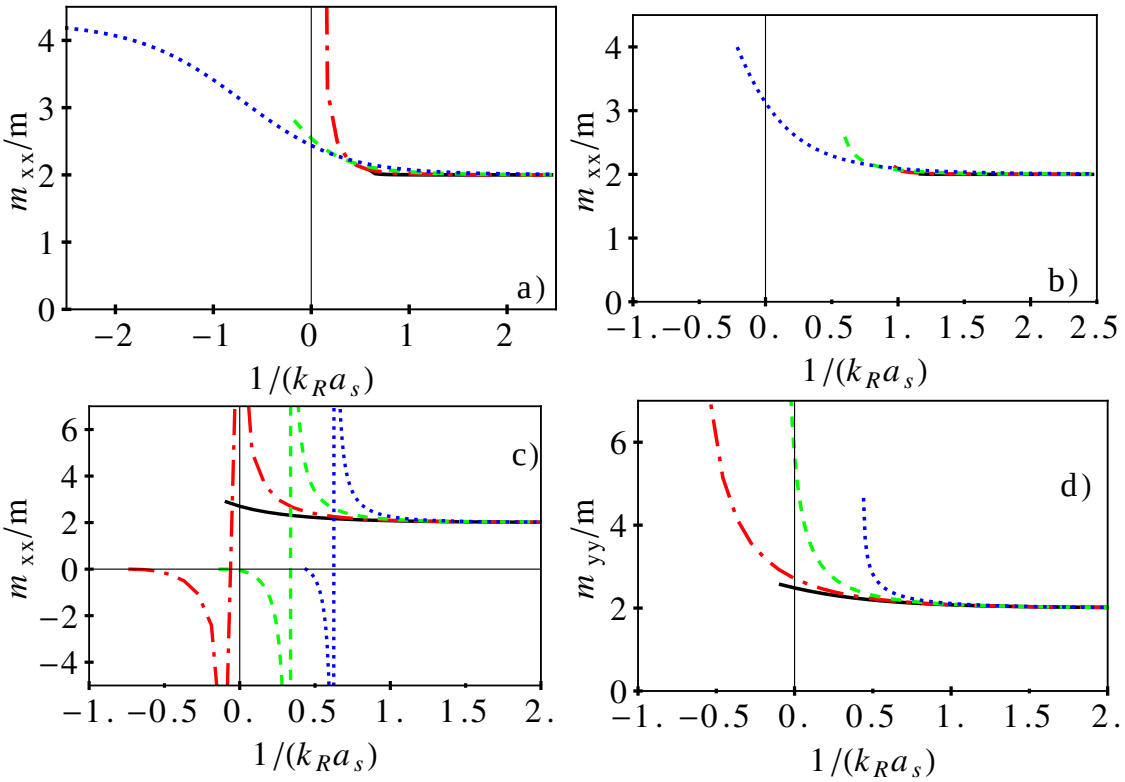

Figure 2.11: Plots of the effective mass components m_{xx}/m plots (a, b, c) and m_{yy}/m for for Rashba type of spin-orbit coupling ($v_R \neq 0$) when $h_y = 0$ (a, b) and when $h_y \neq 0$ (c, d). Notice that when $h_y = 0$ then $m_{xx} = m_{yy}$, and when $h_y \neq 0$ then $m_{xx} \neq m_{yy}$. In the top panels, where $h_y = 0$, the values of h_z are $h_z = 0.5E_R$ (a) and $h_z = 1.5E_R$ (b), and the all curves are labeled by values of mv_R corresponding to $mv_R = 0.25k_R$ (black solid), $mv_R = 0.5k_R$ (red dot-dashed), $mv_R = 0.75k_R$ (green dashed), $mv_R = k_R$ (blue dotted). In the bottom panels, where $h_y \neq 0$, the parameter $h_z = 0.5E_R$ and $mv_R = k_R$ and all the curves are labeled by $h_y = 0.5E_R$ (black solid), $h_y = E_R$ (red dot-dashed), $h_y = 1.5E_R$ (green dashed), $h_y = 2E_R$ (blue dotted). Notice that when $h_y \neq 0$ the effective masses m_{xx} (c) and m_{yy} (d) are not equal.

The effective mass tensor components when the Zeeman fields are turned off, that is, $h_z = 0$ and $h_y = 0$, are plotted in Figs. 2.12a and 2.12c. The parameters used in the figures are $mv_R = 0.5k_R$ for the Rashba momentum and $mv_D = 0.0001k_R$ (black solid), $mv_D = 0.1k_R$ (red dot-dashed), $mv_D = 0.2k_R$ (green dashed), $mv_D = 0.3k_R$ (blue dotted) for the Dresselhaus momenta. Notice that the effective masses are always larger than 2m in this case.

The effective mass tensor components when the Zeeman fields are turned on, that is, $h_z \neq 0$ and $h_y \neq 0$, are plotted in Figs. 2.12b and 2.12d. The parameters used

in the figures are $h_y = 1.5E_R$, $h_z = 0.5E_R$, with Rashba parameter $mv_R = 0.5k_R$ and Dresselhaus parameters $mv_D = 0.0001k_R$ (black solid), $mv_D = 0.1k_R$ (red dot-dashed), $mv_D = 0.2k_R$ (green dashed), $mv_D = 0.3k_R$ (blue dotted). Notice that the m_{xx} can become negative, indicating that the minimum of the bound-state energy dispersion does not occur at $K_x = 0$. The same effect does not happen for m_{yy}, because the field h_y does not alter the location of the minimum with respect to K_y.

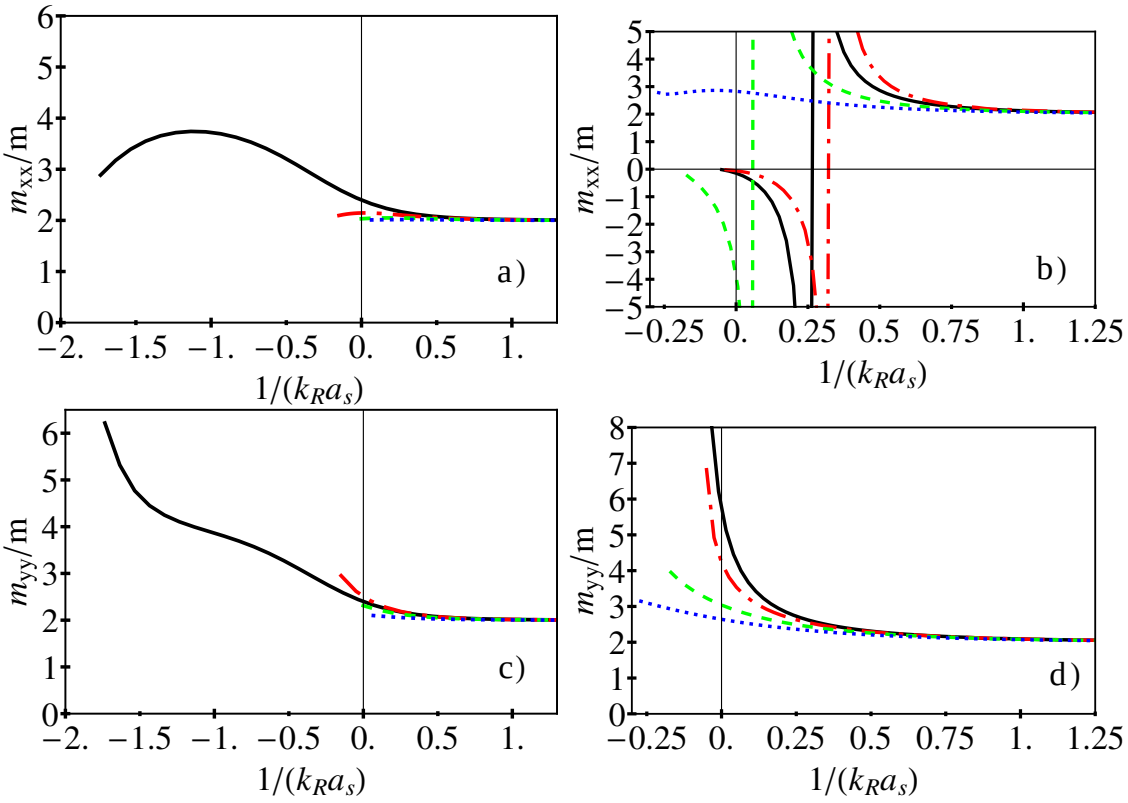

Figure 2.12: Effective mass plots for arbitrary mixture of Rashba and Dresselhaus spin-orbit coupling. The figures on the left show the effective mass components m_{xx} (a) and m_{yy} (c) for no Zeeman fields ($h_y = h_z = 0$), but Rashba parameter $mv_R = 0.5k_R$ and Dresselhaus parameters $mv_D = 0.0001k_R$ (black solid), $mv_D = 0.1k_R$ (red dot-dashed), $mv_D = 0.2k_R$ (green dashed), $mv_D = 0.3k_R$ (blue dotted). The figures on the right show effective mass components m_{xx} (b) and m_{yy} (d) when the Zeeman fields are $h_y = 1.5E_R$, $h_z = 0.5E_R$, with Rashba parameter $mv_R = 0.5k_R$ and Dresselhaus parameters $mv_D = 0.0001k_R$ (black solid), $mv_D = 0.1k_R$ (red dot-dashed), $mv_D = 0.2k_R$ (green dashed), $mv_D = 0.3k_R$ (blue dotted).

Having discussed the effective mass tensor for the spin-orbit cases involving ERD, Rashba and arbitrary mixture of Rashba and Dresselhaus terms, I will discuss next

how the effective mass tensor affects the Bose-Einstein condensation temperature of a dilute non-interacting gas of two-body bound states (Feshbach molecules) in the presence of artificial spin-orbit coupling and Zeeman fields.

2.5 Bose-Einstein Condensation Temperature

In this section, I will discuss the Bose-Einstein condensation temperature of the two-body bound states obtained for the various types of spin-orbit coupling discussed. Given that the two-body bound states are really Feshbach molecules, these molecules behave like bosons, as long as the separation between the molecules is much larger than their size. Therefore, I will be making the assumption that the gas of bound states (Feshbach molecules) is dilute and that the bound states do not interact with each other, such that the usual approximations for Bose-Einstein condensation hold.

In the previous section, I showed that, in several cases, the energy of the bound-states could be expressed as

$$E(\mathbf{K}) = E_0 + \frac{K_x^2}{2M_x} + \frac{K_y^2}{2M_y} + \frac{K_z^2}{2M_z}, \tag{2.62}$$

where E_0 is the energy of the bound state at zero center of mass momentum $\mathbf{K} = 0$, (K_x, K_y, K_z) are the components of $\mathbf{K}$ and $\{M_x, M_y, M_z\}$ are the effective masses along the x, y, z axis respectively. These effective masses have the following correspondence to the effective masses calculated in the previous section: $M_x = m_{xx}$, $M_y = m_{yy}$ and $M_z = m_{zz}$.

Considering a gas of dilute and non-interacting molecular bound states, the density of these molecules is

$$n_{\text{bs}} = \frac{1}{L^3} \sum_{\mathbf{K}} b(\mathbf{K}) \tag{2.63}$$

where L^3 is the volume of free space, and

$$b(\mathbf{K}) = \frac{1}{e^{[E_{\mathbf{K}} - \mu_{bs}]} - 1} \tag{2.64}$$

is the Bose-Einstein distribution function. When the chemical potential $\mu_{\rm bs}$ approaches the binding energy E_0, then the bound states exhibit the phenomenon of Bose-Einstein condensation. The present situation differs slightly from the standard case with dispersion $E(\mathbf{K}) = E_0 + K^2/(2M)$, because the masses are anisotropic.

In the isotropic case (when there are no artificial spin-orbit and Zeeman fields) condensation occurs when

$$n_{\rm bs} = C T_{BEC}^{3/2} M^{3/2}, \tag{2.65}$$

where the constant $C = 0.132344$. This leads to the standard BEC temperature

$$T_{BEC} = C^{-2/3} \frac{n_{\rm bs}^{2/3}}{M}. \tag{2.66}$$

However, since each bound state is formed by two fermions, the density of bound states is half of the fermions density, that is, $n_{\rm bs} = n_{\rm F}/2$, and the mass of the bound state is twice that of the fermion, that is, $M = 2m$. These two statements put together lead to the relation $n_{\rm bs}^{2/3}/M = 2^{-2/3} n_{\rm F}^{2/3}/(2m)$, which ultimately produces the condensation temperature

$$T_{BEC} = (2C)^{-2/3} \frac{n_{\rm F}^{2/3}}{2m} = 0.218 E_F, \tag{2.67}$$

where $E_F = k_F^2/(2m)$ is the Fermi energy of a non-interacting gas of fermions with two internal spin states. This standard result [24] showing that T_{BEC} is proportional to the Fermi energy E_F is not surprising since each of the molecular bound states are formed of two fermions.

In the anisotropic case (when artifical spin-orbit and Zeemans fields are present), the only modification in the intermediate expression for the Bose-Einstein condensation temperature shown in Eq. (2.66) is to change the mass M of the bound-state into the geometrical mean $M_{\rm gm} = (M_x M_y M_z)^{1/3}$, leading to the result

$$T_{BEC} = C^{-2/3} \frac{n_{\rm bs}^{2/3}}{M_{\rm gm}}. \tag{2.68}$$

If I define condensation temperatures of the anisotropic and isotropic cases to be T_{BEC}^{ani} and T_{BEC}^{iso} respectively, then their ratio is simply given by

$$\frac{T_{BEC}^{ani}}{T_{BEC}^{iso}} = \frac{M}{M_{\rm gm}}. \tag{2.69}$$

This result shows that in the limit that the artificial spin-orbit coupling and Zeemans fields are small in comparison to the interaction parameter, the effective masses become isotropic, and the standard results are recovered, as expected. Some more details of the derivation of these results are found in Appendix VII.

The Bose-Einstein condensation temperature T_{BEC} in units of the Fermi energy E_F is plotted in Fig. 2.13 for several cases. However, instead of using really T_{BEC}/E_F, I plotted T_c/E_F, where T_c is defined to be half of T_{BEC}, that is $T_c = T_{BEC}/2$. Using this definition it means that when the scattering parameter is very large and positive then $T_c/E_F \to 0.218/2 = 0.109$ as shown in the figure. The top panels refer ERD case, the middle panels refer to the Rashba, and the lower panels refer to a more generic mixture of Rashba and Dresselhaus terms. Any variations in T_c (or T_{BEC}) from the limiting case of 0.109 (or 0.218) is really due to variations in the geometrical mean of the masses M_{gm}.

Having discussed the Bose-Einstein condensation temperature of a dilute gas of two-body bound states (Feshbach molecules) of Fermi atoms in the presence of artificial spin-orbit coupling and Zeemans, I will make next a brief summary statement for this chapter.

2.6 Conclusions

In summary, I described in this chapter the formation of bound states of two Fermi atoms with two internal states by tuning their mutual interactions via Feshbach resonances. Assuming that the fermions are in free space, I obtained the binding energy, the effective masses and the Bose-Einstein condensation temperature of the resulting bound states (Feshbach molecules) as a function of the s-wave scattering length,

artificial spin-orbit coupling and Zeeman fields.

These investigations were performed for the currently experimentally relevant equal-Rashba-Dresselhaus (ERD) spin-orbit fields, but also for Rashba fields and more generally for an arbitrary mixture of Rashba and Dresselhaus spin-orbit coupling. The qualitative differences between these particular cases was emphasized in the bulk of the chapter.

One important aspect that was not discussed in this chapter is that ultra-cold fermions are typically trapped in a harmonic potential. Thus a more complete theoretical analysis would require the inclusion of a harmonically confining potential in order to investigate its effect on the formation of two-body bound states in the presence of artificial spin-orbit and Zeeman fields. This is done next in chapter III.

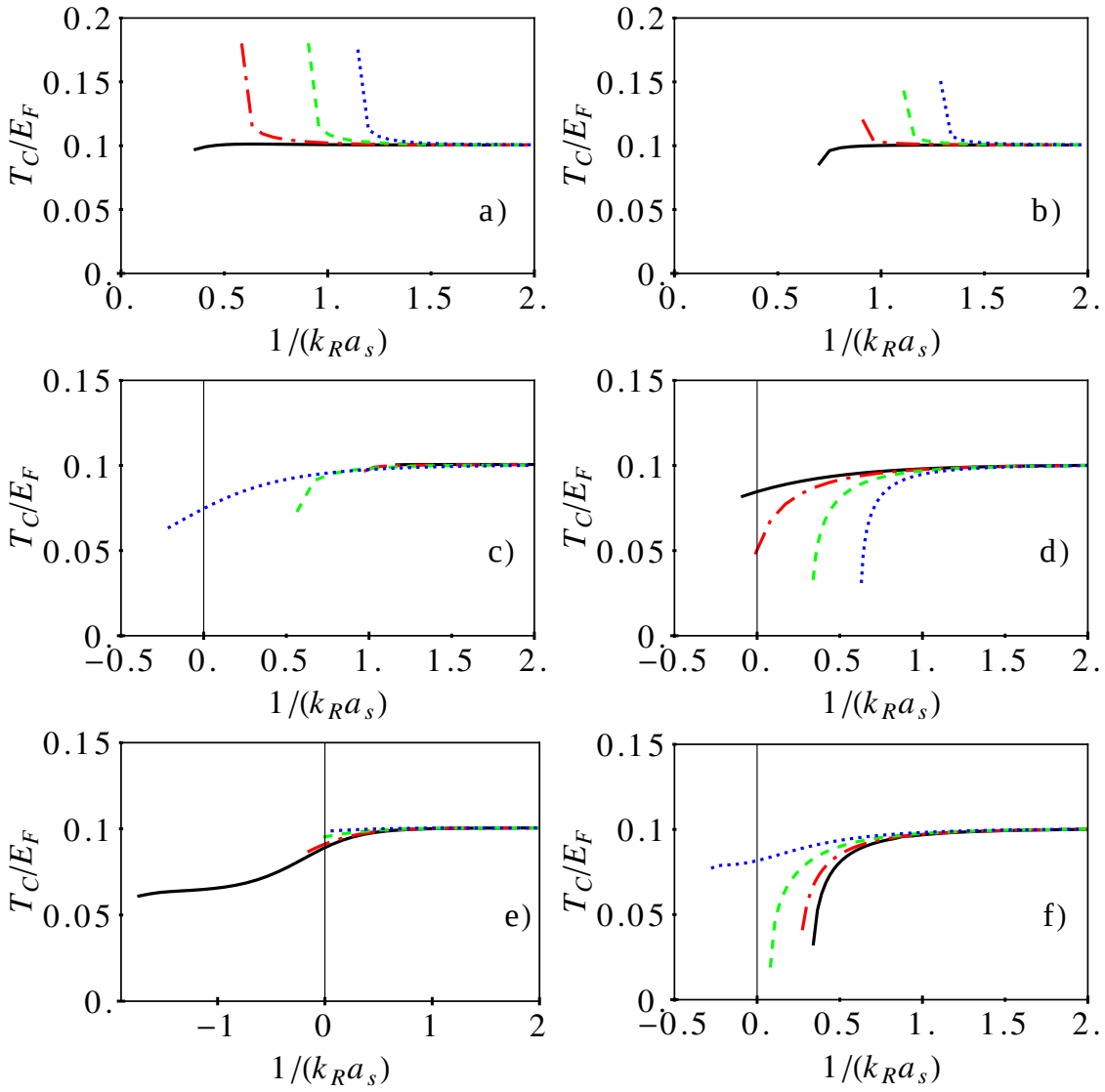

Figure 2.13: Plots of $T_c = T_{BEC}/2$, where T_{BEC} is the Bose-Einstein condensation temperature, in units of the Fermi energy E_F. The top panels refer to the ERD case, the middle panels refer to the Rashba case, and the bottom panels refer to a more generic mixture of Rahsa and Dresselhaus terms. For the top panels the parameters used are $h_z = 0.5E_R$ [left] and $h_z = 1.5E_R$ [right] with $v = k_R/m$ and $h_y = 0.5E_R$ (black-solid), $h_y = E_R$ (green-dashed), $h_y = 1.5E_R$ (red-dot dashed) and $h_y = 2E_R$ (blue-dotted). For the middle panels the parameters used are [left] $h_z = 0.5E_R$ with $v_R = k_R/m$ and $h_y = 0.5E_R$ (black-solid), $h_y = E_R$ (green-dashed), $h_y = 1.5E_R$ (red-dot dashed) and $h_y = 2E_R$ (blue-dotted); [right] $h_z = 1.5E_R$ and $h_y = 0E_R$ with $v_R = 0.25k_R/m$ (black-solid), $v_R = 0.5k_R/m$ (red-dot dashed), $v_R = 0.75k_R/m$ (green-dashed), $v_R = k_R/m$ (blue-dotted). For the bottom panels the parameters used are $v_D = 0.0001k_R/m$ (black-solid), $v_D = 0.1k_R/m$ (red-dot dashed), $v_D = 0.2k_R/m$ (green-dashed) and $v_D = 0.3k_R/m$ (blue-dotted) for the Dresselhaus velocities. For the left panel, the Zeeman fields are $h_z = 0E_R$, $h_y = 0E_R$, and the Rashba velocity $v_R = 0.5k_R/m$ while for the right panel $h_z = 0.5E_R$, $h_y = 1.5E_R$, and $v_R = k_R/m$

CHAPTER III

EFFECTS OF A HARMONIC TRAP ON TWO-BODY BOUND STATES IN THE PRESENCE OF SPIN-ORBIT COUPLING

In chapter II, I discussed the emergence of two-body bound states for fermions in the presence of artificial spin-orbit coupling and Zeeman fields, but in free space. In that case, I took advantage of translational invariance to derive a integral equation for the bound-state eigenvalues in momentum space. However, to apply the previous results more directly to ultra-cold fermions it is necessary necessary to include also the effects of a harmonic potential, which is one of the typical potentials used experimentally to trap atoms. Therefore, in this chapter I will add an isotropic harmonic potential in three-dimensions and solve the resulting Schroedinger's equation in real space.

Several methodological differences will be implemented in this chapter in comparison to chapter II. Given that I will be working always in real space when the harmonic trap is added, the tools used to solve this problem are different that those used in chapter II, when the harmonic trap was absent. For instance, I will introduce the Fermi-Huang pseudo-potential to connect the contact interaction to the s-wave scattering length. Furthermore, I will confine myself to the case of ERD (equal-Rashba-Dresselhaus) spin-orbit coupling only, which is currently the most relevant from the experimental point of view. Finally, I will also add the effects of a Zeeman field, because in ultra-cold fermions, the artificial spin-orbit coupling is always created in the presence of a finite Zeeman field, which can be made small, but not turned off completely.

The remainder of this chapter is organized as follows, the Fermi-Huang potential

is discussed in section 3.1, while the model Hamiltonian describing two fermions in a harmonic potential and in the presence of ERD spin-orbit coupling is discussed in section 3.2. The eigenvalues of Schroedinger's equation in the presence of spin-orbit coupling without Zeeman fields are obtained in section 3.3, and with Zeeman fields are obtained in section 3.4. Lastly, I will present the main conclusions of this chapter in section 3.5.

3.1 Derivation of Fermi-Huang Pseudo-Potential

In this section, I will derive the Fermi-Huang pseudo-potential, which connects the amplitude of a contact potential between two atoms. Provided that the atoms interact only via effective short-ranged forces, which is the case in neutral ultra-cold fermions, the Fermi-Huang pseudo-potential is an excellent approximation to describe atom-atom interactions in three dimensions.

I will briefly skecth the derivation of the Fermi-Huang potential for two interacting particles (without including their *spin* degrees of freedom. Let me start from the Hamiltonian

$$\hat{H}\psi = (\hat{T} + \hat{V})\psi = E\psi, \tag{3.1}$$

where $\hat{T}$ is the kinetic energy operator, $\hat{V}$ is the two-particle potential, E is the energy eigenvalue and ψ is the two-particle wavefunction. More explicitly the Schroedinger's equation becomes

$$\hat{H}\psi(\mathbf{r}_1, \mathbf{r}_2) = \left[-\frac{\nabla_1^2}{2m} - \frac{\nabla_2^2}{2m} + V\Big(|\mathbf{r}_1 - \mathbf{r}_2|\Big) \right] \psi(\mathbf{r}_1, \mathbf{r}_2), \tag{3.2}$$

where I chose to work with units $\hbar = 1$.

A transformation of coordinates from $\mathbf{r}_1$ and $\mathbf{r}_2$ to relative $\mathbf{r} = \mathbf{r}_1 - \mathbf{r}_2$ and center-of-mass $\mathbf{R} = (\mathbf{r}_1 + \mathbf{r}_2)/2$ coordinates leads to the separable Schroedinger's equation

$$\begin{aligned} \left(-\frac{\nabla_{\mathbf{r}}^2}{m} - \frac{\nabla_{\mathbf{R}}^2}{4m} + V(\mathbf{r}) \right) \psi(\mathbf{r}, \mathbf{R}) = -\Phi(\mathbf{R}) \frac{\nabla_{\mathbf{r}}^2}{m} \phi(\mathbf{r}) + ... \\ ... - \phi(\mathbf{r}) \frac{\nabla_{\mathbf{R}}^2}{4m} \Phi(\mathbf{R}) + V(\mathbf{r}) \Phi(\mathbf{R}) \phi(\mathbf{r}), \end{aligned} \tag{3.3}$$

where I made use of the two-body wavefunction being written as $\psi(\mathbf{r}, \mathbf{R}) = \phi(\mathbf{r})\Phi(\mathbf{R})$, with $\Phi(\mathbf{R})$ being associated with the center of mass and $\phi(\mathbf{r})$ being associated with the relative coordinate.

The energy eigenvalue can also be separated as in term of the relative energy E_r and the center of mass energy E_R as $E = E_r + E_R$. The center-of-mass equation is simply

$$-\frac{1}{\phi(\mathbf{R})}\frac{\nabla^2_{\mathbf{R}}}{4m}\Phi(\mathbf{R}) = E_R, \tag{3.4}$$

and the eigenfunctions are just plane waves. The resulting Schroedinger's equation for the relative coordinate becomes

$$-\frac{1}{m}\nabla^2_{\mathbf{r}}\phi(\mathbf{r}) + V(\mathbf{r})\phi(\mathbf{r}) = E_r\phi(\mathbf{r}). \tag{3.5}$$

To obtain the form of the pseudo-potential, it is convenient to look first at the zero energy $E_r = 0$ solutions of Eq. 3.5. If $\mathbf{r} \neq 0$, our interaction potential $V(\mathbf{r}) = 0$, and s-wave solutions for zero energy become

$$-\frac{1}{m}\nabla^2_{\mathbf{r}}\phi(\mathbf{r}) = 0 \rightarrow \phi(\mathbf{r}) = A - \frac{B}{r}. \tag{3.6}$$

The s-wave scattering length a_s is defined as the length at which the wavefunction solution above vanishes. Therefore the wavefunction at zero relative energy reduces to

$$\phi(\mathbf{r}) = A\left(1 - \frac{a_s}{r}\right) \tag{3.7}$$

where $r = |\mathbf{r}|$, and A plays the role of a normalization constant.

The Fermi-Huang pseudo-potential is found from the Schroedinger's equation

$$-\frac{1}{m}\nabla^2_{\mathbf{r}}\phi(\mathbf{r}) + V(r)\phi(\mathbf{r}) = 0 \tag{3.8}$$

as $\mathbf{r} \rightarrow 0$. Using the wavefunction of Eq. (3.7) and the identity $\nabla^2_{\mathbf{r}}(1/r) = -4\pi\delta(\mathbf{r})$ the resulting relation is obtained

$$\frac{4\pi a_s}{m}\delta(\mathbf{r}) + V(\mathbf{r})\left(1 - \frac{a}{r}\right) = 0. \tag{3.9}$$

Notice that this relation is always satisfied if the potential is chosen to be

$$V(\mathbf{r}) = -\frac{4\pi a_s}{m}\delta(\mathbf{r})\frac{\partial}{\partial r}\left(r...\right), \tag{3.10}$$

which is known as the Fermi-Huang potential.

Since I am interested in the formation of bound states between atomic fermions in different hyperfine states (opposite *spins*) and in the presence of a harmonic potential, the atom-atom interaction potential will take the form

$$\hat{H}_I(\mathbf{r}) = -\frac{4\pi a_s}{m}\delta(\mathbf{r})\frac{\partial}{\partial r}\left(r...\right)|00\rangle\langle 00| = -g\delta(\mathbf{r})\frac{\partial}{\partial r}\left(r...\right)|00\rangle\langle 00| \tag{3.11}$$

where the bare coupling constant is $g = 4\pi a_s/m$, and the singlet sector "ket" is $|00\rangle = (|\uparrow\downarrow\rangle - |\downarrow\uparrow\rangle)/\sqrt{2}$.

Having discussed the Fermi-Huang pseudo-potential, next I will make use of it to analyse the eigenvalues of two-fermions confined in a harmonic potential and in the presence of ERD spin-orbit coupling.

3.2 Model Hamiltonian: Two Fermions in a Harmonic Trap

In this section, I will discuss the Schroedinger equation for two fermions in a harmonic trap and at the same time in the presence of ERD spin-orbit coupling. As discussed in chapters I and II, the ERD spin-orbit field experienced by the i^{th} spin-1/2 fermion is

$$\mathbf{h}_i = v\hat{p}_{x_i}\mathbf{e}_y = -iv\partial_{x_i}\mathbf{e}_y, \tag{3.12}$$

leading to a spin-orbit coupling Hamiltonian

$$\hat{H}_{so} = -\mathbf{h}_1\cdot\boldsymbol{\sigma}_1 - \mathbf{h}_2\cdot\boldsymbol{\sigma}_2 \tag{3.13}$$

where $\boldsymbol{\sigma} = \sigma_x\mathbf{e}_x + \sigma_y\mathbf{e}_y + \sigma_z\mathbf{e}_z$ with $\{\sigma_x, \sigma_y, \sigma_z\}$ being the standard Pauli matrices.

The harmonically confining potential in three dimensions is chosen to be spherically symmetrically

$$H_{ha}(\mathbf{r}_1, \mathbf{r}_2) = \frac{1}{2}m\omega^2\left(\mathbf{r}_1^2 + \mathbf{r}_2^2\right) \tag{3.14}$$

and independent of the internal degrees of freedom (*spin*) of the fermions. Here, the vector $\mathbf{r}_i = x_i\mathbf{e}_x + y_i\mathbf{e}_y + z_i\mathbf{e}_z$ represents the displacement of particle i from the origin of the harmonic potential.

I will construct the Hamiltonian matrix for the system of two-particles by recalling that the wavefunctions can be represented by the four component spinor

$$\mathbf{\Psi}^\dagger = \Big(\psi^*_{\uparrow\uparrow}(\mathbf{r}_1,\mathbf{r}_2), \psi^*_{\uparrow\downarrow}(\mathbf{r}_1,\mathbf{r}_2), \psi^*_{\downarrow\uparrow}(\mathbf{r}_1,\mathbf{r}_2), \psi^*_{\downarrow\downarrow}(\mathbf{r}_1,\mathbf{r}_2)\Big), \tag{3.15}$$

where the $\uparrow$ represents hyperfine state *up* and the $\downarrow$ represents hyperfine state *down*. In this case, the non-interacting part of the total Hamiltonian matrix corresponds to

$$\mathbf{H}_{non} = \mathbf{K} + \mathbf{H}_{so} + \mathbf{H}_{ze} + \mathbf{H}_{ha}, \tag{3.16}$$

where the first term

$$\mathbf{K} = -\frac{1}{2m}\nabla_1^2\mathbf{1}\otimes\mathbf{1} - \frac{1}{2m}\nabla_2^2\mathbf{1}\otimes\mathbf{1} \tag{3.17}$$

corresponds to the kinetic energy contribution,

$$\mathbf{H}_{so} = -v\left(\hat{p}_{x_1}\boldsymbol{\sigma}_y\otimes\mathbf{1} + \hat{p}_{x_2}\mathbf{1}\otimes\boldsymbol{\sigma}_y\right) \tag{3.18}$$

corresponds to the ERD spin-orbit coupling,

$$\mathbf{H}_{ze} = -h_z(\boldsymbol{\sigma}_z\otimes\mathbf{1} + \mathbf{1}\otimes\boldsymbol{\sigma}_z,) \tag{3.19}$$

corresponds to the Zeeman term, and

$$\mathbf{H}_{ha} = \frac{1}{2}m\omega^2\left[(x_1^2+y_1^2+z_1^2)\mathbf{1}\otimes\mathbf{1} + (x_2^2+y_2^2+z_2^2)\mathbf{1}\otimes\mathbf{1}\right] \tag{3.20}$$

corresponds to the harmonic potential experienced by the two particles. The symbol $\otimes$ denotes direct product.

The next step in making the Hamiltonian more treatable is to perform the transformation from particle coordinates $\mathbf{r}_1$ and $\mathbf{r}_2$ to relative $\mathbf{r} = \mathbf{r}_1 - \mathbf{r}_2$ and center of mass coordinates $\mathbf{R} = (\mathbf{r}_1 + \mathbf{r}_2)/2$, therefore leading to the Schroedinger's equation

$$(\mathbf{H}_{non} + \mathbf{H}_I)\,\mathbf{\Psi}(\mathbf{r},\mathbf{R}) = E\mathbf{\Psi}(\mathbf{r},\mathbf{R}). \tag{3.21}$$

It is more convenient to rearrange equation above to isolate the the interaction part on the right hand side as

$$\left(\mathbf{H}_{non} - E\right)\mathbf{\Psi}(\mathbf{r},\mathbf{R}) = -\mathbf{H}_I\mathbf{\Psi}(\mathbf{r},\mathbf{R}). \tag{3.22}$$

The construction of all these matrices can be performed using the direct product rules shown in Appendix I.

The simplest terms in the Hamiltonian matrix are those that do not contain Pauli matrices, and are therefore *spin* independent involving the product $\mathbf{1}\otimes\mathbf{1} = \mathbf{1}_4$. The part of $\mathbf{H}_{non}$ which is *spin* independent involves the sum of the kinetic energy matrix $\mathbf{K}$ and the harmonic potential matrix $\mathbf{H}_{ha}$ as shown in

$$\mathbf{H}_0 = \left(\hat{K} + \frac{1}{2}m\omega^2(r^2+4R^2) - E\right)\mathbf{1}\otimes\mathbf{1}, \tag{3.23}$$

where $\hat{K} = -\nabla^2_{\mathbf{r}}/m - \nabla^2_{\mathbf{R}}/(2m)$ is the kinetic energy operator.

The terms that contain the Pauli matrices are also easy to obtain with the direct products shown in Appendix I. I will just illustrate below the explicit form of $\mathbf{H}_{so}$, while the matrix $\mathbf{H}_{ze}$ can be obtained in a similar fashion. The spin-orbit Hamiltonian matrix is

$$\mathbf{H}_{so} = -v\hat{p}_{x_1}\boldsymbol{\sigma}_y\otimes\mathbf{1} - v\hat{p}_{x_2}\mathbf{1}\otimes\boldsymbol{\sigma}_y, \tag{3.24}$$

with the matrices representing the direct products given by

$$v\hat{p}_{x_1}\boldsymbol{\sigma}_y\otimes\mathbf{1} = v\hat{p}_{x_1}\begin{pmatrix} 0 & 0 & -i & 0 \\ 0 & 0 & 0 & -i \\ i & 0 & 0 & 0 \\ 0 & i & 0 & 0 \end{pmatrix} \quad ; \quad v\hat{p}_{x_2}\mathbf{1}\otimes\boldsymbol{\sigma}_y = v\hat{p}_{x_2}\begin{pmatrix} 0 & -i & 0 & 0 \\ i & 0 & 0 & 0 \\ 0 & 0 & 0 & -i \\ 0 & 0 & i & 0 \end{pmatrix}.$$

Before starting to solve the problem, it is convenient to convert the Hamiltonian matrix $\mathbf{H}_{non}$ described in Eq. (3.16 into the singlet-triplet basis, as it was done in chapter II. The reason again is the same as before, the interaction part of the Hamiltonian involves only the singlet sector, while the spin-orbit part of the hamiltonian

can cause transitions between the singlet and triplet sectors. Therefore, I perform the basis change $\mathbf{\Phi} = \mathbf{U}\mathbf{\Psi}$, which in matrix form corresponds to

$$\begin{pmatrix} \psi_{11} \\ \psi_{10} \\ \psi_{1-1} \\ \psi_{00} \end{pmatrix} = \begin{pmatrix} 1 & 0 & 0 & 0 \\ 0 & 1/\sqrt{2} & 1/\sqrt{2} & 0 \\ 0 & 0 & 0 & 1 \\ 0 & 1/\sqrt{2} & -1/\sqrt{2} & 0 \end{pmatrix} \begin{pmatrix} \psi_{\uparrow\uparrow} \\ \psi_{\uparrow\downarrow} \\ \psi_{\downarrow\uparrow} \\ \psi_{\downarrow\downarrow} \end{pmatrix}, \tag{3.25}$$

where the matrix $\mathbf{U}$ is unitary having the property $\mathbf{U}^\dagger\mathbf{U} = \mathbf{1}_4$ and its determinant is one, that is, Det$\mathbf{U} = 1$.

Under this transformation the spin-independent part of the total Hamiltonian $\mathbf{H}_0$ is invariant since it is proportional to the identity matrix $\mathbf{1}_4$, that is to $\mathbf{1} \otimes \mathbf{1} = \mathbf{1}_4$, leading to the unitary transformation $\mathbf{U}\mathbf{1}_4\mathbf{U}^\dagger = \mathbf{1}_4$. However, the spin-dependent part of the hamiltonian does not stay the same. For instance, the spin-orbit part $\mathbf{H}_{so}$ transforms as $\mathbf{U}\mathbf{H}_{so}\mathbf{U}^\dagger = \mathbf{H}'_{so}$ leading to the matrix

$$\mathbf{H}'_{so} = v \begin{pmatrix} 0 & \frac{i}{\sqrt{2}}(\hat{p}_{x_1} + \hat{p}_{x_2}) & 0 & \frac{i}{\sqrt{2}}(\hat{p}_{x_1} - \hat{p}_{x_2}) \\ -\frac{i}{\sqrt{2}}(\hat{p}_{x_1} + \hat{p}_{x_2}) & 0 & \frac{i}{\sqrt{2}}(\hat{p}_{x_1} + \hat{p}_{x_2}) & 0 \\ 0 & -\frac{i}{\sqrt{2}}(\hat{p}_{x_1} + \hat{p}_{x_2}) & 0 & \frac{i}{\sqrt{2}}(\hat{p}_{x_1} - \hat{p}_{x_2}) \\ -\frac{i}{\sqrt{2}}(\hat{p}_{x_1} - \hat{p}_{x_2}) & 0 & -\frac{i}{\sqrt{2}}(\hat{p}_{x_1} - \hat{p}_{x_2}) & 0 \end{pmatrix}. \tag{3.26}$$

Notice that, as a bonus, this process also decomposes the spin-orbit part in term of the center of mass and relative momentum operators, as can be seen explicitly from the matrix elements above.

Using all the direct product matrices (see Appendix I) and appplying the unitary transformation to rotate the matrices to a single-triplet basis lead to the Schroendinger's

matrix equation

$$\begin{pmatrix} \hat{\mathcal{E}}_{r,R}-2h_z & \frac{i}{\sqrt{2}}v\hat{P}_x & 0 & i\sqrt{2}v\hat{k}_x \\ -\frac{i}{\sqrt{2}}v\hat{P}_x & \hat{\mathcal{E}}_{r,R} & -\frac{i}{\sqrt{2}}v\hat{P}_x & 0 \\ 0 & \frac{i}{\sqrt{2}}v\hat{P}_x & \hat{\mathcal{E}}_{r,R}+2h_z & i\sqrt{2}v\hat{k}_x \\ -i\sqrt{2}v\hat{k}_x & 0 & -i\sqrt{2}v\hat{k}_x & \hat{\mathcal{E}}_{r,R} \end{pmatrix} \begin{pmatrix} \psi_{11} \\ \psi_{10} \\ \psi_{1-1} \\ \psi_{00} \end{pmatrix} = \begin{pmatrix} 0 \\ 0 \\ 0 \\ g\delta(\mathbf{r})\partial_r(r\psi_{00}) \end{pmatrix} \quad (3.27)$$

where the operator appearing in the diagonal matrix elements is

$$\hat{\mathcal{E}}_{r,R} \equiv -\frac{1}{m}\nabla_r^2 - \frac{1}{4m}\nabla_R^2 + H_{ha} - E, \quad (3.28)$$

with $H_{ha} = m\omega^2(r^2+4R^2)/2$ being the sum of the harmonic potentials felt by particles 1 and 2 written in relative and center of mass coordinates. Here, $\hat{\mathbf{P}}$ is the center of mass momentum operator and $\hat{\mathbf{k}}$ is relative momentum operator.

It is important to notice that after the introduction of spin-orbit coupling the relative and center-of-mass degrees of freedom are not separable, thus making a general analytical solution of the problem difficult. However, progress can be made by solving the problem in the center-of-mass momentum reference frame, where I set its origin to be at $\mathbf{R} = \mathbf{0}$ and where the center of mass momentum is set to zero ($\mathbf{P} = \mathbf{0}$). Having this in mind, I will first solve the resulting Schroedinger's equation for the case of zero Zeeman field ($h_z = 0$) in the next section, and then in section 3.4 I will add the Zeeman field back to the problem.

3.3 Energy Eigenvalues Without Zeeman Fields

In this section, I will obtain the eigenvalues of two fermions in the presence of a harmonic potential and ERD spin-orbit coupling, but without Zeeman fields.

By applying the Gauss elimination method to the Schroedinger's equation shown in Eq. (6.8), I arrive at the differential equation

$$\hat{\mathcal{E}}_r\psi_{00}(\mathbf{r},\mathbf{0}) + 4v^2\partial_{r_x}^2\hat{\mathcal{E}}_r^{-1}\psi_{00}(\mathbf{r},\mathbf{0}) = g\delta(\mathbf{r})\frac{\partial}{\partial r}\left[r\psi_{00}(\mathbf{r},\mathbf{0})\right] \quad (3.29)$$

where the operator $\hat{\mathcal{E}}_r \equiv -\frac{1}{m}\nabla_r^2 + \frac{1}{2}m\omega^2\mathbf{r}^2 - E$. Notice that Eq. (3.29) reduces to the previously known expression [18] when the spin-orbit coupling is set to zero, that is, in the $v = 0$ limit.

Taking advantage of the hermiticity of $\hat{\mathcal{E}}_r$, I will write the operator $\hat{\mathcal{E}}_r^{-1}$, appearing in the spin-orbit term, via an integral representation over imaginary time leading to

$$\hat{\mathcal{E}}_r\psi_{00}(\mathbf{r},\mathbf{0}) + 4v^2\partial_{r_x}^2\int_0^\infty d\tau e^{-\tau\hat{\mathcal{E}}_r}\psi_{00}(\mathbf{r},\mathbf{0}) = g\delta(\mathbf{r})\frac{\partial}{\partial r}\left[r\psi_{00}(\mathbf{r},\mathbf{0})\right]. \tag{3.30}$$

To solve the differential equation above, I expand the unknown singlet $\psi_{00}(\mathbf{r},\mathbf{0})$ wave function

$$\psi_{00}(\mathbf{r},\mathbf{0}) = \sum_N c_N\phi_N(\mathbf{r}) \tag{3.31}$$

in terms of harmonic oscillator eigenfunctions, which satisfy the equation

$$H_{ha}(\mathbf{r},\mathbf{R}=\mathbf{0})\phi_N(\mathbf{r}) = \epsilon_N\phi_N(\mathbf{r}) \tag{3.32}$$

where $\epsilon_N = \omega(2n + \ell + 3/2)$ are the energy eigenvalues for the three dimensional harmonic oscillator. The quantum numbers are given by the set $\{N\} = \{n, \ell\}$, where n is the principal quantum number and ℓ is the angular momentum quantum number.

Since the interactions between the fermions (Fermi atoms) occurs via an s-wave singlet channel, as a first approximation, I will include only the $\ell = 0$ contributions in the expansion for $\psi_{00}(\mathbf{r},\mathbf{0})$. In this case, the eigenfunctions with $\ell = 0$ are

$$\phi_n(\mathbf{r}) = \mathcal{N}_n e^{-\zeta r^2} L_n^{(1/2)}(2\zeta r^2) \tag{3.33}$$

where $\mathcal{N}_n$ is a normalization constant, $\zeta = m\omega/4$, and the functions $L_n^{(1/2)}(x)$ are generalized Laguerre polynomials with $\ell = 0$, which obey the following orthogonality condition

$$\int_0^\infty L_n^{(k)}(x)L_m^{(k)}(x)x^k e^{-x}dx = \frac{(n+k)!}{n!}\delta_{nm}. \tag{3.34}$$

The use of the recurrence relation

$$\frac{d}{dx}L_n^{(k)}(x) = x^{-1}\left(nL_n^{(k)}(x) - (n+k)L_{n-1}^{(k)}(x)\right) \tag{3.35}$$

and the orthogonality relation of Eq. (3.34) leads to the following normalization constant

$$\mathcal{N}_n = \left(\frac{\pi}{\sqrt{2}\zeta^{3/2}}\frac{(n+1/2)!}{n!}\right)^{-1/2} \tag{3.36}$$

A substitution of the eigenfunctions $\phi_n(\mathbf{r})$ in Eq. (3.29), with posterior integration over imaginary time, and projection into the eigenfunction $\phi_a^*(\mathbf{r})$ leads to the intermediate result

$$\begin{aligned} c_a\left(\epsilon_a - E\right) + 4v^2\sum_k \frac{c_k}{\epsilon_k - E}\int d\mathbf{r}\phi_a^*(\mathbf{r})\partial_{r_x}^2\phi_k(\mathbf{r}) = ... \\ ... = g\sum_p \int d\mathbf{r}\phi_a^*(\mathbf{r})\delta(\mathbf{r})\partial_r[r\phi_p(\mathbf{r})], \end{aligned} \tag{3.37}$$

where the integral appearing in the second term on the left hand side is evaluated in Appendix X.

In the limit where the spin-orbit coupling energy mv^2 is small in comparison to adjacent energy levels of the harmonic oscillator, the expression above reduces to

$$c_a\left[(\epsilon_a - E) - \frac{m\omega v^2}{\epsilon_a - E}\left(\frac{4a}{3} + \frac{5}{3}\right)\right] = -\frac{4\pi}{m}a_s\phi_a^*(\mathbf{0})\left[\frac{\partial}{\partial r}\left(r\sum_{p=0}^{\infty}c_p\phi_p(\mathbf{r})\right)\right]\Bigg|_{r\to 0}, \tag{3.38}$$

which corresponds to a infinite linear system of equations coupling the coefficient c_a of the harmonic oscillator state ϕ_a to all other coefficients c_p, given by

$$c_a = -\frac{4\pi a_s}{m}\phi_a^*(0)\left[\frac{\partial}{\partial r}\left(r\sum_{p=0}^{\infty}c_p\phi_p(\mathbf{r})\right)\right]\Bigg|_{r\to 0}\left(\frac{\epsilon_a - E}{(\epsilon_a - E)^2 - \frac{mv^2\omega}{3}(4a+5)}\right). \tag{3.39}$$

This linear system can be solved analytically to give

$$c_a = \frac{A}{\omega}\left(\frac{B_+}{2a - \nu_+} + \frac{B_-}{2a - \nu_-}\right)\phi_a^*(0), \tag{3.40}$$

where I used the relation $\epsilon_a = \omega(2a + 3/2)$. The coefficient A is obtained by normalization of the overall wavefunction, while $\mu = mv^2/3\omega$ and $\nu_\pm = E/\omega + \mu - 3/2 \pm \eta$,

with $\eta = \sqrt{\mu^2 + 2\mu + 2\mu E/\omega}$. leading to coefficients $B_\pm = (\pm\mu + \eta)/(2\eta)$. Notice that in the limit of $v \to 0$ then $B_\pm \to 1/2$.

By making use of the solutions for the coefficents c_a shown in Eq. (3.40) and inserting them back into Eq. (3.39), an implicit relation between the scattering length a_s, the spin-orbit coupling v and the eigenenergies E is revealed

$$-\frac{m}{4\pi a_s} = \sum_{\lambda=\pm} B_\lambda \left[\frac{\partial}{\partial r}\left(r \sum_{p=0}^{\infty} \frac{\phi_p^*(0)\phi_p(\mathbf{r})}{2p - \nu_\lambda}\right)\right]\Bigg|_{r\to 0}, \tag{3.41}$$

since ν_λ and B_λ are functions of v and E.

Using the explicit form of the eigenfunction $\phi_p(\mathbf{r})$ of the harmonic oscillators in Eq. (3.33), taking the spatial derivative with respect to r and performing the summation over the quantum numbers p leads to the final expression

$$\frac{\sqrt{2}}{a_s\sqrt{m\omega}} = B_- \frac{\Gamma(-\nu_-/2)}{\Gamma(-\nu_-/2 - 1/2)} + B_+ \frac{\Gamma(-\nu_+/2)}{\Gamma(-\nu_+/2 - 1/2)}, \tag{3.42}$$

which relates the scattering length a_s to the energy eigenvalues E for different values of the spin-orbit coupling v, via the Gamma function $\Gamma(z)$. It is this expression that is the central result of this section, and its detailed derivation can be found in Appendix IX.

Using the expression obtained in Eq. (3.42), I plot the inverse of the s-wave scattering length $1/a_s$ versus energy in Fig. (3.1) for the case of zero spin-orbit coupling $v = 0$. The units used in Fig. (3.1) and subsequent figures are such that the fermion mass is $m = 1$ and the frequency of the harmonic oscillator is $\omega = 1$. The result for $v = 0$ coincides with previously known behavior [18]. Notice that when the spin-orbit coupling effect is absent, divergences occur in the inverse scattering length $1/a_s$ precisely at energies $E/\omega = 3/2, 5/2, 7/2...$, which correspond to the eigenvalues of the harmonic oscillator. It is important to notice that when the harmonic potential is present, the energy threshold for the formation of bound states is shifted from 0 in the continuum case (no harmonic potential) to $E_{th}/\omega = 3/2$. In addition, the presence of the harmonic potential enhances dramatically (at the threshold energy) the density

of states avaialable for the formation of two-body bound states. Therefore, two-body bound states can be formed below this threshold for small and negative values of the scattering length a_s, unlike in the continuum case that requires $a_s \geq 0$ for bound state formation. Notice also that when $E \to -\infty$, then $E = -1/ma_s^2$, describing the energy of the two-body bound state in that regime, since the energy of the harmonic potential becomes irrelevant in that limit.

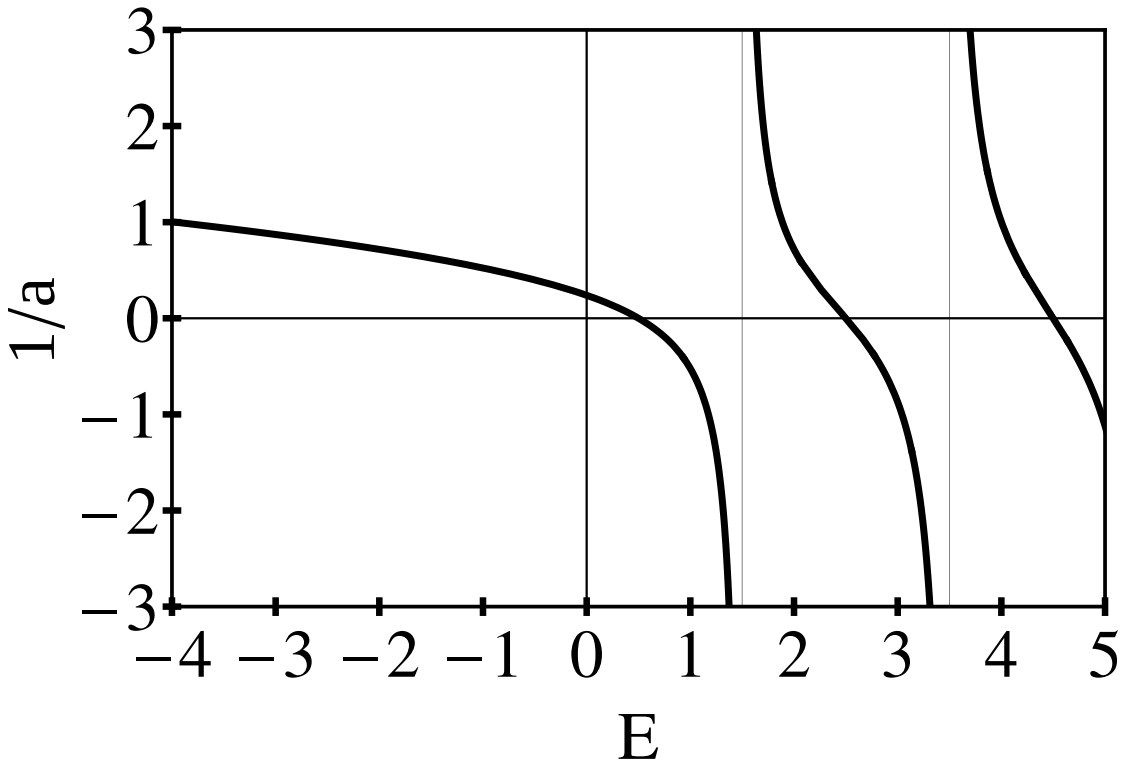

Figure 3.1: Plot of the inverse s-wave scattering length $(1/a_s)$ versus energy when no spin-orbit coupling $(v = 0)$ and Zeeman fields $(h_z = 0)$ are present.

Using again the expression obtained in Eq. (3.42), I plot the inverse of the s-wave scattering length $1/a_s$ versus energy in Fig. (3.2) for the case of zero spin-orbit coupling $v \neq 0$. In this case, the location of the divergences in $1/a_s$ are shifted with respect to the location of harmonic oscillator energies $\epsilon_n = \omega(2n + 3/2)$. The energy shifts are approximately equal to $\pm mv^2/3$ and the location of the divergences in $1/a_s$ are moved to energy values $E_\pm = \omega(2n+3/2) \pm mv^2/3$, with n being an integer. This

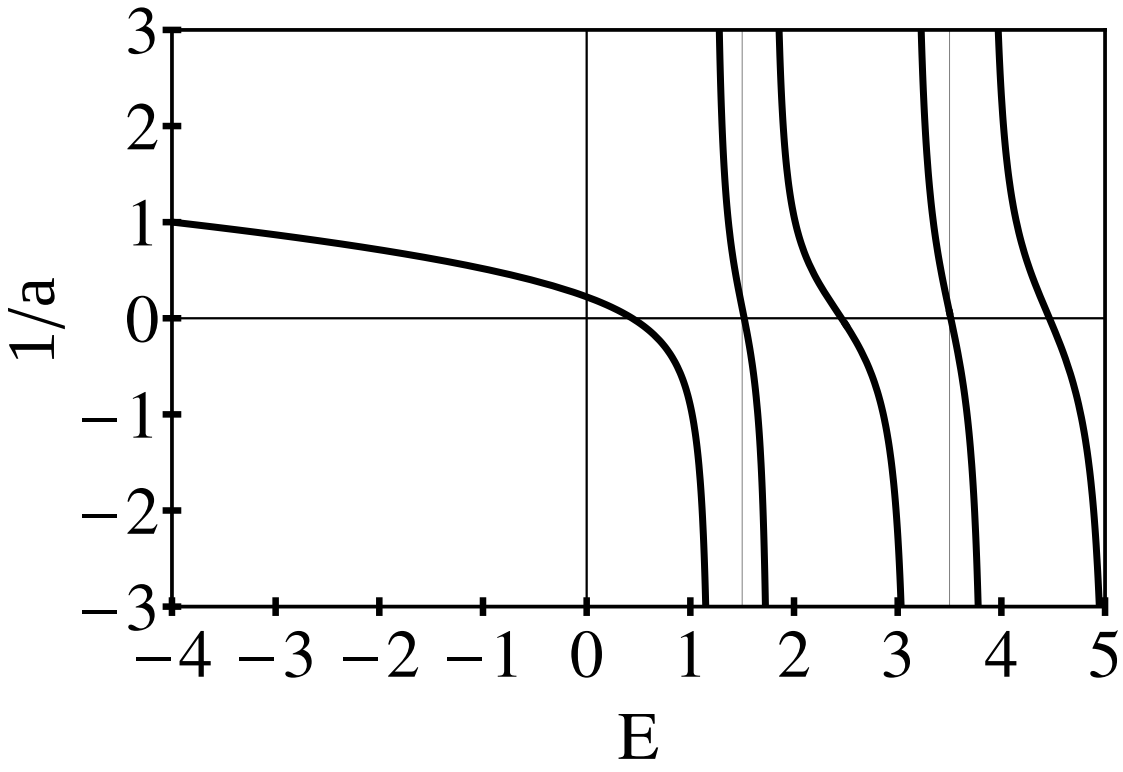

Figure 3.2: Plots of the inverse s-wave scattering length $(1/a_s)$ versus energy with ERD type of spin-orbit coupling with $v = 0.2$ (using units of mass $m = 1$ and frequency $\omega = 1$) and no Zeeman field, $h_z = 0$.

splitting occurs because the presence of spin-orbit coupling fields lifts the degeneracy between the *spin* up and the *spin* down states. Notice that even with level splittings, the density of states available for bound state to form is sufficiently high, that even a small and negative scattering length a_s can lead to their formation. This is in constrast to the continuum case found in chapter II, where $a_s \geq 0$ is required for bound state formation for the ERD case. Furthemore, in the limit of $E \to -\infty$, $E = -1/ma_s^2 - mv^2$ describes the energy of the two-body bound state in that regime, since the energy of the harmonic potential becomes unimportant.

Having described how the presence of a harmonic potential affects the bound states between two fermions with attractive s-wave contact interactions and in the presence of ERD spin-orbit coupling fields, I will next add the action of Zeeman fields. This next step is important, because Zeeman fields are always simultaneously present

in the experimental case where artificial ERD spin-orbit coupling have been created, as they represent the Rabi frequency of the Raman process.

3.4 Energy Eigenvalues in the Presence of Zeeman Fields

In this section, I will discuss the added effects of an artificial Zeeman field h_z representing the Rabi frequency of the Raman beams that produce the ERD spin-orbit coupling controlled by the parameter v.

Using the general Schroedinger matrix defined in Eq. (3.27) and working in the center of mass reference frame as done in section 3.4 leads to

$$\hat{\mathcal{E}}_r\psi_{00}(\mathbf{r},0)+4v^2\partial_{r_x}^2\left(\hat{\mathcal{E}}_r^2-4h_z^2\right)^{-1}\hat{\mathcal{E}}_r\psi_{00}(\mathbf{r},0)=g\delta(\mathbf{r})\frac{\partial}{\partial r}\left[r\psi_{00}(\mathbf{r},0)\right], \tag{3.43}$$

where the details leading to this expression are given in Appendix VIII.

I will employ the same technique used in section 3.4, where the singlet wavefunction $\psi_{00}(\mathbf{r},\mathbf{0})$ was expanded in terms of harmonic oscillator eigenfunctions as in Eq. (3.31). In the present case the Schroedinger's equation becomes

$$\begin{aligned}\sum_n c_n\left(\epsilon_n-E\right)\phi_n(\mathbf{r})+4v^2\partial_{r_x}^2\sum_p c_p\frac{\epsilon_p-E}{(\epsilon_p-E)^2-4h_z^2}\phi_p(\mathbf{r})=...\\ ...g\delta(\mathbf{r})\frac{\partial}{\partial_r}\left(r\sum_k c_k\phi_k\left(\mathbf{r}\right)\right),\end{aligned} \tag{3.44}$$

where h_z represents the added Zeeman field. When compared to Eq. (3.29), h_z seems to be harmless in order to make analytical progress, but unfortunately the corresponding summations and integrations that were possible to perform analytically, in part due to the spin-degeneracy of the harmonic oscillator eigenfunctions $\phi_n(\mathbf{r})$, are no longer easy to perform. Therefore to make progress, I will treat the Zeeman energy h_z as a perturbation in comparison to the energy spacing 2ω of the harmonic oscillator and obtain the equation

$$\begin{aligned}\sum_n c_n\left(\epsilon_n-E\right)\phi_n(\mathbf{r})+4v^2\partial_{r_x}^2\sum_p c_p\left[\frac{1}{(\epsilon_p-E)}+\frac{4h_z^2}{(\epsilon_p-E)^3}\right]\phi_p(\mathbf{r})=...\\ ...g\delta(\mathbf{r})\frac{\partial}{\partial_r}\left(r\sum_k c_k\phi_k\left(\mathbf{r}\right)\right)\end{aligned} \tag{3.45}$$

Projecting Eq. (3.45) into the harmonic oscillator function $\phi_a^*(\mathbf{r})$, integrating over the spatial coordinate $\mathbf{r}$, and neglecting cross-level contributions, since $h_z/(2\omega) \ll 1$, leads to

$$\begin{aligned} c_a = -\frac{4\pi}{m} a_s \phi_a^*(0) \left[\frac{\partial}{\partial r} \left(r \sum_p c_p \phi_p(\mathbf{r}, 0) \right) \right] \Bigg|_{r \to 0} \times ... \\ ... \times \frac{(\epsilon_a - E)^3}{(\epsilon_a - E)^4 - \frac{mv^2\omega}{3}(4a+5)\left[(\epsilon_a - E)^2 + 4h_z^2\right]}, \end{aligned} \tag{3.46}$$

which corresponds to an infinite linear system connecting coefficient c_a to all other coefficients c_p from the harmonic oscillator eigenfunction expansion. Notice that in the limit of $h_z \to 0$, the equation above reduces to Eq. (3.39) discussed in section 3.3.

The solution of the linear system in Eq. (3.46) has the form

$$c_a = \frac{A}{\omega} \phi_a^*(0) \sum_{i=1}^{4} \frac{(\lambda_0 + 2\lambda_i)^3}{(a - \lambda_i)} \beta_i. \tag{3.47}$$

The parameters shown in the expression above are $\lambda_0 = 3/2 - E/\omega$ and

$$\beta_i \;\; = \;\; \prod_{j \neq i}^{4} \frac{1}{\lambda_i - \lambda_j}$$

with λ_i being the roots of the dimensionless equation

$$(2a + 3/2 - \epsilon)^4 - \mu(4a+5)\left[(2a + 3/2 - \epsilon)^2 + 4\tilde{h}^2\right] = 0 \tag{3.48}$$

where $\tilde{h} = h_z/\omega$, $\epsilon = E/\omega$, $\mu = mv^2/3\omega$.

Using the expression of coefficient c_a back into the Schroedinger's equation expressed by the linear system described in Eq. (3.46) leads to a relationship between the scattering length a_s and the energy E, via the parameters λ_0, λ_i and β_i, given by

$$\frac{1}{\sqrt{2} a_s \sqrt{m\omega}} = \sum_{i=1}^{4} \beta_i \left(\lambda_0 + 2\lambda_i\right)^3 \frac{\Gamma(-\lambda_i)}{\Gamma(-\lambda_i - 1/2)}, \tag{3.49}$$

where $\Gamma(z)$ are Gamma functions of argument z. This is the central result of this section. This expression reduces to that of Eq. (3.42) when $h_z \to 0$, recovering the result found in section 3.3. It is important to mention that even if the λ_i are imaginary

numbers, the right hand side in Eq. (3.49) is real, and the resulting scattering length a_s is also real, but can be as usual positive or negative.

In Figs. 3.3 and 3.4, I show the effects of the Zeeman field for fixed spin-orbit coupling $v/(\omega/m)^{1/2} = 0.2$, in the of $h_z/\omega = 0.01$ and $h_z/\omega = 0.1$, respectively. In these figures, I use again the units of mass $m = 1$ and energy $\omega = 1$.

In Fig. 3.3, h_z is sufficiently small to verify that indeed the relation obtained in Eq. (3.49) indeed reduces to that of Eq. 3.42). The plots are, however, in a different scale than that used in Fig. 3.2 corresponding to $h_z = 0$ in section 3.4. Nevertheless, the limiting results hold. The main effect of the Zeeman field is to split further the energy states and to make the formation of two-body bound states in the singlet channel a little more difficult.

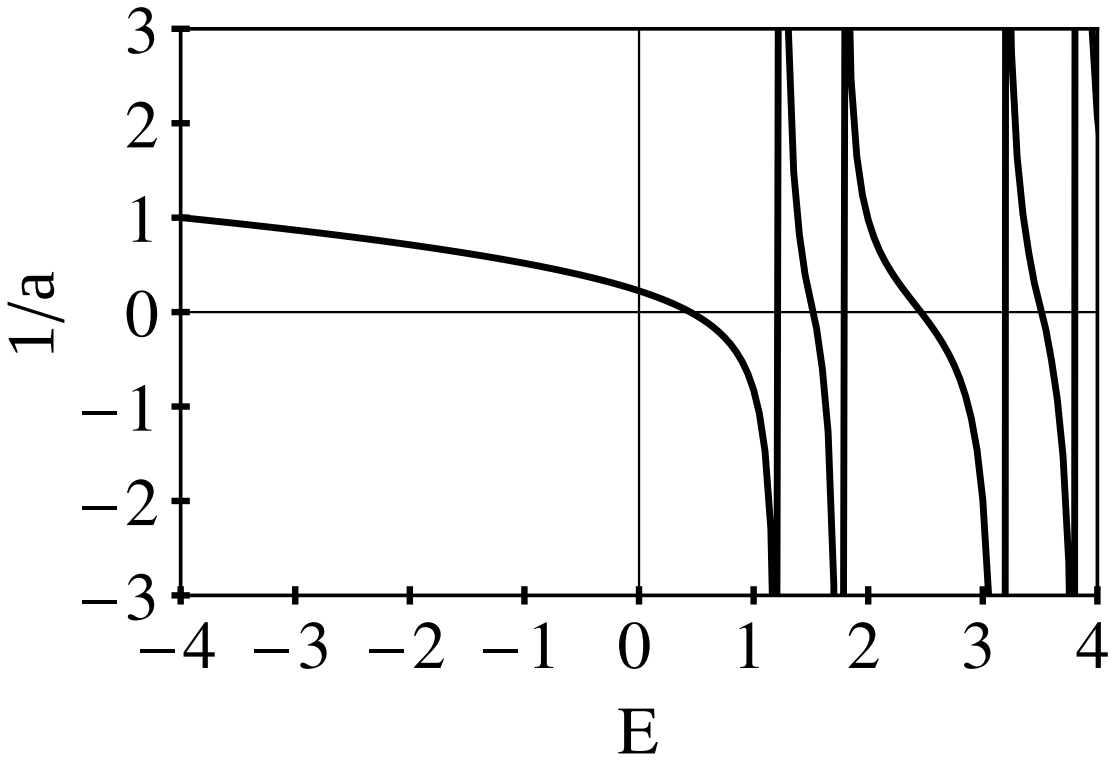

Figure 3.3: Plots of the inverse s-wave scattering length $(1/a_s)$ versus energy with ERD type of spin-orbit coupling with $v = 0.2$ (using units of mass $m = 1$ and frequency $\omega = 1$) and with Zeeman field, $h_z = 0.01$.

In Fig. 3.4, h_z is sufficiently large to show the further lifting of spin degeneracy.

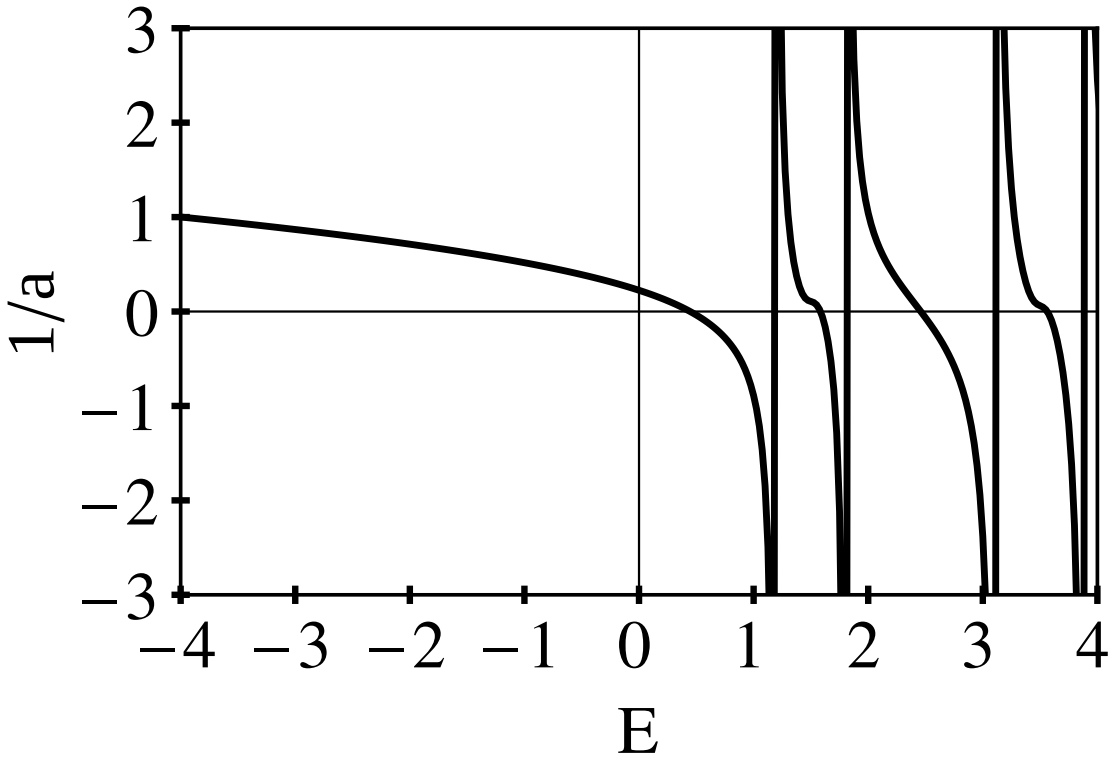

Figure 3.4: Plots of the inverse s-wave scattering length $(1/a_s)$ versus energy with ERD type of spin-orbit coupling with $v = 0.2$ (using units of mass $m = 1$ and frequency $\omega = 1$) and with Zeeman field, $h_z = 0.1$.

The plots are, however, in a different scale than that used in Fig. 3.2 corresponding to $h_z = 0$ in section 3.4. The main effect of the Zeeman field is to split further the energy states and to make the formation of two-body bound states in the singlet channel more difficult.

Having discussed in this chapter the energy eigenvalues for two fermions confined to a harmonic potential and subject to attractive contact interactions in the presence of artificial ERD spin-orbit and Zeeman fields, I will present next the main conclusions for this chapter.

3.5 Conclusions

In this chapter, I have found the energy eigenvalues for two fermions trapped in a harmonic potential and subject to attractive contact interactions, while simultaneously in the presence of artificial equal-Rashba-Dresselhaus spin-orbit coupling and Zeeman fields.

The presence of the harmonic potential alters the typical spectrum when the characteristic energy scale for the harmonic potential $\hbar\omega$ is much larger than the Zeeman energy h_z, and the spin-orbit energy mv^2. The effects of spin-orbit coupling and Zeeman fields were taken into account only in this regime, where the s-wave scattering length was analysed as function of energy.

In this chapter, the main findings were that energy levels of two harmonically trapped fermions with attractive interactions are split when the spin-orbit and Zeeman fields are present, because they lift the spin degeneracy of the system, and thus modify dramatically the relation between energy and s-wave scattering length. This effect is more prominent for energies close to those of the harmonic oscillator potential in the relative coordinate system.

Regarding the lowest possible two-particle bound state, the presence of the harmonic potential shifts the energy threshold for binding to the zero point energy of the oscillator, when no spin-orbit or Zeeman fields are included. When these latter fields are present, but are still small, then the threshold energy remains near the zero point energy. However, a small and negative scattering length is sufficient to produce the lowest two-body bound states, while in contrast such bound states can only occur for $a_s > 0$ in the three-dimensional continuum with or without ERD spin-orbit coupling present.

CHAPTER IV

ARTIFICIAL SPIN-ORBIT COUPLING IN ULTRA-COLD FERMIONS WITH THREE HYPERFINE STATES

4.1 Introduction

The field of ultra-cold atoms has been a very prolific area of research with the experimental realization of several fundamental theoretical ideas such as Bose-Einstein condensation (BEC) [19, 20], the Mott-Insulator transition in the Bose-Hubbard model [21] and the evolution from BCS to BEC superfluidity [22, 23, 24]. Strong connections to standard condensed matter physics have been developed, specially in the case of optical lattices, which are being used to simulate several properties of standard solids [4].

Building on the success of early experiments [25, 26] where bosonic atoms in two hyperfine states were trapped and investigated, a new class of experiments have emerged targeting the trapping of bosonic or fermionic atoms with large integer or half-integer spins, with many hyperfine states. Such experimental efforts have now lead to the realization SU(N) invariant Hamiltonians, as evidenced experimentally in the case of Strontium (Sr) atoms [27]. The realization of such exotic situations is promoting the field of ultra-cold atoms beyond the stage of simulating known Hamiltonians from diverse areas of physics to the stage of creating novel Hamiltonians, which may not have direct counterpart in any area of Physics. An important example, as previously discussed, is the unusual case of two-hyperfine-state bosons in the presence of artificial spin-orbit coupling, which was created experimentally [5, 28] and its effects on Bose-Einstein condensation were studied thoroughly [29, 30, 31, 32].

In this chapter, I discuss the case of three-hyperfine-state (or pseudo-spin 1)

fermions in the presence of artificial spin-orbit coupling, instead of the case of two-hyperfine-state (or pseudo-spin-1/2) fermions that has been recently studied theoretically [33, 34, 35, 36, 37] and experimentally [38, 39, 1, 40]. The case of two-hyperfine-state fermions with artificial SOC was discussed in chapter I in the context of non-interacting fermions and in chapters II and III in the context of the formation of Feshbach molecules between two free fermions and two harmonically trapped fermions, respectively.

A potential three-hyperfine state (pseudo-spin 1) Fermi system is the fermionic isotope of Potassium (^{40}K), which possesses several hyperfine states that can be trapped [15]. For instance, (^{40}K) was the system used to create artificial spin-orbit with two-hyperfine-state fermions [38, 1]. However, other high spin Fermi atoms are also potential candidates, such as Ytterbium (Yt) or Strontium (Sr), since they have several hyperfines that can also be trapped.

The situation envisioned here is that three hyperfine states of the Fermi atom are trapped, and these states are coupled via two-photon light-matter interactions, that is, Raman transitions. The laser beams that produce these Raman transitions generate artificial spin-orbit coupling in the fermionic system, in the same way as in the two-hyperfine state case discussed previously. Thus, the present case is similar to that encountered in Chapters II and III, but a basic difference is that one has three internal levels, rather than two, and they are all coupled via Raman transitions. A schematic diagram of the simplest non-trivial configuration is shown in Fig. 4.1. This change from two to three hyperfine states introduces qualitatively different terms in the Hamiltonian and generates new physics to be discussed in this chapter.

The interest in studying three-hyperfine-state fermions is driven in part by the planning of the next generation of experiments involving artificial spin-orbit coupling, and in part by theoretical questions related to the quantum phases of these systems and their connection to color and multi-band superconductors.

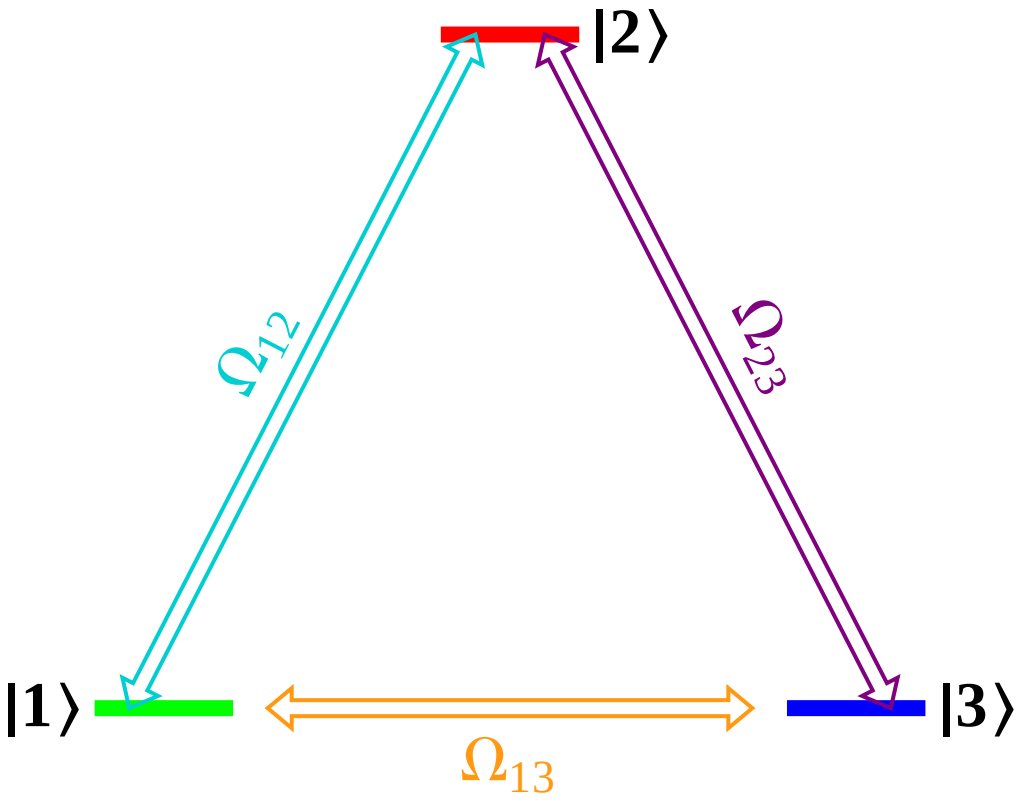

Figure 4.1: Schematic diagram of three hyperfine states interacting with Raman beans. The energy levels in the presence of the Raman beams are labeled as 1, 2, 3 and the Rabi frequencies reflecting the transition matrix element between the states are labeled Ω_{12}, Ω_{13}, Ω_{23}. In this simpler configuration the states 1 and 3 are initially degenerate, and state 2 can have either higher or lower energy with respect to states 1 and 2.

Even the non-interacting system of three-hyperfine-state fermions is interesting when artificial spin-orbit coupling and Zeeman fields are introduced, because they change the energy dispersions and strongly renormalize the effective mass of the fermions. Furthermore, a specially simple can be engineered, where states 1 and 3 experience recoil during the Raman process, but state 2 does not. This is the situation illustrated in Fig. 4.1, which leads to an effective Hamiltonian described by spin-one matrices. At the independent particle level the Hamiltonian is identical to that encountered in spin-one bosons, such as ^{87}Rb, where interesting spinor physics in the presence of spin-orbit coupling is now being studied [13]. However, even in

the case of non-interacting fermions with three hyperfine states, the physics is very different from that of non-interacting bosons. For pseudo-spin-1 fermions, the Pauli exclusion principle leads to three Fermi surfaces, whose shape and size are strongly affected by artificial spin-orbit and Zeeman fields. Furthermore, as we shall see later in this chapter, topological changes in Fermi surfaces (Lifshitz transitions) may occur as a function of the momentum transfer to the atoms.

The problem becomes even more interesting with the addition of interactions between the fermions. For instance, after three-hyperfine-state fermions in states 1, 2 and 3 are trapped, one can envision the tuning of the interactions between atoms in states 1 and 2, 2 and 3, as well as 1 and 3. That tuning may be possible using available Feshbach resonances, which are specific to each type of atom. However, it is difficult to tune all these interactions independently, because, most commonly, Feshbach resonances are reached via the application of an external magnetic field, which affects all internal states simultaneously. Nevertheless, it is relatively easy to find resonances, for example, between states 1 and 3 without other nearby resonances between states 1 and 2 or between states 2 and 3. So that the interactions between states 1 and 3 can be tuned, while keeping fermions in states 1 and 2, as well as 2 and 3 essentially non-interacting.

The study of three-hyperfine-state fermions with attractive interactions has some connections to color superconductivity, when the three different hyperfine states are viewed as colors (red for state 1, green for 2 and blue for 3) [41]. A perfect connection is difficult to make for several reasons, but let me outline just two. First, one would have to add bosonic atoms to the system, such that they could play the role gluons which binds different colored fermions. To simulate the gluon, the bosonic atom would need to have spin-1, and to mediate an indirect interaction between different three-hyperfine-states. The addition of a spin-1 boson makes experiments much more difficult, specially if one has in mind to add artificial spin-orbit coupling to the mix.

Second, even if one sidelines the addition of bosons to provide the glue between colored fermions, it is also experimentally difficult using Feshbach resonances to make the interactions g_{ij} between fermions in states i and j (with $i \neq j$) being all the same, that is, $g_{12} = g_{13} = g_{23}$. Even though, it may not be easy to simulate precisely color superconductivity as envisioned in a QCD environment, where different colored quarks bind into Cooper pairs mediated by gluons, one can expect a connection between the superfluid phases that three-hyperfine-state Fermi superfluids possess and color superconductivity, if interactions can be found to produce three sets of Cooper pairs involving a) states 1 and 2 (red and green), b) states 1 and 3 (red and blue), and c) states 2 and 3 (green and blue). This is the extent of the connection that one intends to make to color superconductivity: three different types of Cooper pairs in the superfluid state, without worrying about the origin/mechanism of pairing.

Three-hyperfine state (pseudo-spin-1) fermions are also related to multi-band superconductors, which are materials that have Cooper pairing occuring in more than one Fermi surface. This connection arises by thinking of the eigenstates of the three-hyperfine state Fermi system as labelling different energy bands. If interactions can be controlled to produce superfluidity, a multi-band superfluid should emerge in the presence of spin-orbit coupling and Zeeman fields. Several multi-band superconductors are known to exist in condensed matter physics, such as Magnesium-Diboride [42], Strontium Ruthenate [43] and a family of materials called Pcnitides [44].

It is important to emphasize that systems of three-hyperfine-state (pseudo-spin-1) Fermions are not in violation of the spin-statistics theorem [45], as the hyperfine states 1, 2 and 3 do not label true spin states, but rather internal states that represent pseudo-spin degrees of freedom. In the same sense, the labels *color* or *band index* may be used to represent either the internal states or the eigenstates of the Hamiltonian corresponding to non-interacting three-hyperfine-state fermions. Having this in mind,

I discuss several spectroscopic properties in section 4.2 for the case of many non-interacting fermions in the presence of artificial spin-orbit coupling Zeeman fields and quadratic Zeeman shifts. While, I set the stage for the study of the superfluid phases of three-hyperfine-state fermions in section 4.3 when atom-atom interactions are also included.

4.2 Non-interacting three-hyperfine-state fermions in the presence of artificial spin-orbit and Zeeman fields

In this section, I discuss the effective Hamiltonian for three-hyperfine-state fermions in the presence of artificial spin-orbit coupling and Zeeman fields. The effective Hamiltonian is obtained in the same way as for the case of two-hyperfine-state fermions, that is, via Raman processes. The essential difference is that now one could have three-hyperfine-states coupled via up to three Raman transitions from states 1 to 2, 2 to 3, and 1 to 3, instead of a single Raman transition connecting states 1 to 2 in the case of two-hyperfine-state fermions.

I will study the simplest non-trivial case of three-hyperfine state fermions where Raman processes couple states 1 to 2 and 2 to 3, such that only two Raman transitions are needed. The effective Hamiltonian describing this situation is obtained as follows. For the Raman transition from state 1 to 2, there is a net momentum transfer of $\mathbf{Q}_{12}$ from the photons to the atoms in state 1 and a net momentum transfer of $-\mathbf{Q}_{23}$ from the photons to the atoms in state 3, resulting in the light-atom Hamiltonian matrix

$$\mathbf{H}_{\mathrm{LA}}(\mathbf{k}) = \begin{pmatrix} \varepsilon_1(\mathbf{k}) & \Omega_{12} & 0 \\ \Omega_{12}^* & \varepsilon_2(\mathbf{k}) & \Omega_{23} \\ 0 & \Omega_{23}^* & \varepsilon_3(\mathbf{k}) \end{pmatrix}, \tag{4.1}$$

written in the rotating frame.

Each diagonal element (ℓ^{th} state) of the light-atom Hamiltonian matrix in Eq. (4.1) has momentum $\mathbf{k}-\mathbf{k}_\ell$, and energy dispersion $\varepsilon_\ell(\mathbf{k}) = (\mathbf{k}-\mathbf{k}_\ell)^2/(2m)+\eta_\ell$ corresponding

to the sum of the kinetic energy $(\mathbf{k}-\mathbf{k}_\ell)^2/(2m)$ of the ℓ^{th} hyperfine state after the net momentum transfer $\mathbf{k}_\ell$ and the *internal* energy η_ℓ. The transferred momenta $\mathbf{k}_\ell$ are explicitly $\mathbf{k}_1 = \mathbf{Q}_{12}$, $\mathbf{k}_2 = \mathbf{0}$ and $\mathbf{k}_3 = -\mathbf{Q}_{23}$. The terms $\Omega_{\ell m}$ are the Rabi frequencies describing the coupling of adjacent hyperfine states, which can be taken to be real such that $\Omega_{12} = \Omega_{12}^*$ and $\Omega_{23} = \Omega_{23}^*$. As in the case of two-hyperfine states, the Rabi frequencies are proportional to the intensity of the laser fields causing two-photon transitions between two atomic states. We can define an energy reference via the sum $\sum_\ell \eta_\ell = \eta$, in this case we can set $\eta_1 = -\delta$, $\eta_2 = \eta$ and $\eta_3 = +\delta$, where δ represents the detuning energy of the Raman transition.

When the beams for each Raman transition form an arbitrary angle, momentum transfers can be parametrized as $\mathbf{k}_1 = k_T\hat{\mathbf{x}}$, $\mathbf{k}_2 = \mathbf{0}$, and $\mathbf{k}_3 = -k_T\hat{\mathbf{x}}$, where k_T is the magnitude of the momentum transferred to the atom by the photons. The magnitude's range is $0 \leq k_T \leq 2k_R$, where $k_R = 2\pi/\lambda$ is the recoil momentum, and λ is the photon wavelength. Assuming that all Rabi frequencies are the same $(\Omega_{12} = \Omega_{23} = \Omega)$ the Hamiltonian of Eq. (4.1) reduces to

$$\mathbf{H}_{\mathrm{LA}}(\mathbf{k}) = \begin{pmatrix} \varepsilon_0(\mathbf{k}) - h_z(\mathbf{k}) + b_z & -h_x/\sqrt{2} & 0 \\ -h_x/\sqrt{2} & \varepsilon_0(\mathbf{k}) & -h_x/\sqrt{2} \\ 0 & -h_x/\sqrt{2} & \varepsilon_0(\mathbf{k}) + h_z(\mathbf{k}) + b_z \end{pmatrix}, \qquad (4.2)$$

where $\varepsilon_0(\mathbf{k}) = \mathbf{k}^2/(2m) + \eta$ is a reference kinetic energy which is the same for all hyperfine states, $h_z(\mathbf{k}) = 2k_Tk_x/(2m) + \delta$ is a momentum dependent Zeeman field along the z-axis, which is transverse to the momentum transfer direction (x-axis), $h_x(\mathbf{k}) = -\sqrt{2}\Omega$ is the *spin-flip* (Rabi) field, and $b_z = k_T^2/(2m) - \eta$ is the quadratic Zeeman term.

It is important to mention that very recently, a similar Hamiltonian was created experimentally in the NIST group for spin-one bosonic atoms [13], where two Raman transitions were also used to couple three hyperfine states of ^{87}Rb. This recent

experimental report gives further justification to the theoretical work involving three-hyperfine state fermions discussed in this chapter, as this is a natural next direction of this rapidly evolving field.

The light-atom Hamiltonian matrix displayed in Eq. (4.2.2) can be expanded in terms of a subset of the SU(3) Gell-Mann matrices that includes the identity $\mathbf{1}$ and the spin-one angular momentum matrices $\mathbf{J}_x$, $\mathbf{J}_z$ and $\mathbf{J}_z^2$. In compact notation, the expansion reads

$$\mathbf{H}_{\mathrm{LA}}(\mathbf{k}) = \varepsilon_0(\mathbf{k})\mathbf{1} - h_x(\mathbf{k})\mathbf{J}_x - h_z(\mathbf{k})\mathbf{J}_z + b_z\mathbf{J}_z^2. \tag{4.3}$$

Written in this form the light-atom Hamiltonian matrix can be interpreted as describing pseudo-spin-one fermions in the presence of momentum dependent Zeeman field components $h_x(\mathbf{k})$, $h_z(\mathbf{k})$ and a quadratic Zeeman shift parametrized by the coefficient b_z.

4.2.1 Energy Spectrum

The next step in the analysis of the light-atom Hamiltonian matrix described in Eq. (4.3) is to obtain its energy spectrum. The simplest situation encountered corresponds to the vanishing of the quadratic Zeeman term, that is, to $b_z = 0$. When this happens, the light-atom Hamiltonian matrix $\mathbf{H}_{LA}(\mathbf{k})$ reduces to that of pseudo-spin-one fermions in the presence of a momentum-dependent Zeeman field with components $h_x(\mathbf{k})$ and $h_z(\mathbf{k})$. In this case, the eigenvalues are

$$E_\alpha(\mathbf{k}) = \varepsilon_0(\mathbf{k}) - m_\alpha|h_{\mathrm{eff}}(\mathbf{k})|, \tag{4.4}$$

with $m_\alpha = \{+1, 0, -1\}$, where the effective momentum dependent Zeeman field amplitude is $|h_{\mathrm{eff}}(\mathbf{k})| = \sqrt{|h_x(\mathbf{k})|^2 + |h_z(\mathbf{k})|^2}$.

The general solution for the eigenvalues of Eq. (4.3) can be obtained using Cardano's method [46], even for $b_z \neq 0$. The eigenvalues of this pseudo-spin-one fermion

Hamiltonian can be obtained analytically from the zeros of the characteristic polynomial $P(\omega) = \det\left[\omega\mathbf{1} - \mathbf{H}_{\rm LA}(\mathbf{k})\right]$, which leads to the cubic equation:

$$\omega^3 - \omega^2 \mathrm{Tr}\left[\mathbf{H}_{LA}(\mathbf{k})\right] - \frac{\omega}{2}\left\{\mathrm{Tr}\left[\mathbf{H}_{LA}(\mathbf{k})\right]^2 - \left[\mathrm{Tr}\left[\mathbf{H}_{LA}(\mathbf{k})\right]\right]^2\right\} - \det \mathbf{H}_{LA}(\mathbf{k}) = 0 \quad (4.5)$$

but the general expressions are quite cumbersome and not particularly illuminating. Thus, we also obtain the eigenvalues $E_\alpha(\mathbf{k})$ by direct diagonalization of $\mathbf{H}_{\rm LA}(\mathbf{k})$ to validate the analytical results and order them such that $E_1(\mathbf{k}) > E_2(\mathbf{k}) > E_3(\mathbf{k})$.

From this point on, I will consider only the case where the detuning δ is set to zero, which corresponds to the simplest experimental situation. However, I will keep nonzero all the other experimentally tunable parameters k_T, Ω, and b_z (or η) appearing in the light-matter Hamiltonian matrix $\mathbf{H}_{LA}(\mathbf{k})$ of Eq. (4.3).

In Fig. 4.2, plots of eigenvalues $E_\alpha(\mathbf{k})$ versus momentum along the k_x and k_y directions are shown. Qualitatively different situations are illustrated in this figure, corresponding to momentum transfer $k_T = 0.5k_R$, Rabi frequency $\Omega = 0.35E_R$ and three different values of the quadratic Zeeman shift $b_z = \{-E_R, 0, E_R\}$. Along the k_x direction, notice that a double minimum is present in $E_3(\mathbf{k})$ when $b_z < 0$, and that a double minimum appears in $E_2(\mathbf{k})$, when $b_z > 0$, while $E_3(\mathbf{k})$ is very flat near $k_x = 0$ and $E_2(\mathbf{k})$ has a single minimum when $b_z = 0$.

If our system consisted of non-interacting spin-one bosonic atoms, a phase transition would take place at low temperatures between a Bose-Einstein condensate (BEC) at finite and zero momentum as b_z is increased from negative to positive values (see Fig. 4.2). However, for three-hyperfine state fermions the Pauli exclusion principle is important, and thus available energy states are filled up to the Fermi energy corresponding to the appropriate density of particles. This leads to the emergence of Fermi surfaces, to be discussed next.

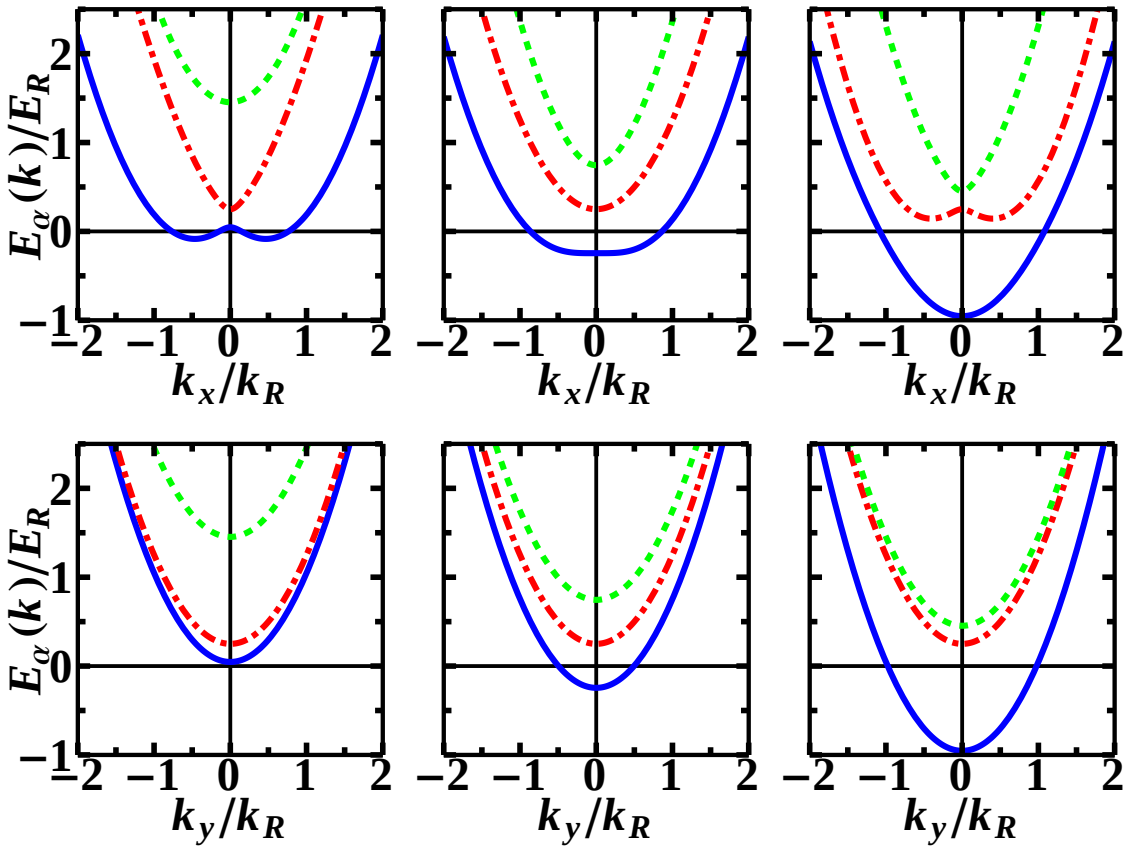

Figure 4.2: (color online) Eigenvalues $E_\alpha(\mathbf{k})$ in qualitatively different situations corresponding to momentum transfer $k_T = 0.5k_R$, Rabi frequency $\Omega = 0.35E_R$ and quadratic Zeeman shift $b_z = -E_R$ (left); $b_z = 0$ (middle); $b_z = E_R$ (right). The dashed-green line corresponds to $E_1(\mathbf{k})$, the dot-dashed-red line to $E_2(\mathbf{k})$, and the solid blue to $E_3(\mathbf{k})$. The top and bottom panels corresponds to cuts along the $(k_x, 0, 0)$ and $(0, k_y, 0)$ directions, respectively.

4.2.2 Fermi Surfaces

For three-hyperfine-state fermions, light-matter interactions produce three energy bands with dispersions and corresponding Fermi surfaces that can be dramatically modified by the tuning of the experimental parameters k_T, Ω and b_z.

In Fig. 4.3, the Fermi surfaces in qualitatively different situations corresponding to $k_T = 0.5k_R$, $\Omega = 0.35E_R$ and $b_z = \{-E_R, 0, E_R\}$ are shown. I define the effective Fermi momentum k_F via the total particle density $n = 3k_F^3/(6\pi^2)$, where the factor of 3 indicates the presence of three internal states which lead to the three bands of

the many-fermion system. I also define the effective Fermi energy as $E_F = k_F^2/(2m)$ and and remark that the Fermi surfaces shown in Fig. 4.3 correspond to a density of $n = 10^{14}\text{atoms/cm}^3$.

Notice that in the middle panel of Fig. 4.3 there is no quadratic Zeeman shift ($b_z = 0$), but k_T and Ω are non-zero. As described above, this implies that new fermionic bands $E_\alpha(\mathbf{k}) = \varepsilon_0(\mathbf{k}) - m_\alpha|h_{\text{eff}}(\mathbf{k})|$, with $m_\alpha = \{+1, 0, -1\}$, emerge from three degenerate bands $\varepsilon_0(\mathbf{k})$. As a result, identical spherical Fermi surfaces associated with $\varepsilon_0(\mathbf{k})$ become non-degenerate since the new energy dispersions are controlled by $|h_{\text{eff}}(\mathbf{k})|$, which is a function of k_T and Ω. With the exception of the central band $E_2(\mathbf{k})$, which still produces a spherical Fermi surface, the other two bands possess anisotropic Fermi surfaces due to $|h_{\text{eff}}(\mathbf{k})|$.

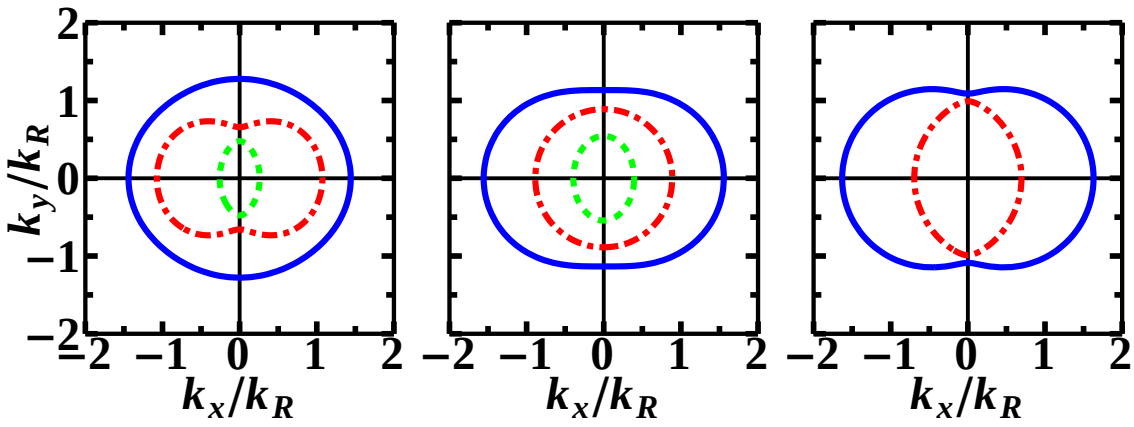

Figure 4.3: (color online) Fermi surfaces are shown in qualitatively different situations corresponding to momentum transfer $k_T = 0.5k_R$, Rabi frequency $\Omega = 0.35E_R$ and three different values of the quadratic Zeeman shift $b_z = -E_R$ (left); (b) $b_z = 0$ (middle); (c) $b_z = E_R$ (right). The values of the chemical potential are $\mu = 1.23E_R$ (left), $\mu = 1.04E_R$ (middle), $\mu = 0.68E_R$ (right) for particle density $n = 10^{14}\text{atoms/cm}^3$.

These effects are reminiscent of the Pomeranchuk [47] instability in condensed matter physics, where deformations in Fermi surfaces may emerge spontaneously in systems with anisotropic density-density interactions, without violating Luttinger's

theorem [48]. However, in the present case, it is important to emphasize that deformations of the spherical Fermi surfaces associated with $\epsilon_0(\mathbf{k})$ are induced by the artifical spin-orbit coupling, and therefore are not due to spontaneous symmetry breaking.

Nevertheless a connection can be made to the situation encountered in condensed matter physics, where anisotropic interactions produce deformations of the Fermi surfaces, making them incompatible with the underlying symmetry of the crystal. The easiest way to see this connection is to analyze the toy Hamiltonian

$$H = \sum_{\mathbf{k},\alpha} [\varepsilon(\mathbf{k})\hat{n}_\alpha(\mathbf{k})] + \frac{1}{2}\sum_{\mathbf{k},\mathbf{k}'\alpha\beta} F_{\alpha\beta}(\mathbf{k},\mathbf{k}')\hat{n}_\alpha(\mathbf{k})\hat{n}_\beta(\mathbf{k}')$$

where $\hat{n}_\alpha(\mathbf{k}) = c_\alpha^\dagger(\mathbf{k})c_\alpha(\mathbf{k})$ is the number operator for spin α. The replacement of $\hat{n}_\alpha(\mathbf{k}) = \langle\hat{n}_\alpha(\mathbf{k})\rangle + \delta\hat{n}_\alpha(\mathbf{k})$ leads to the mean-field Hamiltonian

$$H = \sum_{\mathbf{k},\alpha} [E_\alpha(\mathbf{k})\hat{n}_\alpha(\mathbf{k})] + C. \tag{4.6}$$

The energy for internal state α is $E_\alpha(\mathbf{k}) = \varepsilon(\mathbf{k}) - h_\alpha(\mathbf{k})$, where $\varepsilon(\mathbf{k}) = \mathbf{k}^2/(2m)$, is the kinetic energy of fermions of mass m, and

$$h_\alpha(\mathbf{k}) = -\sum_{\beta,\mathbf{k}'} [F_{\alpha\beta}(\mathbf{k},\mathbf{k}') + F_{\beta\alpha}(\mathbf{k}',\mathbf{k})]\,\langle\hat{n}_\beta(\mathbf{k}')\rangle, \tag{4.7}$$

is the *effective* field affecting the α-band. Lastly, the constant energy reference is

$$C = \frac{1}{2}\sum_{\mathbf{k},\mathbf{k}'\alpha\beta} F_{\alpha\beta}(\mathbf{k},\mathbf{k}')\langle\hat{n}_\alpha(\mathbf{k})\rangle\langle\hat{n}_\beta(\mathbf{k}')\rangle. \tag{4.8}$$

Notice that when $h_\alpha(\mathbf{k})$ does not have spherical symmetry, then the Fermi surface for state α is deformed. The eigenvalues of the mean field Hamiltonian displayed in Eq. (4.6) have the same structure of eigenvalues at the Hamiltonian matrix describing the spin-orbit coupled systems of three-hyperfine-state fermions.

In Fig. 4.3, a clear signature of the Pomeranchuk-like deformation can be seen for the band with energy $E_2(\mathbf{k})$ shown as the red dot-dashed line. However, notice that for fixed k_T and Ω, what drives the Fermi surface deformations is the quadratic Zeeman

coupling b_z, that is, the J_z-J_z spinor coupling instead of density-density interactions. When $b_z = 0$, the Fermi surface corresponding to $E_2(\mathbf{k})$ is spherically symmetric, however when $b_z > 0$ ($b_z < 0$) this Fermi surface suffers a predominant deformation along the k_x (k_y) direction. The Ising-Nematic deformation parameter

$$\mathcal{N}_2 = \int d\mathbf{k} \left[k_y^2 + k_z^2 - 2k_x^2\right] \langle \phi_2^\dagger(\mathbf{k})\phi_2(\mathbf{k})\rangle \tag{4.9}$$

becomes zero for $b_z = 0$, positive for $b_z < 0$ and negative for $b_z > 0$, where $\phi_2^\dagger(\mathbf{k})$ is the creation operator for eingestate 2. Similar Pomeranchuk-type deformations occur for $E_1(\mathbf{k})$ or $E_3(\mathbf{k})$, however deformations are already present even for $b_z = 0$, because the spin-orbit coupling contains non-spherically-symmetric contributions through the effective field $h_{\text{eff}}(\mathbf{k})$.

It is also important to notice the existence of a Lifshitz transition [49], which for fixed momentum transfer $\mathbf{k}_T$ and particle density n, can be tuned via the Rabi frequency Ω and the quadratic Zeeman coupling b_z. In Fig. 4.3, one can see a Lifsthitz transition for fixed Ω and changing b_z, as three Fermi surfaces (genus 3) for $b_z = 0$ are reduced to two Fermi surfaces (genus 2) for $b_z = -E_R$. A phase diagram can be constructed mapping out these topological changes in the Ω versus b_z plane. In Fig. 4.4, I show the behavior of the chemical potential μ in units of E_R versus the quadratic Zeeman shift parameter b_z/E_R for fixed values of the momentum transfer k_T. It is this change of μ as a function of b_z that is responsible for the Lifshitz transition in the Fermi surfaces of the system, eventhough the particle density is fixed.

Having analysed the eigenvalues and the Fermi surfaces of three-hyperfine state fermions, I will discuss next the eigenfunctions of the system and the unitary matrix transformation that diagonalizes the Hamiltonian matrix $\mathbf{H}_{LA}(\mathbf{k})$.

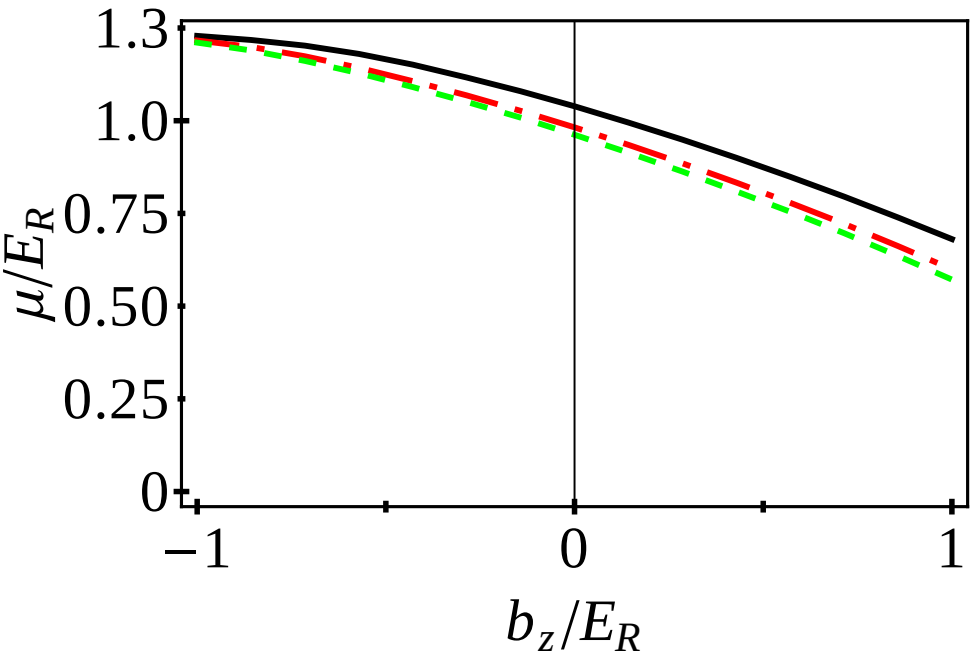

Figure 4.4: Chemical potential versus b_z/E_R is shown for $\Omega = 0.35E_R$ with $k_T = 0k_R$ (black solid), $k_T = 0.25k_R$ (red dot-dashed), $k_T = 0.5k_R$ (green dashed), for particle density $n = 10^{14}$atoms/cm^3.

4.2.3 Eigenfunctions of three-component Fermions

The effects of artificial spin-orbit and quadratic Zeeman coupling, due to light-atom interactions via the Raman scheme, can be further explored by investigating the three-component spinor wavefunctions of the Hamiltonian

$$H_{\mathrm{LA}} = \sum_{\mathbf{k}} \mathbf{\Psi}_{\mathbf{k}}^{\dagger} \mathbf{H}_{\mathrm{LA}}(\mathbf{k}) \mathbf{\Psi}_{\mathbf{k}}, \tag{4.10}$$

where $\mathbf{\Psi}_{\mathbf{k}}$ is a three-component spinor with $\mathbf{\Psi}_{\mathbf{k}}^{\dagger} = \left(\psi_1^{\dagger}(\mathbf{k}), \psi_2^{\dagger}(\mathbf{k}), \psi_3^{\dagger}(\mathbf{k})\right)$, where $\psi_s^{\dagger}(\mathbf{k})$ represents the creation of a fermion in hyperfine state s. When $s = 1$, the atom has momentum $\mathbf{k} - \mathbf{k}_T$ and $m_1 = +1$; when $s = 2$, the atom has momentum $\mathbf{k}$ and $m_2 = 0$; and when $s = 3$, the atom has momentum $\mathbf{k} + \mathbf{k}_T$ and $m_3 = -1$. The Hamiltonian H_{LA} can be diagonalized via the rotation $\mathbf{\Phi}(\mathbf{k}) = \mathbf{U}(\mathbf{k})\mathbf{\Psi}(\mathbf{k})$, which connects the three-component spinor $\mathbf{\Psi}(\mathbf{k})$ in the original spin basis to the three-component spinor $\mathbf{\Phi}(\mathbf{k})$ representing the basis of eigenstates. The matrix $\mathbf{U}(\mathbf{k})$ is

unitary and satisfies the relation $\mathbf{U}^\dagger(\mathbf{k})\mathbf{U}(\mathbf{k}) = \mathbf{1}$. The diagonalized Hamiltonian is

$$\mathbf{H}_D(\mathbf{k}) = \mathbf{U}(\mathbf{k})\mathbf{H}_{\rm LA}\mathbf{U}^\dagger(\mathbf{k}) \tag{4.11}$$

with matrix elements $[\mathbf{H}_D(\mathbf{k})]_{\alpha\beta} = E_\alpha(\mathbf{k})\delta_{\alpha\beta}$, where $E_\alpha(\mathbf{k})$ are the eigenvalues of $\mathbf{H}_{\rm LA}(\mathbf{k})$ discussed above. The three-component spinor in the eigenbasis is $\mathbf{\Phi}^\dagger(\mathbf{k}) = \left(\phi_1^\dagger(\mathbf{k}), \phi_2^\dagger(\mathbf{k}), \phi_3^\dagger(\mathbf{k}), \right)$, where $\phi_\alpha^\dagger(\mathbf{k})$ is the creation operator of a fermion with eigenenergy $E_\alpha(\mathbf{k})$. The unitary matrix

$$\mathbf{U}(\mathbf{k}) = \begin{pmatrix} u_{11}(\mathbf{k}) & u_{12}(\mathbf{k}) & u_{13}(\mathbf{k}) \\ u_{21}(\mathbf{k}) & u_{22}(\mathbf{k}) & u_{23}(\mathbf{k}) \\ u_{31}(\mathbf{k}) & u_{32}(\mathbf{k}) & u_{33}(\mathbf{k}) \end{pmatrix} \tag{4.12}$$

has rows that satisfy the normalization condition $\sum_s |u_{\alpha s}(\mathbf{k})|^2 = 1$. The knowledge of the unitary matrix elements $u_{\alpha s}$ allows for an analysis of the spin-dependent momentum distribution of three-component Fermi gas to be discussed next.

4.2.4 Momentum Distribution

Using a Stern-Gerlach technique, another spectroscopic property that can be measured is the spin-dependent momentum distribution

$$n_s(\mathbf{k}) = \sum_\alpha |u_{\alpha s}(\mathbf{k})|^2 f[E_\alpha(\mathbf{k})]. \tag{4.13}$$

We can fix the average number of particles $N_s = \sum_{\mathbf{k}} n_s(\mathbf{k})$ in each state s independently, in which case chemical potentials μ_s for each state s are necessary. However, when the total average number of particles $N = \sum_s N_s = \sum_{s,\alpha} |u_{\alpha s}(\mathbf{k})|^2 f[E_\alpha(\mathbf{k})]$ is fixed, we need only one chemical potential μ. The use of the normalization condition $\sum_s |u_{\alpha s}(\mathbf{k})|^2 = 1$ leads to $N = \sum_\alpha f[E_\alpha(\mathbf{k})]$.

In Fig. 4.5, we show $n_s(\mathbf{k})$ at low temperatures for the simpler case where there is only one chemical potential. The cross sections along k_x with $k_y = k_z = 0$ are shown in Fig. 4.5 top panels, while the cross sections along k_y with $k_x = k_z = 0$ are shown

in Fig. 4.5 lower panels. In the top panels of Fig. 4.5, notice that $n_s(\mathbf{k})$ for states $s = 1$ ($m_1 = +1$) and $s = 3$ ($m_3 = -1$) do not have well defined parity, but are mirror images of each other. This is a reflection of the Hamiltonian invariance under the transformation $(k_x, m_1) \to (-k_x, m_3)$ and $(k_x, m_3) \to (-k_x, m_1)$.

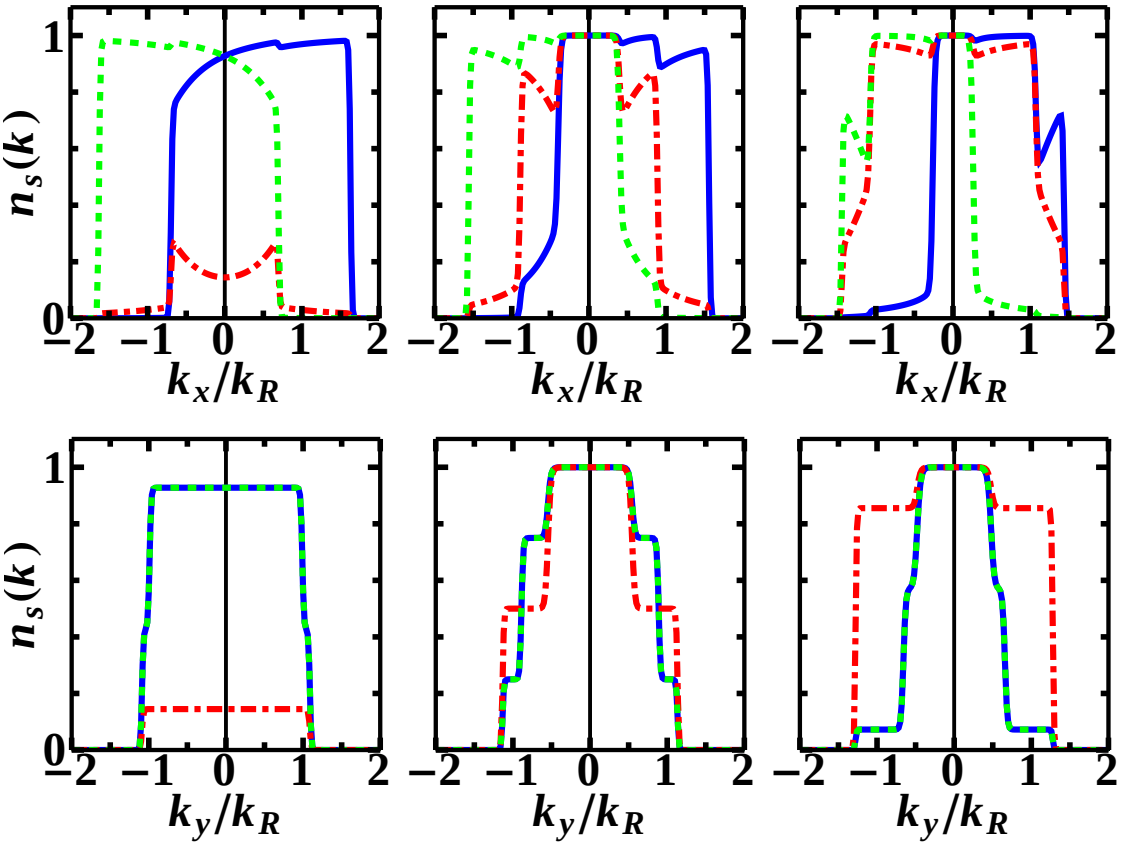

Figure 4.5: Momentum distributions $n_s(\mathbf{k})$ for $s = 1$ ($m_1 = +1$) (blue-solid curves), $s = 2$ ($m_2 = 0$) (red-dot-dashed curves) and $s = 3$ ($m_3 = -1$) (green-dashed curves), with $T = 0.02E_R \approx 0.01E_F$. The parameter values are $b_z = -E_R$ (left panels), $b_z = 0$ (middle panels) and $b_z = +E_R$ (right panels), with $k_T = 0.5k_R$ and $\Omega = 0.35E_R$.

The momentum distributions shown in Figure 4.5 and Figure 4.6 can be understood as follows. The momentum transfer along the k_x direction shifts the center of mass of the atom in state $s = 1$ with $m_1 = +1$ ($s = 3$ with $m_3 = -1$) to be around k_T ($-k_T$). While there is no momentum shift for the state $s = 2$ with $m_2 = 0$. In the limit of $\Omega \to 0$, $n_s(\mathbf{k})$ along k_x have square shapes characteristic of degenerate fermions for each state labeled by s. However, momentum transfer can only occur when the

lasers are on, which means $\Omega \neq 0$. This leads to mixing of states with different values of s and to a modification of the trivial momentum distributions via the coherence factors $|u_{\alpha s}(\mathbf{k})|^2$. The dramatic effects of the coherence factors is seen on Fig. 4.5 (top panels) where finite Ω causes strong deviations from square momentum distributions, due to the momentum-dependent mixing states with different values of s. However, $n_s(\mathbf{k})$ along the k_y direction experience no momentum transfer and the distributions are centered around $k_y = 0$. For $k_x = 0$, the light-atom Hamiltonian matrix is invariant under the transformations $(k_y, m_s) \to (-k_y, m_s)$, $(k_y, m_1) \to (-k_y, m_3)$, and $(k_y, m_3) \to (-k_y, m_1)$, such that the corresponding $n_s(\mathbf{k})$ along k_y for states $s = 1$ and $s = 3$ are identical. The square like structures that emerge are a consequence of the less dramatic dependence of the coherence factors $|u_{\alpha s}(\mathbf{k})|^2$ on k_y. By symmetry, the same square structures also appear along the k_z direction.

Notice that as b_z increases from negative to positive (left to right panels in Fig. 4.5), $n_s(\mathbf{k})$ for state $s = 2$ along the k_x and k_y directions increase on average at fixed Ω. This enhancement occurs because the energy of the $s = 2$ state becomes increasingly lowered in comparison to the energy of the $s = 1, 3$ states, and spectral weight is transferred from states $s = 1, 3$ to $s = 2$, causing a corresponding decrease in the average $n_s(\mathbf{k})$ of the former states. When b_z becomes large and negative, the central state ($s = 2$) is pushed up in energy with respect to $s = 1, 3$, thus the system reduces to effective spin-1/2 fermions for densities such that the Fermi energy crosses only the two lowest states. However, when b_z becomes large and positive, the central state ($s = 2$) is pushed down in energy with respect to the $s = 1, 3$ states, and for densities such that the Fermi energy only crosses the $s = 2$ state, the system reduces to effective spin-zero (spinless) fermions.

The matrix elements $u_{\alpha s}$ of the unitary matrix $\mathbf{U}(\mathbf{k})$ can also be used to analyse the spin-dependent density of states to be discussed next.

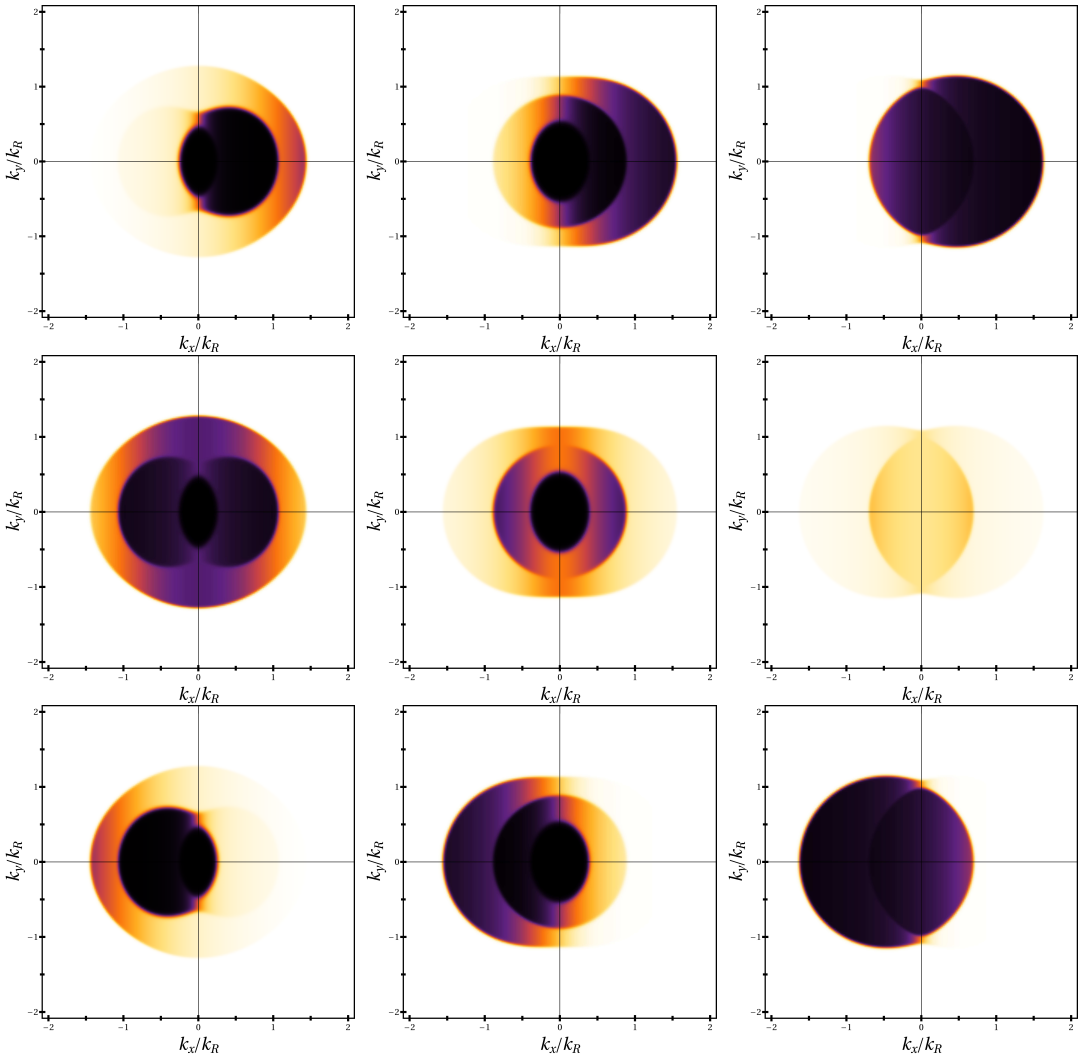

Figure 4.6: Contour momentum distribution of $s = 1$ (Top), $s = 2$ (Middle) and $s = 3$ (Bottom), states with $\Omega = 0.35E_R$ and $k_T = 0.5k_R$ with $b_z = E_R$ (left), $b_z = 0E_R$ (middle), $b_z = -E_R$ (right).

4.2.5 Density of States

The last spectroscopic quantity that I would like to analyze is the spin-dependent density of states (DOS)

$$\rho_s(\omega) = \sum_{\mathbf{k},\alpha} |u_{\alpha s}(\mathbf{k})|^2 \delta(\omega - E_\alpha(\mathbf{k})). \tag{4.14}$$

Below the minimum of $E_3(\mathbf{k})$ there are no states available, that is, $\rho_s(\omega) = 0$ for $\omega \leq \omega_*(\Omega, b_z, k_T) = \min_{\mathbf{k}} E_3(\mathbf{k})$. The spin-dependent DOS for $\Omega = 0.35E_R$ and $b_z = \{-E_R, 0, E_R\}$ are shown in Fig. 4.7. Notice that for $b_z = -E_R$ (left panel) the

spin-dependent DOS is non-zero only when $\omega \geq -0.09E_R$ and that for small values of $\gamma = (\omega - \omega_*)/E_R$, the main contributions to the total DOS $\rho(\omega) = \sum_s \rho_s(\omega)$ come from states $s = 1, 3$. In addition, for $b_z = 0$ (central panel), $\rho_s(\omega) \geq 0$ when $\omega \geq -0.27E_R$, and the DOS for each spin component are comparable for small values of γ. However, for $b_z = +E_R$ (right panel), $\rho_s(\omega) \geq 0$ when $\omega \geq -1.00E_R$, and the main contribution to $\rho(\omega)$ comes from $\rho_2(\omega)$ for small values of γ, as state $s = 2$ has the lowest energy.

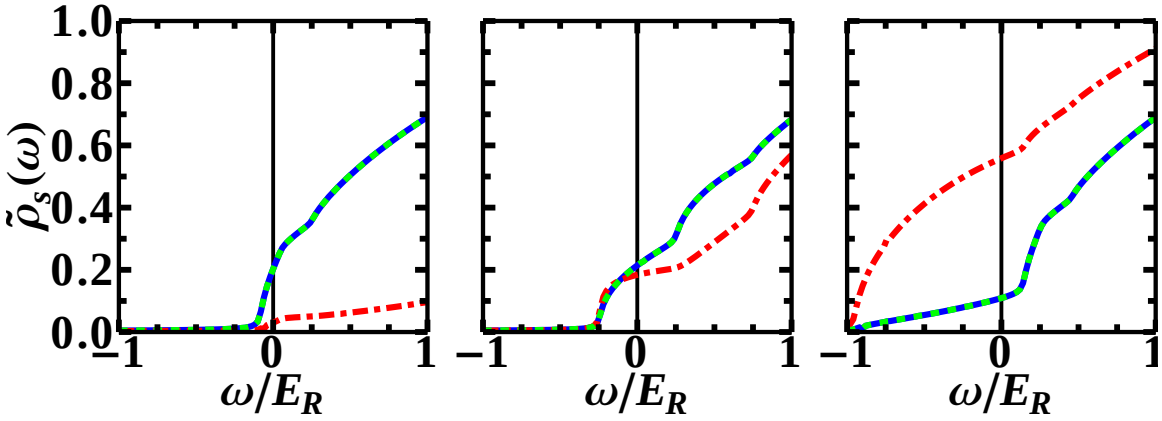

Figure 4.7: Density of states $\widetilde{\rho}_s(\omega) = \rho_s(\omega)E_F/N$ for $s = 1$ ($m_1 = +1$) (blue-solid lines), $s = 2$ ($m_2 = 0$) (red-dot-dashed lines), and $s = 3$ ($m_3 = -1$) (green-dashed lines). N is the total number of particles and E_F is the effective Fermi energy. We use a line-width broadening $\delta_{\ell w} = 0.01E_R$. The parameters used are $b_z = -E_R$ (left panel), $b_z = 0$ (middle panel) and $b_z = +E_R$ (right panel), with $k_T = 0.5k_R$ and $\Omega = 0.35E_R$ and $E_F = 1.95E_R$.

Having considered the case of non-interacting fermions in the presence of artificial spin-orbit coupling and Zeemsn fields in the preceeding sections, I am ready to discuss next a few preliminary aspects due to attractive interactions that can lead to superfluid phases.

4.3 Superfluid phases

In this section, I will discuss on a preliminary basis the effects of atom-atom interactions in systems of three-hyperfine-state fermions. I will consider the simplest theoretical situation that could be, in principle, realized in the fermionic isotope of

Potassium (^{40}K). I will discuss the case of s-wave attractive contact interactions between hyperfine $s = 1$ and $s = 3$ with strength g_{13}, between states $s = 1$ and $s = 2$ with strength g_{12} and between states $s = 2$ and $s = 3$ with strength g_{23}. This means that the interaction Hamiltonian can be written in momentum space as

$$H_{AA} = -V \sum_{\mathbf{k},\mathbf{k}',\mathbf{Q},s\neq s'} g_{ss'}\psi_s^\dagger(\mathbf{k}+\mathbf{Q}/2)\psi_{s'}^\dagger(-\mathbf{k}-\mathbf{Q}/\mathbf{2})\psi_{s'}(-\mathbf{k}'-\mathbf{Q}/\mathbf{2})\psi_s(\mathbf{k}'+\mathbf{Q}/2), \tag{4.15}$$

where $g_{ss'}$ represent the strength of s-wave contact interactions between hyperfine states s and s', V is the volume, $\mathbf{k}$ and $\mathbf{k}'$ are fermionic labels of momentum states and $\mathbf{Q}$ is the center of mass momentum of the fermion pair operator

$$b_{ss'}^\dagger(\mathbf{Q}) = \sum_{\mathbf{k}} \psi_s^\dagger(\mathbf{k}+\mathbf{Q}/2)\psi_{s'}^\dagger(-\mathbf{k}-\mathbf{Q}/\mathbf{2}). \tag{4.16}$$

The fermionic operators $\psi_s(\mathbf{q})$ describe exactly the same states that appear in the light-atom Hamitonian H_{LA} shown in Eq. (4.10). Finally, the atom-atom interaction Hamiltonian in terms of the pair operators become simply

$$H_{AA} = -V \sum_{\mathbf{Q}s\neq s'} g_{ss'} b_{ss'}^\dagger(\mathbf{Q}) b_{ss'}(\mathbf{Q}), \tag{4.17}$$

and the total Hamiltonian describing the effects of spin-orbit coupling, Zeeman fields, and atom-atom interactions is described by the sum

$$H_T = H_{LA} - \mu\hat{N} + H_{AA}, \tag{4.18}$$

where H_{LA} is the light-atom interaction Hamiltonian, $-\mu\hat{N}$ is the chemical potential term containing the number operator $\hat{N} = \sum_{\mathbf{k},s} \psi_s^\dagger(\mathbf{k})\psi_s(\mathbf{k})$ and the chemical potential μ, while H_{AA} is the atom-atom interaction Hamiltonian. The chemical potential term was added now because it will be necessary to fix the total number of particles later, as the superfluid phase will be described within the Grand Canonical ensemble in the same spirit of the conventional BCS theory.

Now that the Hamiltonian of our system is known, I will describe a few approximations that facilitate the search of superfluid phases of three-hyperfine state fermions

in the presence of spin-orbit coupling and Zeeman fields. The mean-field approach to three-hyperfine state superfluidity will be discussed next.

4.3.1 Mean Field Approach

The mean field approximation for the superfluid phase can be made by considering pairing at zero center of mass momentum only, that is, $\mathbf{Q} = \mathbf{0}$. This amounts physically to replacing the pairing operator $b_{ss'}(\mathbf{0})$ by it quantum mechanical and thermal average $\langle b_{ss'}(\mathbf{0})\rangle$. However, it is more convenient to define an order parameter for superfluidity via the relation

$$\Delta_{ss'} = -\frac{g_{ss'}}{V}\langle b_{ss'}(\mathbf{0})\rangle, \tag{4.19}$$

which is the quantity that appears naturally in the mean field Hamiltonian to be discussed shortly. The symbol V represents the volume of the system, such that the order parameter defined above represents an energy scale associated with the momentum sum of the paired fermionic states $\psi_s(\mathbf{k})$ and $\psi_{s'}(-\mathbf{k})$ with opposite momenta as described mathematically by the expression

$$\Delta_{ss'} = -\frac{g_{ss'}}{V}\sum_{\mathbf{k}}\langle\psi_{s'}(-\mathbf{k})\psi_s(\mathbf{k})\rangle. \tag{4.20}$$

The atom-atom interaction term H_{AA} can now be written in terms of the order parameter as

$$H_{AA}^{\mathrm{mf}} = -V\sum_{s\neq s'}\frac{|\Delta_{ss'}|^2}{g_{ss'}} + \sum_{\mathbf{k},s\neq s'}\left[\Delta_{ss'}\psi_s^\dagger(\mathbf{k})\psi_{s'}^\dagger(-\mathbf{k}) + H.C.\right], \tag{4.21}$$

where $H.C.$ denotes Hermitian conjugation. To write the total mean field Hamiltonian $H_T^{\mathrm{mf}} = H_{LA} + H_{AA}^{\mathrm{mf}}$ in standard form, it is convenient to introduce a generalized Nambu spinor (GNS)

$$\widetilde{\mathbf{\Psi}}^\dagger(\mathbf{k}) = \left(\psi_1^\dagger(\mathbf{k}), \psi_2^\dagger(\mathbf{k}), \psi_3^\dagger(\mathbf{k}), \psi_1(-\mathbf{k})\psi_2(-\mathbf{k}), \psi_3(-\mathbf{k})\right), \tag{4.22}$$

where the *widetilde* symbol is used to differentiate the GNS from the three-hyperfine state spinor $\mathbf{\Psi}^\dagger(\mathbf{k}) = \left(\psi_1^\dagger(\mathbf{k}), \psi_2^\dagger(\mathbf{k}), \psi_3^\dagger(\mathbf{k})\right)$ defined previously. The GNS can then be written in the compact form $\widetilde{\mathbf{\Psi}}^\dagger(\mathbf{k}) = \left(\mathbf{\Psi}^\dagger(\mathbf{k}), \mathbf{\Psi}^\dagger(-\mathbf{k})\right)$.

In the GNS basis the mean field Hamiltonian can be written in the simple form

$$H_T^{\mathrm{mf}} = \frac{1}{2}\sum_{\mathbf{k}} \widetilde{\Psi}^\dagger(\mathbf{k})\mathbf{H}_T^{\mathrm{mf}}(\mathbf{k})\widetilde{\Psi}(\mathbf{k}) + \frac{1}{2}\sum_{\mathbf{k},s}\xi_s(-\mathbf{k}) - \sum_{s\neq s'}\frac{|\Delta_{ss'}|^2}{g_{ss'}}, \tag{4.23}$$

where $\xi_s(\mathbf{k}) = \epsilon_s(\mathbf{k}) - \mu$ represent the kinetic energy term, where $\epsilon_s(\mathbf{k})$ is the energy dispersion of hyperfine state s. The mean field Hamiltonian matrix is

$$\mathbf{H}_T^{\mathrm{mf}}(\mathbf{k}) = \left(\begin{array}{c|ccc|ccc} & \psi_1(\mathbf{k}) & \psi_2(\mathbf{k}) & \psi_3(\mathbf{k}) & \psi_1^\dagger(-\mathbf{k}) & \psi_2^\dagger(-\mathbf{k}) & \psi_3^\dagger(-\mathbf{k}) \\ \hline \psi_1^\dagger(\mathbf{k}) & \xi_1(\mathbf{k}) & \Omega & 0 & 0 & \Delta_{12} & \Delta_{13} \\ \psi_2^\dagger(\mathbf{k}) & \Omega & \xi_2(\mathbf{k}) & \Omega & -\Delta_{12} & 0 & \Delta_{23} \\ \psi_3^\dagger(\mathbf{k}) & 0 & \Omega & \xi_3(\mathbf{k}) & -\Delta_{13} & -\Delta_{23} & 0 \\ \hline \psi_1(-\mathbf{k}) & 0 & -\Delta_{12}^* & -\Delta_{13}^* & -\xi_1(-\mathbf{k}) & -\Omega & 0 \\ \psi_2(-\mathbf{k}) & \Delta_{12}^* & 0 & -\Delta_{23}^* & -\Omega & -\xi_2(-\mathbf{k}) & -\Omega \\ \psi_3(-\mathbf{k}) & \Delta_{13}^* & \Delta_{23}^* & 0 & 0 & -\Omega & -\xi_3(-\mathbf{k}) \end{array}\right), \tag{4.24}$$

where Ω is the Rabi frequency, and the basis in which the Hamiltonian matrix is written is made explicit in order to facilitate visualization and interpretation of the terms. The diagonal blocks of the matrix Hamiltonian $\mathbf{H}_T^{\mathrm{mf}}(\mathbf{k})$ are simply the light-atom interaction matrices $\mathbf{H}_{LA}(\mathbf{k})$ (top diagonal block) and $-\mathbf{H}_{LA}(-\mathbf{k})$ (lower diagonal blocks). The off-diagonal blocks reflect pairing between different hyperfine states.

Now that the mean field Hamiltonian is known, I will analyse next the thermodynamic potential and the system of self-consistent equations satisfied by the order parameter $\Delta_{ss'}$ and the chemical potential μ.

4.3.2 Thermodynamic Potential and Self-Consistency Relations

The thermodynamic potential is

$$\mathcal{Q} = -T\left(\ln \mathcal{Z}\right), \tag{4.25}$$

when expressed in terms of the Grand Canonical partition function

$$\mathcal{Z} = \mathrm{Tr}\left(e^{-H_T/T}\right), \tag{4.26}$$

where T is the temperature ($k_B = 1$) and H_T is the total Hamiltonian of the system (including the chemical potential term) defined in Eq. (4.18).

To obtain $\mathcal{Q}$ at the mean field level, it is necessary to find out the eigenvalues of the Hamiltonian matrix $\mathbf{H}_T^{\rm mf}(\mathbf{k})$ defined in Eq. (4.24). This matrix has six eigenvalues $E_j(\mathbf{k})$, and it is convenient to order them from highest to lowest energies as follows $E_1(\mathbf{k}) > E_2(\mathbf{k}) > E_3(\mathbf{k}) > E_4(\mathbf{k}) > E_5(\mathbf{k}) > E_6(\mathbf{k})$. The three higher eigenvalues (E_1, E_2, E_3) are guaranteed to be positive and describe quasi-particle excitations, while the three lowest eigenvalues (E_4, E_5, E_6) are guaranteed to be negative and describe quasi-hole excitations. In addition, $\mathbf{H}_T^{\rm mf}(\mathbf{k})$ exhibits quasi-particle/quasi-hole symmetry, which means that the quasi-particle and quasi-hole eigenvalues are related by the following transformation $E_6(\mathbf{k}) = -E_1(-\mathbf{k})$, $E_5(\mathbf{k}) = -E_2(-\mathbf{k})$, and $E_4(\mathbf{k}) = -E_3(-\mathbf{k})$.

These eigenvalues need to be obtained numerically, but the mean field thermodynamic potential

$$\mathcal{Q}_{\rm mf} = -\frac{T}{2}\sum_{\mathbf{k}j} \ln\left(1 + e^{-E_j(\mathbf{k})/T}\right) + \frac{1}{2}\sum_{\mathbf{k}s} \xi_s(-\mathbf{k}) - \sum_{s\neq s'} \frac{|\Delta_{ss'}|^2}{g_{ss'}} \tag{4.27}$$

can be easily written in terms of $E_j(\mathbf{k})$ with $j = \{1, 2, 3, 4, 5, 6\}$, the kinetic terms $\xi_s(-\mathbf{k})$ and the order parameters $\Delta_{ss'}$, with $\{s, s'\} = \{1, 2, 3\}$.

In order to determine the phase diagrams of three-hyperfine-state Fermi superfluids and their excitation spectrum, it is necessary to establish self-consistently the order parameter $\Delta_{ss'}$ for superfluidity and the chemical potential μ that fixes the total number N of fermions. The order parameter equations for the potentially three order parameters $\{\Delta_{12}, \Delta_{13}, \Delta_{23}\}$ are determined from the saddle-point condition

$$\frac{\partial \mathcal{Q}}{\partial \Delta_{ss'}^*} = \frac{1}{2}\sum_{\mathbf{k}}\sum_{j=1}^{3} \tanh\left(\frac{\beta E_j(\mathbf{k})}{2}\right)\frac{\partial E_j(\mathbf{k})}{\partial \Delta_{ss'}^*} - \frac{V}{g_{ss'}}\Delta_{ss'} = 0, \tag{4.28}$$

while the number equation from the thermodynamic relation

$$N = -\frac{\partial \mathcal{Q}}{\partial \mu} = \frac{1}{2}\sum_{\mathbf{k}}\left[\sum_{j=1}^{3} \tanh\left(\frac{\beta E_i(\mathbf{k})}{2}\right)\frac{\partial E_j(\mathbf{k})}{\partial \mu} + 3\right]. \tag{4.29}$$

In the expressions above, notice that the summations over eigenvalues only involve the quasi-particle energies $E_1(\mathbf{k})$, $E_2(\mathbf{k})$ and $E_3(\mathbf{k})$, as the quasi-particle/quasi-hole symmetry was used to elimminate the quasi-hole energies $E_4(\mathbf{k})$, $E_5(\mathbf{k})$ and $E_6(\mathbf{k})$.

Once these self-consistent equations are solved to determine the order parameters $\Delta_{ss'}$ and the chemical potential μ, then the quasi-particle/quasi-particle spectrum can be obtained and several spectroscopic properties can be calculated. Furthermore, all thermodynamic properties can be obtained from the thermodynamic potential $\mathcal{Q}$, within the mean field approximation. These calculations are currently in progress for the simpler case where there is pairing only between hyperfine states 1 and 3, that is when only $\Delta_{13} \neq 0$, and will reported as a separate publication in the future.

4.4 Conclusions

In this chapter, I have discussed a fermionic system involving three hyerfine states at fixed Rabi frequency, but changing artificial spin-orbit fields and quadratic Zeeman shifts induced by light-atom interactions using a Raman coupling scheme. By adjusting the artificial quadratic Zeeman shift it was possible to tune through regimes where only one, two or three-hyperfine states are important. Lifshitz transitions and Pomeranchuk deformations of the Fermi surfaces were studied for varying quadratic Zeeman shifts. Several spectroscopic properties spectroscopic properties were studied including energy dispersion, Fermi surfaces, spectral function, spin-dependent momentum distribution and density of states.

The possibility of superfluidity in three-hyperfine state fermions was also discussed at the mean field level. The mean field thermodynamic potential, as well as self-consistent equations for the order parameter and particle number were obtained, but not yet solved. It is hoped that in the immediate future, these equations will be solved numerically to obtain the phase diagram of this rich system as a function of the quadratic Zeeman shift and the Rabi frequency, as least in simpler cases, where

possible topological phase transitions make take place.

CHAPTER V

CONCLUSIONS

In this thesis, I have discussed the effects of artificial spin-orbit and Zeeman fields in systems consisting of ultra-cold fermions. I explored two general aspects of such systems. The first aspect was the exploration of few-body physics of fermions with two relevant hyperfine states, and the second aspect was the investigation of many-body physics of fermions with three relevant hyperfine states. My work was inspired by the experimental realization of these artificial fields for Fermi atoms such as ^{40}K.

Regarding the few-body physics aspect, I have analysed the existence of two-body bound states as a function of spin-orbit coupling strength, Zeeman fields and atom-atom interactions for fermionic atoms with two relevant hyperfine states. Such systems were investigated in the regime where only s-wave interactions are important, and where the two-particles reside either in free space or in a harmonically confining potential. In the case of free space, I have obtained the energies and effective masses of the two-body bound states, which were used to calculate the Bose-Einstein condensation temperature of these molecular states. In the case of a harmonically confining potential, I have investigated the changes in the energy of two-body bound states produced by this potential.

Concerning the many-body physics aspect of this thesis, I explored a novel direction corresponding to the physics of ultra-cold fermions with three relevant hyperfine states in the presence of artificial spin-orbit and Zeeman fields. In the case of three hyperfine states, it is also possible to have an additional term corresponding to an artificial quadratic Zeeman shift. A possible experimental system corresponding to

this situation is ultra-cold fermionic ^{40}K, when these atoms are trapped in three distinct hyperfine states. In the case where the Fermi atoms where non-interacting, I analysed spectroscopic properties such as energy spectrum, momentum distribution, Fermi surfaces and density of states as a function of artificial spin-orbit coupling, Zeeman fields and quadratic Zeeman shift. When interactions were included, I explored the possibility of superfluid phases, and derived self-consistency relations for the order parameters and chemical potential of the system. Lastly, I found out that these relations allow for a description of the quantum phases of three-hyperfine-state fermions, which may include topological superfluidity.

CHAPTER VI

APPENDIX

6.1 Appendix I: Kronecker Products for Pauli Spin Matrices in Chapter II

In this appendix, I display the Kronecker products of 2×2 Pauli matrices, which are used to construct the Hamiltonian of two non-interacting fermions in chapter II.

The identity and individual Pauli matrices are

$$\mathbf{1} = \begin{pmatrix} 1 & 0 \\ 0 & 1 \end{pmatrix} \quad \boldsymbol{\sigma}_x = \begin{pmatrix} 0 & 1 \\ 1 & 0 \end{pmatrix} \quad \boldsymbol{\sigma}_y = \begin{pmatrix} 0 & -i \\ i & 0 \end{pmatrix} \quad \boldsymbol{\sigma}_z = \begin{pmatrix} 1 & 0 \\ 0 & -1 \end{pmatrix}.$$

The corresponding Kronecker products of the relevant matrices are

$$\mathbf{1} \otimes \mathbf{1} = \begin{pmatrix} 1 & 0 & 0 & 0 \\ 0 & 1 & 0 & 0 \\ 0 & 0 & 1 & 0 \\ 0 & 0 & 0 & 1 \end{pmatrix},$$

$$\boldsymbol{\sigma}_x \otimes \mathbf{1} = \begin{pmatrix} 0 & 0 & 1 & 0 \\ 0 & 0 & 0 & 1 \\ 1 & 0 & 0 & 0 \\ 0 & 1 & 0 & 0 \end{pmatrix} \quad , \quad \mathbf{1} \otimes \boldsymbol{\sigma}_x = \begin{pmatrix} 0 & 1 & 0 & 0 \\ 1 & 0 & 0 & 0 \\ 0 & 0 & 0 & 1 \\ 0 & 0 & 1 & 0 \end{pmatrix}$$

$$\boldsymbol{\sigma}_y \otimes \mathbf{1} = \begin{pmatrix} 0 & 0 & -i & 0 \\ 0 & 0 & 0 & -i \\ i & 0 & 0 & 0 \\ 0 & i & 0 & 0 \end{pmatrix} \quad , \quad \mathbf{1} \otimes \boldsymbol{\sigma}_y = \begin{pmatrix} 0 & -i & 0 & 0 \\ i & 0 & 0 & 0 \\ 0 & 0 & 0 & -i \\ 0 & 0 & i & 0 \end{pmatrix}$$

$$\boldsymbol{\sigma}_z \otimes \mathbf{1} = \begin{pmatrix} 1 & 0 & 0 & 0 \\ 0 & 1 & 0 & 0 \\ 0 & 0 & -1 & 0 \\ 0 & 0 & 0 & -1 \end{pmatrix} \quad \text{and} \quad \mathbf{1} \otimes \boldsymbol{\sigma}_z = \begin{pmatrix} 1 & 0 & 0 & 0 \\ 0 & -1 & 0 & 0 \\ 0 & 0 & 1 & 0 \\ 0 & 0 & 0 & -1 \end{pmatrix}.$$

6.2 Appendix II: Derivation of Eigenvalue Equation in Chapter II

In this appendix, I display the computer code written in *Mathematica* to perform the symbolic manipulation of the Gaussian ellimination method that leads to Eqs. (2.40), (2.43), (2.44), (2.48) and (2.50) in chapter II. I solve for the most general case involving an arbitrary mixture of Rashba and Dresselhaus terms, as well finite Zeeman fields h_y and h_z, from which all the particular case can be obtained.

After the Gaussian ellimination method is used or after the direct application of the formal solution shown in Eq. (2.39), the Schroedinger's equation becomes

$$\phi_{00}(\mathbf{k}, \mathbf{K}) = f(\mathbf{k}, \mathbf{K}, h_z, h_y, v_R, v_D, E) \frac{g}{L^3} \sum_{\mathbf{k}} \phi_{00}(\mathbf{k}, \mathbf{K}),$$

where I explictly showed all the important variable dependencies of the function f to indicate that this derivation corresponds to the most general case where all the external variables are non-zero, that is, $\{v_R, v_D, h_y, h_z\} \neq 0$.

A summation (integration) of the expression above over relative momenta $\mathbf{k}$ leads to the relation

$$\sum_{\mathbf{k}} \phi_{00}(\mathbf{k}, \mathbf{K}) = \sum_{\mathbf{k}} f(\mathbf{k}, \mathbf{K}, h_z, h_y, v_R, v_D, E) \frac{g}{L^3} \sum_{\mathbf{k}} \phi_{00}(\mathbf{k}, \mathbf{K}),$$

which produces the desired result

$$\frac{1}{g} = \frac{1}{L^3} \sum_{\mathbf{k}} f(\mathbf{k}, \mathbf{K}, h_z, h_y, v_R, v_D, E),$$

upon cancellation of the common factor $\sum_{\mathbf{k}} \phi_{00}(\mathbf{k}, \mathbf{K})$ on both sides of the equation.

The most general form of the function f in compact notation is

$$f(\mathbf{k},\mathbf{K},h_z,h_y,v_R,v_D,E)=\frac{\mathcal{E}_{\mathbf{k},\mathbf{K}}\left(\mathcal{E}_{\mathbf{k},\mathbf{K}}^2-4h_z^2-\mathbf{b}^2\right)}{\mathcal{E}_{\mathbf{k},\mathbf{K}}^4-\mathcal{E}_{\mathbf{k},\mathbf{K}}^2\left(4\mathbf{a}^2+\mathbf{b}^2+4h_z^2\right)+4\left(\mathbf{a}\cdot\mathbf{b}\right)}, \tag{6.1}$$

where I used the notation $\mathcal{E}_{\mathbf{k},\mathbf{K}}=E-\epsilon_{\mathbf{k},\mathbf{K}}$, and the vectors appearing in the expression above are $\mathbf{a}=\gamma k_x\mathbf{e}_x+\beta k_y\mathbf{e}_y$ and $\mathbf{b}=\left(2h_y+\gamma K_x\right)\mathbf{e}_x+\beta K_y\mathbf{e}_y$. Recall that the coefficients $\beta=v_D-v_R$ and $\gamma=v_D+v_R$, relate directly to Rashba and Dresselhaus velocities v_R and v_D.

The code written in *Mathematica* is shown in Fig. 6.1 and gives the inverse of the function f defined above.

6.3 Appendix III: Derivation of the Bound State Energy for ERD spin-orbit coupling in Chapter II

In this appendix, I solve analytically for the bound state energy for ERD spin-orbit without the presence of Zeeman fields. I will use the general method outlined in chapter II, which is more powerful for more complex cases. The reason for using this more powerful method for this simpler case is to gain confidence in the method and its results.

The unitarity matrix $\mathbf{V}$ used to diagonalize the Hamiltonian $\mathbf{H}_0$ described in Eq. (2.27) contains the components of the eigenvector of $\mathbf{H}_0$ and has the form

$$\mathbf{V}=\begin{pmatrix} -\frac{i\mathrm{sgn}(k_x)}{\sqrt{2}} & 0 & \frac{i\mathrm{sgn}(k_x)}{2} & -\frac{i\mathrm{sgn}(k_x)}{2} \\ 0 & 1 & 0 & 0 \\ \frac{i\mathrm{sgn}(k_x)}{\sqrt{2}} & 0 & \frac{i\mathrm{sgn}(k_x)}{2} & -\frac{i\mathrm{sgn}(k_x)}{2} \\ 0 & 0 & \frac{1}{\sqrt{2}} & \frac{1}{\sqrt{2}} \end{pmatrix},$$

when the center of mass momentum is set to zero, that is, $\mathbf{K}=\mathbf{0}$. This matrix is also used to diagonalize $\mathbf{H}_0-E\mathbf{1}$, where E is the energy eigenvalue and $\mathbf{1}$ is identity,

leading to the following result

$$\mathbf{V}(\mathbf{H}_0 - E\mathbf{1})\mathbf{V}^\dagger = \mathbf{H}_0' - E\mathbf{1} = \begin{pmatrix} \epsilon_{\mathbf{k},0} - E & 0 & 0 & 0 \\ 0 & \epsilon_{\mathbf{k},0} - E & 0 & 0 \\ 0 & 0 & \epsilon_{\mathbf{k},0} - E - 2vk_x & 0 \\ 0 & 0 & 0 & \epsilon_{\mathbf{k},0} - E + 2vk_x \end{pmatrix}.$$

The corresponding four-dimensional spinor in the rotated basis is $\mathbf{\Lambda}(\mathbf{k}, \mathbf{K}) = \mathbf{V}\mathbf{\Phi}(\mathbf{k}, \mathbf{K})$, which in the case of $\mathbf{K} = \mathbf{0}$, becomes

$$\mathbf{\Lambda}(\mathbf{k}, \mathbf{0}) = \mathbf{V}\mathbf{\Phi}(\mathbf{k}, \mathbf{0}) = \begin{pmatrix} i\frac{\phi_{1,1}(\mathbf{k},\mathbf{0}) - \phi_{1,-1}(\mathbf{k},\mathbf{0})}{\sqrt{2}} \\ \phi_{1,0}(\mathbf{k}, 0) \\ \frac{1}{2}\left(-i\phi_{1,1}(\mathbf{k}, \mathbf{0}) - i\phi_{1,-1}(\mathbf{k}, \mathbf{0}) + \sqrt{2}\phi_{0,0}(\mathbf{k}, \mathbf{0})\right) \\ \frac{1}{2}\left(i\phi_{1,1}(\mathbf{k}, \mathbf{0}) + i\phi_{1,-1}(\mathbf{k}, \mathbf{0}) + \sqrt{2}\phi_{0,0}(\mathbf{k}, \mathbf{0})\right) \end{pmatrix}.$$

A similar transformation can be used for the action of the interaction matrix $\mathbf{H}_I$ on $\mathbf{\Phi}(\mathbf{k}, \mathbf{K})$ leading to the transformation $\mathbf{H}_I\mathbf{\Phi}(\mathbf{k}, \mathbf{K}) \rightarrow \mathbf{H}_I'\mathbf{\Lambda}(\mathbf{k}, \mathbf{K})$, where $\mathbf{H}_I' = \mathbf{V}\mathbf{H}_I\mathbf{V}^\dagger$. Therefore the transformation $\mathbf{V}\mathbf{H}_I\mathbf{V}^\dagger\mathbf{V}\mathbf{\Phi} = \mathbf{H}_I'\mathbf{\Lambda}$, which is shown below as

$$\mathbf{V}\mathbf{H}_I\mathbf{\Phi}(\mathbf{k}, 0) = \mathbf{V}\mathbf{H}_I\mathbf{V}^\dagger\mathbf{V}\mathbf{\Phi}(\mathbf{k}, 0) = \mathbf{H}_I'\mathbf{\Lambda}(\mathbf{k}, \mathbf{0}) = \begin{pmatrix} 0 \\ 0 \\ -\frac{g}{L^3\sqrt{2}}\sum_{\mathbf{k}} \phi_{0,0}(\mathbf{k}, \mathbf{0}) \\ -\frac{g}{L^3\sqrt{2}}\sum_{\mathbf{k}} \phi_{0,0}(\mathbf{k}, \mathbf{0}) \end{pmatrix},$$

given that $\mathbf{V}$ satisfies the unitarity condition $\mathbf{V}\mathbf{V}^\dagger = \mathbf{1}$.

The corresponding Schroedinger's equation for the ERD case can then be solved using the method in appendix II, and leads to

$$\frac{(\epsilon_{\mathbf{k},0} - E)^2 - 4v^2k_x^2}{\epsilon_{\mathbf{k},0} - E}\phi_{0,0}(\mathbf{k}, \mathbf{0}) = \frac{g}{L^3}\sum_{\mathbf{k}'} \phi_{0,0}(\mathbf{k}', \mathbf{0}),$$

which upon summation over the relative momentum coordinate $\mathbf{k}$ produces the integral equation

$$\frac{1}{g} = \frac{1}{L^3}\sum_{\mathbf{k}} \frac{\epsilon_{\mathbf{k},0} - E}{(\epsilon_{\mathbf{k},0} - E)^2 - 4v^2k_x^2}$$

for the eigenvalues of the two fermion problem. Fortunately, this integral equation can be solved analytically in the simple case that we are considering through a series of standard calculus manipulations which are displayed below.

Starting from the relation

$$\frac{1}{g} = \frac{1}{(2\pi)^3}\int d\mathbf{k}\frac{\epsilon_{\mathbf{k},0}-E}{\left(\epsilon_{\mathbf{k},0}-E\right)^2-4v^2k_x^2}, \tag{6.2}$$

where summations over $\mathbf{k}$ were replaced by integrals over $\mathbf{k}$, I replace the interaction parameter g in favor of the scattering length on the left hand side of the previous relation. At the same time I use cylindrical coordinates in momentum space to obtain the expression

$$-\frac{m}{4\pi a_s}+\frac{1}{(2\pi)^3}\int d\mathbf{k}\frac{1}{\epsilon_{\mathbf{k},0}} = \frac{m}{(2\pi)^3}\iiint dk_x k dk d\theta \frac{k^2+k_x^2-mE}{(k^2+k_x^2-mE)^2-4m^2v^2k_x^2}. \tag{6.3}$$

The next step in the manipulations is to decompose the integrand in the right hand side of the previous equation into partial fractions, while using the explicit form of $\epsilon_{\mathbf{k},0}$ on the left hand side. These operations lead to the intermediate expression

$$-\frac{m}{4\pi a_s}+\frac{m}{(2\pi)^3}\iiint \frac{dk_x k dk d\theta}{k_x^2+k^2} = \frac{m}{(2\pi)^3}\frac{1}{2}\iiint dk_x k dk d\theta \sum_{\eta=\pm}\left[\frac{1}{k^2+k_x^2-mE+\eta 2mvk_x}\right] \tag{6.4}$$

Integrations over the angle θ and k_x lead to the final integral

$$-\frac{m}{4\pi a_s} = \frac{m}{(2\pi)^2}\int kdk\left(\frac{1}{\sqrt{k^2-mE-m^2v^2}}-\frac{1}{k}\right), \tag{6.5}$$

which can be easily performed to give the simple result

$$\frac{1}{a_s} = \sqrt{-mE-m^2v^2}$$

This result shows that a_s must be positive, since it is a real quantity. Furthermore, squaring the previous relations gives the standard result for the bound state energy

$$E = E_B = -\frac{1}{ma_s^2}-mv^2,$$

where mv^2 is just the Galilean boost given to the atoms by the ERD spin-orbit coupling which was not explicitly included in the Hamiltonian, thus changing the

minimum energy of two free fermions to $-mv^2$. However the binding energy E_{Bin} is the difference between the bound state energy E_B and the lowest energy of two free fermions, leading therefore to the final result

$$E_{Bin} = E_B + mv^2 = -\frac{1}{ma_s^2}, \tag{6.6}$$

which shows that the binding energy is not affected by the ERD spin-orbit coupling, when the Zeeman fields are not included. This is not surprising because in the case of zero Zeeman fields, and ERD spin-orbit only, our system is Galilean invariant, and the boost provided by the ERD field can be gauged away. However, this is not the case of Rashba or Dresselhaus fields.

6.4 Appendix IV: Derivation of Bound State Energy for Rashba spin-orbit coupling in Chapter II

In this appendix, I present the derivation of the bound state energy, at the zero center of mass momentum ($\mathbf{K} = \mathbf{0}$), for two fermions in the presence of Rashba spin-orbit coupling v_R, but without Zeeman fields. I use the same method outlined in chapter II, and in Appendix III. The rotation matrix in the Rashba case is

$$\mathbf{V} = \begin{pmatrix} -\frac{k_x+ik_y}{\sqrt{2}(k_x-ik_y)} & 0 & \frac{1}{\sqrt{2}} & 0 \\ 0 & 1 & 0 & 0 \\ \frac{ik_x-k_y}{2k_\perp} & 0 & \frac{ik_x+k_y}{2k_\perp} & \frac{1}{\sqrt{2}} \\ \frac{-ik_x+k_y}{2k_\perp} & 0 & \frac{-ik_x-k_y}{2k_\perp} & \frac{1}{\sqrt{2}} \end{pmatrix},$$

which I apply to the Hamiltonian $\mathbf{H}_0$ for the Rashba system leading to the diagonal form

$$\mathbf{V}(\mathbf{H}_0 - E\mathbf{1})\mathbf{V}^\dagger = \mathbf{H}_0' - E\mathbf{1} = \begin{pmatrix} \epsilon_{\mathbf{k},0} - E & 0 & 0 & 0 \\ 0 & \epsilon_{\mathbf{k},0} - E & 0 & 0 \\ 0 & 0 & \epsilon_{\mathbf{k},0} - E + 2v_R k_\perp & 0 \\ 0 & 0 & 0 & \epsilon_{\mathbf{k},0} - E - 2v_R k_\perp \end{pmatrix},$$

where $k_\perp = \sqrt{k_x^2 + k_y^2}$ is the magnitude of the relative momentum in the xy plane.

The corresponding four-dimensional spinor in the rotated basis is $\mathbf{\Lambda}(\mathbf{k}, \mathbf{K}) = \mathbf{V}\mathbf{\Phi}(\mathbf{k}, \mathbf{K})$, which in the case of $\mathbf{K} = \mathbf{0}$, becomes

$$\mathbf{\Lambda}(\mathbf{k}, \mathbf{0}) = \mathbf{V}\mathbf{\Phi}(\mathbf{k}, \mathbf{0}) = \begin{pmatrix} -\frac{k_x - ik_y}{\sqrt{2}(k_x + ik_y)}\phi_{1,1} - \frac{ik_x + k_y}{2k_\perp}\left(\phi_{1,-1} - \phi_{0,0}\right) \\ \phi_{1,0} \\ \frac{1}{\sqrt{2}}\phi_{1,1} + \frac{-ik_x + k_y}{2k_\perp}\left(\phi_{1,-1} - \phi_{0,0}\right) \\ \frac{\phi_{1,-1} + \phi_{0,0}}{\sqrt{2}} \end{pmatrix},$$

where I have dropped the momentum arguments $(\mathbf{k}, \mathbf{0})$ of the function $\phi_{s,m_s}(\mathbf{k}, \mathbf{0})$ for the sake of symplifying the notation in the matrix.

The corresponding transformation for the interaction part of the Hamiltonian leads to

$$\mathbf{V}\mathbf{H}_I\mathbf{\Phi}(\mathbf{k}, 0) = \mathbf{V}\mathbf{H}_I\mathbf{V}^\dagger\mathbf{V}\mathbf{\Phi}(\mathbf{k}, 0) = \mathbf{H}_I'\mathbf{\Lambda}(\mathbf{k}, \mathbf{0}) = -g \begin{pmatrix} \frac{ik_x + k_y}{2k_\perp} \\ 0 \\ \frac{ik_x - k_y}{2k_\perp} \\ \frac{1}{\sqrt{2}} \end{pmatrix} \sum_{\mathbf{k}} \phi_{0,0}(\mathbf{k}, 0),$$

given that $\mathbf{V}$ satisfies the unitarity condition $\mathbf{V}\mathbf{V}^\dagger = \mathbf{1}$.

The resulting Schroedinger's equation matrix for the Rashba case can be reduced by Gaussian ellimination to the integral equation

$$\frac{(\epsilon_{\mathbf{k},0} - E)^2 - 4v_R^2 k_\perp^2}{(\epsilon_{\mathbf{k},0} - E)}\phi_{0,0}(\mathbf{k}, \mathbf{0}) = \frac{g}{L^3}\sum_{\mathbf{k}'} \phi_{0,0}(\mathbf{k}', \mathbf{0}),$$

where $k_\perp = \sqrt{k_x^2 + k_y^2}$. Integration over the relative momentum $\mathbf{k}$ leads to the relation

$$\frac{1}{g} = \frac{1}{L^3}\sum_{\mathbf{k}} \frac{(\epsilon_{\mathbf{k},0} - E)}{(\epsilon_{\mathbf{k},0} - E)^2 - 4v_R^2 k_\perp^2}.$$

Transforming the summation over momenta into an integral produces

$$\frac{1}{g} = \frac{1}{(2\pi)^3}\int d\mathbf{k} \frac{(\epsilon_{\mathbf{k},0} - E)}{(\epsilon_{\mathbf{k},0} - E)^2 - 4v_R^2 k_\perp^2},$$

which in turn can be written in terms of cylindrical coordinates as $\mathbf{k} = (k_\perp, \theta, k_z)$. After a trivial integration over θ, I obtain the expression

$$\frac{1}{g} = \frac{m}{4\pi^2} \iint k_\perp dk_\perp dk_z \frac{k_\perp^2 + k_z^2 - mE}{(k_\perp^2 + k_z^2 - mE)^2 - 4m^2 v_R^2 k_\perp^2}.$$

The next step is to replace the interaction g in favor of the scattering length and to reorganize the relation in the form

$$-\frac{m}{4\pi a_s} = \frac{m}{8\pi} \int k_\perp dk_\perp \left(\frac{1}{\sqrt{k_\perp^2 - 2mv_R k_\perp - mE}} + \frac{1}{\sqrt{k_\perp^2 + 2mv_R k_\perp - mE}} - \frac{2}{k_\perp} \right),$$

which upon integration over $k_\perp$ generates an expression relating the scattering length a_s and the energy of the bound state $E = E_B$ given by

$$-\frac{m}{4\pi a_s} = -\frac{\sqrt{-mE}}{4\pi} - \frac{mv_R}{8\pi} \ln \left[\frac{\sqrt{-mE} - mv_R}{\sqrt{-mE} + mv_R} \right].$$

This last relation can be also be written in a equivalent form by exponentiating the natural logarithm, giving the result

$$\exp \left[\frac{1}{mv_R} \left(2\sqrt{-mE} - \frac{2}{a_s} \right) \right] = \frac{\sqrt{-mE} + mv_R}{\sqrt{-mE} - mv_R}.$$

A simple graphical solution of the relation above shows that bound states occur for all values of a_s, in sharp contrast to result found in the ERD case, where it was necessary for a_s to be positive. In the Rashba case with no Zeeman fields, any value of a_s gives a bound state. This means that an arbitrary small attractive interaction g produces a bound state in three-dimensions when the Rashba spin-orbit is present. Physically this occurs because the effective density of states of the system is modified by the Rashba field to that of a one-dimensional system, where no critical value of g is necessary to produce a bound state. A particularly interesting value for the bound state energy occurs at unitarity, where $a_s \to \infty$. In this case the bound state energy is

$$E = -(1.43923) m v_R^2,$$

a result that is in agreement with an earlier paper [17].

6.5 Appendix V: Derivation of Bound State Energy for Arbitrary Mixture of Rashba and Dresselhaus spin-orbit coupling in Chapter II

In this appendix, I will obtain the bound state energy for an arbitrary mixture of Rashba and Dresselhaus spin-orbit coupling for zero center of mass momentum $\mathbf{K} = \mathbf{0}$ and zero Zeeman fields $h_y = h_z = 0$.

In the case of an arbitrary mixture of Rashva and Dresselhaus terms the integral equation for energy eigenvalues of the corresponding Schroedinger's equation is

$$\frac{1}{g} = \frac{1}{L^3} \sum_{\mathbf{k}} \frac{\mathcal{E}_{\mathbf{k},0}}{\mathcal{E}_{\mathbf{k},0}^2 - 4\mathbf{a}\cdot\mathbf{a}},$$

where the vector $\mathbf{a} = \gamma k_x \mathbf{e}_x + \beta k_y \mathbf{e}_y$, and $\mathcal{E}_{\mathbf{k},0} = \epsilon_{\mathbf{k},0} - E$. A more explicit form of the relation above is

$$\frac{1}{g} = \frac{1}{L^3} \sum_{\mathbf{k}} \frac{\left(\epsilon_{\mathbf{k},0} - E\right)^2}{\left(\epsilon_{\mathbf{k},0} - E\right)^2 - 4\left(k_x^2\gamma + \beta^2 k_y^2\right)},$$

which can have its sum over momenta converted into an integration leading to the expression

$$\frac{1}{g} = \frac{m}{(2\pi)^3} \int_{-\infty}^{\infty} dk_z \int_{-\infty}^{\infty} dk_y \int_{-\infty}^{\infty} dk_x \frac{\left(k_x^2 + k_y^2 + k_z^2 - mE\right)^2}{\left(k_x^2 + k_y^2 + k_z^2 - mE\right)^2 - 4m^2\left(k_x^2\gamma^2 + \beta^2 k_y^2\right)}.$$

An integration over the variable k_z gives a double integral in the momentum components k_x and k_y given by

$$\frac{1}{g} = \frac{m}{16\pi^2} \int_{-\infty}^{\infty} dk_y \int_{-\infty}^{\infty} dk_x \sum_{\eta=\pm} \left(\frac{1}{\sqrt{k_x^2 + k_y^2 - mE + \eta 2m\sqrt{k_y^2\beta^2 + k_x^2\gamma^2}}} \right),$$

which can be further written in polar coordinates $(k_x, k_y) \to (k, \theta)$ as

$$\frac{1}{g} = \frac{m}{16\pi^2} \int_0^{\infty} k dk \int_0^{2\pi} d\theta \sum_{\eta=\pm} \left(\frac{1}{\sqrt{k^2 - mE + \eta 2mk\sqrt{\beta^2 \sin^2\theta + \gamma^2 \cos^2\theta}}} \right).$$

The replacement of g in favor of the scattering length and a subsequent integration of the expression over radial momentum k leads to an integral over the angle θ in the

form

$$-\frac{m}{4\pi a_s} = -\frac{m^2\gamma}{16\pi^2}\int_0^{2\pi} d\theta \left(2\nu + \sqrt{1-\mu\sin^2\theta}\ln\left[\frac{\nu-\sqrt{1-\mu\sin^2\theta}}{\nu+\sqrt{1-\mu\sin^2\theta}}\right]\right),$$

which, after a trivial integral of the first term on the right had side, can be rearranged as

$$\frac{1}{a_s} - m\gamma\nu = \frac{m\gamma}{\pi}\int_0^{\pi/2} d\theta\sqrt{1-\mu\sin^2\theta}\ln\left[\frac{\nu-\sqrt{1-\mu\sin^2\theta}}{\nu+\sqrt{1-\mu\sin^2\theta}}\right].$$

A final division of the previous equation by the factor $m\gamma/\pi$ leads to the expression

$$\frac{\pi}{m\gamma a_s} - \pi\nu = \int_0^{\pi/2} d\theta\sqrt{1-\mu\sin^2\theta}\ln\left[\frac{\nu-\sqrt{1-\mu\sin^2\theta}}{\nu+\sqrt{1-\mu\sin^2\theta}}\right],$$

where I defined the parameters $\nu = \sqrt{-mE}/m\gamma$ and $\mu = 1-\beta^2/\gamma^2$. Notice that the ERD case corresponds to $\mu = 1$ and Rashba case corresponds to $\mu = 0$. Thus, I will use the parameter μ to be in the range $0 < \mu < 1$.

This definition of parameters permits a series expansion of integrand in the right hand side of the previous expression with respect to μ. This expansion takes the form

$$\sqrt{1-\mu\sin^2\theta}\ln\left[\frac{\nu-\sqrt{1-\mu\sin^2\theta}}{\nu+\sqrt{1-\mu\sin^2\theta}}\right] = \ln\left(\frac{\nu-1}{\nu+1}\right)\times ...$$
$$... \times \left[1 - \sum_{n=1}^{\infty}\frac{(2n-1)!!}{(2n)!!(2n-1)}\sin^{2n}\theta\mu^n\right] + \sum_{n=1}^{\infty}\frac{\mu^n\sin^{2n}\theta}{(2n)!!}\frac{P_n(\nu)}{(\nu^2-1)^n},$$

which can be used to perform the integrations over θ. In order to perform this final integration it is useful to recall the relation

$$\int_0^{\pi/2} d\theta\sin^{2n}\theta = \frac{\pi}{2}\frac{(2n-1)!!}{(2n)!!},$$

and then utilize the power series expansion of the complete elliptic integral of the second kind

$$E\left(\frac{\pi}{2}\middle|\,\mu\right) = \frac{\pi}{2}\left\{1 - \sum_{n=1}^{\infty}\left[\frac{(2n-1)!!}{(2n)!!(2n-1)}\right]^2\mu^n\right\},$$

to produce the equation relating the s-wave scattering length and the energy E of the bound state:

$$\frac{\pi}{m\gamma a_s} - \pi\nu = \ln\left[\frac{\nu-1}{\nu+1}\right] E\left(\frac{\pi}{2}\middle|\,\mu\right) + \frac{\pi}{2}\sum_{n=1}^{\infty}\frac{(2n-1)!!}{[(2n)!!]^2}\frac{P_n(\nu)}{(\nu^2-1)^n}\mu^n.$$

Up to fifth order, the orthogonal polynomials $P_n(\nu)$ are

$$\begin{aligned}
P_1(\nu) &= 2\nu, \\
P_2(\nu) &= -2(\nu+\nu^3), \\
P_3(\nu) &= 6\nu + 16\nu^3 - 6\nu^5, \\
P_4(\nu) &= -2\nu(15 + 73\nu^2 - 55\nu^4 + 15\nu^6), \\
P_5(\nu) &= 2\nu(105 + 790\nu^2 - 896\nu^4 + 490\nu^6 - 105\nu^8).
\end{aligned}$$

It is important to notice that for the practical purpose of estabilishing the relationship between the s-wave scattering length a_s, the energy of the bound state E and its dependence on the spin-orbit parameters β and γ, the expression containing a single integral over the angular variable θ is more than sufficient.

6.6 Appendix VI: Computer code to calculate the effective mass for ERD, Rashba and Arbitrary mixture Rashba and Dresselhaus spin-orbit coupling in Chapter II

The computer code that uses symbolic manipulation to calculate the effective mass tensor defined in chapter II is shown sequentially in Figs. 6.2, 6.3, and 6.4. I used the symbolic manipulation routines from *Mathematica* to obtain the results for the effective masses.

6.7 Appendix VII: Derivation the Bose-Einstein condensate temperature in Chapter II

In this appendix, I will derive the Bose-Einstein condensation temperature of a dilute and non-interacting gas of two-fermion bound states (Feshbach molecules).

The density of bound states (Feshbach molecules), in the dilute and non-interacting regime where these molecules are bosonic in nature, is given by

$$n_{bs} = \frac{1}{L^3}\sum_{\mathbf{K}} b(\mathbf{K}) = \frac{1}{(2\pi)^3}\iiint dK_x dK_y dK_z \frac{1}{\exp\left[E_{\mathbf{K}} - \mu_{bs}\right]/T - 1},$$

where $b(\mathbf{K})$ is the Bose function, and

$$E_{\mathbf{K}} = E_0 + \frac{K_x^2}{2M_x} + \frac{K_y^2}{2M_y} + \frac{K_z^2}{2M_z} \tag{6.7}$$

is the bound state energy dispersion. Here, the masses M_i are directly related to the effective mass tensors of chapter II by the relation $M_i = m_{ii}$, that is, $M_x = m_{xx}$, $M_y = m_{yy}$ and $M_z = m_{zz}$.

Bose-Einstein condensation occurs when the chemical potential μ_{bs} reaches the lowest energy state available for the bound states, which corresponds to E_0. The temperature at which $\mu_{bs} = E_0$ is the Bose-Einstein condensation temperature T_{BEC}, which can be obtained from the relation

$$n_{bs} = \frac{1}{(2\pi)^3}\iiint dK_x dK_y dK_z \left(\exp\left[\frac{K_x^2}{2M_x} + \frac{K_y^2}{2M_y} + \frac{K_z^2}{2M_z}\right]/T_{BEC} - 1\right)^{-1}.$$

Using the scaling $\alpha = T_{BEC}^{-1/2} K_\alpha/\sqrt{2M_\alpha}$, to elliminate the momentum variables K_α, in favor of the dimensionless variables α, I can express the density of bound states as

$$n_{bs} = \frac{1}{(2\pi)^3}(2T_{BEC})^{3/2}\sqrt{M_x M_y M_z}\iiint \frac{dxdydz}{e^{x^2+y^2+z^2} - 1}.$$

Performing the triple dimensionless integral leads to the result

$$n_{bs} = C T_{BEC}^{3/2} M_{gm}^{3/2},$$

where $M_{gm} = (M_x M_y M_z)^{1/3}$ is the geometrical mean of the three masses $\{M_x, M_y, M_z\}$, and the constant $C = \sqrt{2}\zeta(3/2)/\pi^2$, with $\zeta(3/2)$ being the Riemann zeta function evaluated at 3/2.

To relate the Bose-Einstein condensation temperature with the Fermi energy of the Fermi atoms that make the molecular bound state, it is sufficient to notice that

there are two fermions per bound state. This means that the density of bound states n_{bs} is half of the density of fermions n_F, that is

$$n_{bs} = \frac{n_F}{2} = \frac{1}{2}\frac{2}{(2\pi)^3}\int\limits_{|\mathbf{k}|<k_F} d\mathbf{k}1.$$

Performing the integration above leads to

$$n_{bs} = \frac{k_F^2}{6\pi^2} = \frac{m^{3/2}}{6\pi^2}E_F^{3/2}$$

when the relation $E_F = k_F^2/(2m)$ between the Fermi energy E_F, the Fermi momentum k_F and the mass m of the fermions is used.

Using the explicit relation between n_{bs} and T_{BEC} in terms of the Fermi energy leads to the expression

$$CT_{BEC}^{3/2}M_{gm}^{3/2} = E_F^{3/2}\frac{(2m)^{3/2}}{6\pi^2}$$

which can be quickly rewritten as

$$\frac{T_{BEC}}{E_F} = \frac{2m}{M_{gm}}\left(\frac{1}{6\pi^2 C}\right)^{2/3}$$

corresponding to the desired result.

6.8 Appendix VIII: Derivation of Schroedinger's equation for harmonically trapped fermions with ERD spin-orbit coupling and Zeeman fields in Chapter III

In this appendix, I present a derivation of the Schroedinger's equation for harmonically trapped fermions in with ERD spin-orbit coupling and Zeeman fields described in Eq. (3.43) of Chapter III. This equation is the relevant differential equation when a Zeeman field h_z added along z direction is added. The Schroedinger's matrix equation using the singlet-triplet basis is

$$\begin{pmatrix} \hat{\mathcal{E}}_{r,R} - 2h_z & \frac{i}{\sqrt{2}}v\hat{P}_x & 0 & i\sqrt{2}v\hat{k}_x \\ -\frac{i}{\sqrt{2}}v\hat{P}_x & \hat{\mathcal{E}}_{r,R} & -\frac{i}{\sqrt{2}}v\hat{P}_x & 0 \\ 0 & \frac{i}{\sqrt{2}}v\hat{P}_x & \hat{\mathcal{E}}_{r,R} + 2h_z & i\sqrt{2}v\hat{k}_x \\ -i\sqrt{2}v\hat{k}_x & 0 & -i\sqrt{2}v\hat{k}_x & \hat{\mathcal{E}}_{r,R} \end{pmatrix} \begin{pmatrix} \psi_{11} \\ \psi_{10} \\ \psi_{1-1} \\ \psi_{00} \end{pmatrix} = \begin{pmatrix} 0 \\ 0 \\ 0 \\ g\delta(\mathbf{r})\partial_r(r\psi_{00}) \end{pmatrix}.$$

Carrying out the matrix multiplication leads to the four coupled differential equations

$$\begin{aligned}
\left(\hat{\mathcal{E}}_{r,R} - 2h_z\right)\psi_{11} + \frac{i}{\sqrt{2}}v\hat{P}_x\psi_{10} + i\sqrt{2}v\hat{k}_x\psi_{00} &= 0 \qquad (I)\\
-\frac{i}{\sqrt{2}}v\hat{P}_x\psi_{11} + \hat{\mathcal{E}}_{r,R}\psi_{10} - \frac{i}{\sqrt{2}}v\hat{P}_x\psi_{1-1} &= 0 \qquad (II)\\
\frac{i}{\sqrt{2}}v\hat{P}_x\psi_{10} + \left(\hat{\mathcal{E}}_{r,R} + 2h_z\right)\psi_{1-1} &= 0 \qquad (III)\\
-i\sqrt{2}v\hat{k}_x\left(\psi_{11} + \psi_{1-1}\right) + \hat{\mathcal{E}}_{r,R}\psi_{00} &= g\delta(\mathbf{r})\partial_r(r\psi_{00}), \quad (IV)
\end{aligned}$$

which can be manipulated by addition or subtractions of rows. Keeping in mind that ψ_{sm_s} are functions defined in real space coordinates, that is, $\psi_{sm_s} \equiv \psi_{sm_s}(\mathbf{r}, \mathbf{R})$, it is convenient to make the row substitutions $I + III \to I$ and $I - III \to III$ leading to the modified equations

$$\begin{aligned}
\hat{\mathcal{E}}_{r,R}\left(\psi_{11} + \psi_{1-1}\right) - 2h_z\left(\psi_{11} - \psi_{1-1}\right) + i2\sqrt{2}v\hat{k}_x\psi_{00} &= 0,\\
-i\frac{v}{\sqrt{2}}\hat{P}_x\left(\psi_{11} + \psi_{1-1}\right) + \hat{\mathcal{E}}_{r,R}\psi_{10} &= 0,\\
\hat{\mathcal{E}}_{r,R}\left(\psi_{11} - \psi_{1-1}\right) - 2h_z\left(\psi_{11} + \psi_{1-1}\right) - i\frac{2v}{\sqrt{2}}\hat{P}_x\psi_{10} &= 0,\\
-i\sqrt{2}v\hat{k}_x\left(\psi_{11} + \psi_{1-1}\right) + \hat{\mathcal{E}}_{r,R}\psi_{00} &= g\delta(\mathbf{r})\partial_r(r\psi_{00}).
\end{aligned}$$

In the set of equations above, I divide the first row by $2h_z$, and apply the differential operator $\hat{\mathcal{E}}_{r,R}^{-1}$ from the left to the second row in order to obtain an expression ψ_{10}, which is substituted on the third row, thus producing only a set of three coupled differential equations

$$\begin{aligned}
\left(\psi_{11} - \psi_{1-1}\right) &= \frac{\hat{\mathcal{E}}_{r,R}}{2h_z}\left(\psi_{11} + \psi_{1-1}\right) + \frac{iv\sqrt{2}\hat{k}_x}{h_z}\psi_{00},\\
\hat{\mathcal{E}}_{r,R}\left(\psi_{11} - \psi_{1-1}\right) &= 2h_z\left(\psi_{11} + \psi_{1-1}\right) - iv\sqrt{2}\hat{P}_x\left(\hat{\mathcal{E}}_{r,R}^{-1}\frac{iv}{\sqrt{2}}\hat{P}_x\left(\psi_{11} - \psi_{1-1}\right)\right),\\
g\delta(\mathbf{r})\partial_r(r\psi_{00}) &= -i\sqrt{2}v\hat{k}_x\left(\psi_{11} + \psi_{1-1}\right) + \hat{\mathcal{E}}_{r,R}\psi_{00}.
\end{aligned}$$

These equations are strongly coupled and are very difficult to solve, but a simplification occurs if solution is sought at the origin of the center of mass coordinate

system $\mathbf{R} = 0$, where only the relative motion is considered. To make additional progress, I will make use of the commutation relation

$$\left[\hat{P}_x, \hat{\mathcal{E}}_{r,R}^{-1}\right] = 0,$$

which is derived in Appendix XI.

Starting from the set of three equations above, substituting the term $(\psi_{11} - \psi_{1-1})$ from first row into the second row and using the vanishing derivatives involving $\hat{P}_x$, converts the second row into the expression

$$\left(\frac{\hat{\mathcal{E}}_{r,R}^2}{2h_z} - 2h_z\right)(\psi_{11} + \psi_{1-1}) \;\; = \;\; -\frac{\hat{\mathcal{E}}_{r,R}}{h_z} i\sqrt{2} v \hat{k}_x \psi_{00},$$

which can immediately be written as

$$(\psi_{11} + \psi_{1-1}) = -iv2\sqrt{2}\left(\hat{\mathcal{E}}_{r,R}^2 - 4h_z^2\right)^{-1} \hat{\mathcal{E}}_{r,R} \hat{k}_x \psi_{00}$$

Finally, I can substitute $(\psi_{11} + \psi_{1-1})$ into the third row of the last set of equations to produce the differential equation

$$-4v^2\hat{k}_x^2\left(\hat{\mathcal{E}}_{r,R}^2 - 4h_z^2\right)^{-1} \hat{\mathcal{E}}_{r,R}\psi_{00} + \hat{\mathcal{E}}_{r,R}\psi_{00} = g\delta(\mathbf{r})\partial_r(r\psi_{00}).$$

This completes the derivation of the differential equation for $\psi_{00} = \psi_{00}(\mathbf{r}, \mathbf{R} = \mathbf{0})$.

6.9 Appendix IX: Derivation of Eq. (3.42) at Chapter III

In this Appendix, I provide the derivation of Eq. (3.42) from Eq. (3.37). A substitution of the Laguerre polynomials into Eq. (3.37) leads to

$$\begin{aligned} -\frac{m\omega\sqrt{\pi}}{4\sqrt{2}a_s\zeta^{3/2}} = B_- \left[\frac{\partial}{\partial r}\left(re^{-\zeta r^2}\sum_{p=0}^{\infty}\frac{L_p^{(1/2)}(2\zeta r^2)}{2p-\nu_-}\right)\right]\Bigg|_{r\to 0} + ... \\ ... + B_+ \left[\frac{\partial}{\partial r}\left(re^{-\zeta r^2}\sum_{p=0}^{\infty}\frac{L_p^{(1/2)}(2\zeta r^2)}{2p-\nu_+}\right)\right]\Bigg|_{r\to 0}, \end{aligned} \tag{6.8}$$

where I used the relation

$$L_n^{(1/2)}(0) = \frac{(n+1/2)!}{n!(1/2)!}.$$

I redefine the argument of Laguerre polynomials in terms of a new variable $x^2 = 2\zeta r^2$ to rewrite the expression above as

$$-\frac{2m\omega\sqrt{\pi}}{4\sqrt{2}a_s\zeta^{3/2}} = B_- \left[\frac{\partial}{\partial x}\left(xe^{-x^2/2}\sum_{p=0}^{\infty}\frac{L_p^{(1/2)}(x^2)}{p-\nu_-/2}\right)\right]\Bigg|_{x\to 0} + ... \\ ... + B_+ \left[\frac{\partial}{\partial x}\left(xe^{-x^2/2}\sum_{p=0}^{\infty}\frac{L_p^{(1/2)}(x^2)}{p-\nu_+/2}\right)\right]\Bigg|_{x\to 0}. \tag{6.9}$$

Next, I introduce the useful integral representation [18]

$$\frac{1}{p-\nu_\pm/2} = \int_0^\infty \frac{dy}{(1+y)^2}\left(\frac{y}{1+y}\right)^{p-\nu_\pm/2-1},$$

for the purpose of making use of a special property of Laguerre polynomials described below. Using the integral just described in Eq. (6.9) gives

$$\sum_{p=0}^{\infty}\frac{L_p^{(1/2)}(x^2)}{p-\nu_\pm/2} = \sum_{p=0}^{\infty}\int_0^\infty \frac{dy}{(1+y)^2}\left(\frac{y}{1+y}\right)^{p-\nu_\pm/2-1} L_p^{(1/2)}(x^2),$$

which can be evaluated with the aid of the special property of Laguerre polynomials

$$\sum_{p=0}^{\infty} L_p^{(1/2)}(x)z^p = (1-z)^{-3/2}\exp\left(\frac{xz}{z-1}\right).$$

All these substitutions lead to the result

$$\begin{aligned}\sum_{p=0}^{\infty}\frac{L_p^{(1/2)}(x^2)}{p-\nu_\pm/2} &= \int_0^\infty \frac{dy}{\sqrt{1+y}}e^{-yx^2}\left(\frac{y}{1+y}\right)^{-\nu_\pm/2-1} \\ &= \Gamma(-\nu_\pm/2)F(-\nu_\pm/2,3/2,x^2),\end{aligned}$$

where $\Gamma(z)$ is the Gamma function and $F(z,3/2,x^2)$ is the confluent hypergeometric function. In the asymptotic limit of $x\to 0$,

$$\lim_{x\to 0}\Gamma(-\nu_\pm/2)F(-\nu_\pm/2,3/2,x^2) = -\sqrt{\pi}\left(\frac{2\Gamma(-\nu_\pm/2)}{\Gamma(-\nu_\pm/2-1/2)} - \frac{1}{x} + O(x)\right),$$

which can be used in Eq. (6.8) to obtain the equation for the bound state energy as

$$\frac{\sqrt{2}}{a_s\sqrt{m\omega}} = B_-\frac{\Gamma(-\nu_-/2)}{\Gamma(-\nu_-/2-1/2)} + B_+\frac{\Gamma(-\nu_+/2)}{\Gamma(-\nu_+/2-1/2)},$$

which is the desired result of my derivation.

6.10 Appendix X: Derivation of Eq. (3.37) in Chapter III

In this appendix, I discuss the derivation of the matrix element in Eq. (3.37) described in chapter III.

The second derivative of the wave functions $\phi_k(\mathbf{r})$ of the harmonic oscillator in the relative coordinates is

$$\partial^2_{r_x}\phi_k(\mathbf{r}) = N_n 2\zeta e^{-\zeta r^2}\left[8x^2\zeta L^{(5/2)}_{n-2}(2\zeta r^2) + (8x^2\zeta - 2)L^{(3/2)}_{n-1}(2\zeta r^2) + (2x^2\zeta - 1)L^{(1/2)}_{n}(2\zeta r^2)\right],$$

where $\zeta = m\omega/4$.

Projecting the second derivative above on the wavefunction $\phi^*_a(\mathbf{r})$ and integrating over real space gives

$$\int d\mathbf{r}\phi^*_a(r)\partial^2_{r_x}\phi_n(r) =$$

$$N_n^2 4\pi(2\zeta)\int_0^\infty r^2 e^{-2\zeta r^2}L^{(1/2)}_a(2\zeta r^2)\left[\frac{\zeta r^2}{3}\left(8L^{(5/2)}_{n-2}(2\zeta r^2) + 8L^{(3/2)}_{n-1}(2\zeta r^2) + 2L^{(1/2)}_{n}(2\zeta r^2)\right) - ... \right.$$
$$\left. ... - \left(2L^{(3/2)}_{n-1}(2\zeta r^2) + L^{(1/2)}_{n}(2\zeta r^2)\right)\right] dr,$$

where I used spherical coordinates $x = r\sin\theta\cos\phi$, $y = r\sin\theta\sin\phi$, $z = r\cos\theta$ performed angular integrals of the type

$$\int_0^\pi \sin^2\theta d\cos\theta \int_0^{2\pi}\cos^2\phi d\phi = \frac{4\pi}{3}.$$

Changing variables in the projection above using the relation $2\zeta r^2 = x$ gives an expression for the right hand side of the type

$$2\pi\frac{N_n^2}{\sqrt{2\zeta}}\left(\int_0^\infty x^{3/2}e^{-x}L^{(1/2)}_a(x)\left[\frac{4}{3}L^{(5/2)}_{n-2}(x) + \frac{4}{3}L^{(3/2)}_{n-1}(x) + \frac{1}{3}L^{(1/2)}_{n}(x)\right] - ... \right.$$
$$\left. ... - \int_0^\infty x^{1/2}e^{-x}L^{(1/2)}_a(x)\left[2L^{(3/2)}_{n-1}(x) + L^{(1/2)}_{n}(x)\right]\right).$$

In this expression there are five different types of integrals that need to be evaluated, namely

$$
\begin{aligned}
I_1 &= \int_0^\infty x^{3/2} e^{-x} L_n^{(5/2)}(x) L_m^{(1/2)}(x) dx \quad , \\
I_2 &= \int_0^\infty x^{3/2} e^{-x} L_n^{(3/2)}(x) L_m^{(1/2)}(x) dx \quad , \\
I_3 &= \int_0^\infty x^{3/2} e^{-x} L_n^{(1/2)}(x) L_m^{(1/2)}(x) dx \quad , \\
I_4 &= \int_0^\infty x^{1/2} e^{-x} L_n^{(3/2)}(x) L_m^{(1/2)}(x) dx \quad , \\
I_5 &= \int_0^\infty x^{1/2} e^{-x} L_n^{(1/2)}(x) L_m^{(1/2)}(x) dx \quad .
\end{aligned}
$$

The last integral I_5 can be evaluated using the orthogonality condition of generalized Laguerre polynomials

$$
I_5 = \int_0^\infty x^{1/2} e^{-x} L_n^{(1/2)}(x) L_m^{(1/2)}(x) dx = \frac{\Gamma(m+3/2)}{m!} \delta_{n,m} = \frac{(m+1/2)!}{m!} \delta_{m,n},
$$

while to evaluate the other integrals, it is necessary to utilize several recurrence properties of the the Laguerre polynomials, such as,

$$
\begin{aligned}
L_n^{(\alpha+1)}(x) &= \sum_{j=0}^{n} L_j^{(\alpha)}(x) \\
L_n^{(\alpha)}(x) &= L_n^{(\alpha+1)}(x) - L_{n-1}^{(\alpha+1)}(x) \\
\frac{d}{dx} L_n^{(k)}(x) &= x^{-1} \left(n L_n^{(k)}(x) - (n+k) L_{n-1}^{(k)}(x) \right).
\end{aligned}
$$

With these relations at hand all the I_i integrals can be evaluated. The first integral becomes

$$
I_1 = \int_0^\infty x^{3/2} e^{-x} L_{n-2}^{(5/2)}(x) L_a^{(1/2)}(x) dx = \sum_{i=0}^{n-2} \left(\frac{\Gamma(i+5/2)}{i!} \delta_{i,a} - \frac{\Gamma(i+5/2)}{i!} \delta_{i,a-1} \right),
$$

while the second integral takes the form

$$
I_2 = \int_0^\infty x^{3/2} e^{-x} L_{n-1}^{(3/2)}(x) L_a^{(1/2)}(x) dx = \frac{\Gamma(n+3/2)}{(n-1)!} \delta_{n-1,a} - \frac{\Gamma(n+3/2)}{(n-1)!} \delta_{n-1,a-1}.
$$

An evaluation of the third type of integral can also be performed to give

$$I_3 = \int_0^\infty x^{3/2} e^{-x} L_n^{(1/2)}(x) L_a^{(1/2)}(x) dx = \frac{\Gamma(n+5/2)}{n!}\delta_{n,a} + ... \\ ... - \frac{\Gamma(n+5/2)}{n!}\delta_{a,n-1} - \frac{\Gamma(n+3/2)}{(a-1)!}\delta_{a-1,n} + \frac{\Gamma(a+3/2)}{(a-1)!}\delta_{a-1,n-1},$$

and, similarly, performing the fourth and fifth kinds of integrals produce the following results

$$I_4 = \int_0^\infty x^{1/2} e^{-x} L_{n-1}^{(3/2)}(x) L_a^{(1/2)}(x) dx = \sum_{i=0}^{n-1} \frac{\Gamma(a+3/2)}{a!}\delta_{a,i},$$

$$I_5 = \int_0^\infty x^{1/2} e^{-x} L_n^{(1/2)}(x) L_a^{(1/2)}(x) dx = \frac{\Gamma(a+3/2)}{a!}\delta_{n,a}.$$

In the limit where the spin orbit coupling is small in comparison to adjacent energy levels of the harmonic oscillator, the coefficients coming from cross-terms can be neglected. Adding all the contributions from the projection integrals described above leads to an infinite set of linearly coupled equations between the coefficients c_a and various c_p

$$c_a \left[(\epsilon_a - E_u) + 4\frac{2\pi N_a^2}{\sqrt{2\zeta}} \frac{v^2}{\epsilon_a - E_u} \left(\frac{1}{3}\frac{\Gamma(a+5/2)}{a!} - \frac{\Gamma(a+3/2)}{a!} - \frac{\Gamma(a+3/2)}{(a-1)!} \right) \right] = ... \\ ... - \frac{4\pi}{m} a_s \phi_n^*(\mathbf{0}) \left[\frac{\partial}{\partial r} \left(r \sum_{p=0}^{\infty} c_p \phi_p(\mathbf{r}) \right) \right] \Bigg|_{r\to 0},$$

which can be reorganized as

$$c_a \left[(\epsilon_a - E_u) + 4\frac{2\zeta v^2}{(\epsilon_a - E_u)} \left(\frac{1}{3}\frac{\Gamma(a+5/2)}{\Gamma(a+3/2)} - 1 - a \right) \right] = ... \\ ... - \frac{4\pi}{m} a_s \phi_n^*(\mathbf{0}) \left[\frac{\partial}{\partial r} \left(r \sum_{p=0}^{\infty} c_p \phi_p(\mathbf{r}) \right) \right] \Bigg|_{r\to 0}.$$

Making use of the relations involving the Gamma function

$$\Gamma(a+1/2) = \frac{(2n-1)!!}{2^n}\sqrt{\pi} \quad \text{and} \quad \frac{\Gamma(a+5/2)}{\Gamma(a+3/2)} = \frac{2a+1}{2}$$

into the previous equation for c_a, yields

$$c_a \left[(\epsilon_a - E_u) - \frac{m\omega v^2}{\epsilon_a - E_u} \left(\frac{4a}{3} + \frac{5}{3} \right) \right] = - \frac{4\pi}{m} a_s \phi_n^*(\mathbf{0}) \left[\frac{\partial}{\partial r} \left(r \sum_{p=0}^{\infty} c_p \phi_p(\mathbf{r}) \right) \right] \Bigg|_{r\to 0},$$

which when reorganized gives the desired result

$$c_a = -\frac{4\pi a}{m}\phi_a^*(\mathbf{0})\left[\frac{\partial}{\partial r}\left(r\sum_{p=0}^{\infty}c_p\phi_p(\mathbf{r})\right)\right]\Bigg|_{r\to 0}\left(\frac{\epsilon_a - E_u}{(\epsilon_a - E_u)^2 - \frac{mv^2\omega}{3}(4a+5)}\right).$$

This is the relation displayed in Eq. (3.38), while the previous expression for c_a is the relation displayed in Eq. (3.37).

6.11 Appendix XI: Derivation of Commutator Relation

In this appendix, I will outline the derivation of the commutation relation $[\partial_{r_x}, \hat{\mathcal{E}}_r^{-1}] = 0$. This commutation relation above was neccessary to obtain the differential equation described in Eq. (3.43).

Let me begin the derivation by noting the simpler commutation relation between the center of mass momentum component $\mathbf{P}_x$ and the kinetic energy term written in center of mass and relative coordinates: $\left[\hat{P}_x, \hat{\mathcal{E}}_{r,R}\right] = 0$. Let me apply the commutation that I want to prove to the harmonic oscillator eigenfunctions $\phi(\mathbf{r}, \mathbf{R})$ such that

$$\begin{aligned}\left[\hat{P}_x, \hat{\mathcal{E}}_{r,R}^{-1}\right]\phi(\mathbf{r},\mathbf{R}) &= \\ \left(\hat{P}_x\hat{\mathcal{E}}_{r,R}^{-1} - \hat{\mathcal{E}}_{r,R}^{-1}\hat{P}_x\right)\phi(\mathbf{r},\mathbf{R}) &= \\ \left(\hat{P}_x\int_0^{\infty} ds\, e^{-s\,\hat{\mathcal{E}}_{r,R}} - \int_0^{\infty} ds\, e^{-s\,\hat{\mathcal{E}}_{r,R}}\hat{P}_x\right)\phi(\mathbf{r},\mathbf{R}).\end{aligned}$$

Notice that in the last line I used a simple integral representation of the inverse operator $\hat{\mathcal{E}}_{r,R}$ since it is Hermitian, and thus the integral is well defined.

By performing an expansion of the exponential term used in the integral representation of the operator

$$\left(\int_0^\infty ds\, \left[\hat{P}_x, e^{-s\,\hat{\mathcal{E}}_{r,R}}\right]\right)\phi\left(\mathbf{r},\mathbf{R}\right) =$$

$$\left(\int_0^\infty ds\, \left[\hat{P}_x, 1 - s\hat{\mathcal{E}}_{r,R} + \frac{1}{2}s^2\hat{\mathcal{E}}_{r,R}^2 - ...\right]\right)\phi\left(\mathbf{r},\mathbf{R}\right) =$$

$$\left(\int_0^\infty ds\, \left(\underbrace{\left[\hat{P}_x, 1\right]}_{0} - s\underbrace{\left[\hat{P}_x, \hat{\mathcal{E}}_{r,R}\right]}_{0} + \frac{s^2}{2}\underbrace{\left[\hat{P}_x, \hat{\mathcal{E}}_{r,R}^2\right]}_{0} - ...\right)\right)\phi\left(\mathbf{r},\mathbf{R}\right) = 0,$$

it is now self-evident that the commutators inside the integral vanish order by order, thus leading to the final result

$$[\partial_{r_x}, \hat{\mathcal{E}}_r^{-1}] = 0,$$

which was used to obtain the differential equation described in Eq. (3.43).

- **Find the self-consistent equation. The last line returns the function f(k, K, , , , , .**

  xa →
  xb →
  xc →
  xd →
  h → **(Zeeman field along z)**
  hy → **(Zeeman field along y)**
  vR → **(Rashba type spin-orbit coupling)**
  vD → **(Dresselhaus type spin-orbit coupling)**
  px → **(Center of mass momentum along x)**
  py → **(Center of mass momentum along y)**
  kx → **(Relative momentum along x)**
  ky → **(Relative momentum along y)**
  ener → **(Kinetic energy −energy eigenvalue)**

  being the recoil energy.

In[1976]:=
```
Clear[xa, xb, xc, xd]
```

In[1977]:=
```
xa = xa /. Solve[(ener - 2 h) xa + (i (vR + vD)/Sqrt[2] px - (vD - vR)/Sqrt[2] py + i Sqrt[2] hy) xb +
    (-i Sqrt[2] (vR + vD) kx + Sqrt[2] (vD - vR) ky) xd == 0, xa][[1]]
```

In[1978]:=
```
xb = xb /. Solve[(-i (vR + vD)/Sqrt[2] px - (vD - vR)/Sqrt[2] py - i Sqrt[2] hy) xa +
    ener xb + (i (vR + vD)/Sqrt[2] px - (vD - vR)/Sqrt[2] py + i Sqrt[2] hy) xc == 0, xb][[1]]
```

In[1979]:=
```
xc = xc /. Solve[(-i (vR + vD)/Sqrt[2] px - (vD - vR)/Sqrt[2] py - i Sqrt[2] hy) xb +
    (ener + 2 h) xc + (-i Sqrt[2] (vR + vD) kx - Sqrt[2] (vD - vR) ky) xd == 0, xc][[1]]
```

In[1981]:=
```
FullSimplify[
  ((i Sqrt[2] (vR + vD) kx + Sqrt[2] (vD - vR) ky) xa + (i Sqrt[2] (vR + vD) kx - Sqrt[2] (vD - vR) ky) xc + ener xd) / xd]
```

Out[1981]=
$$-\left(\text{ener}^4 - \text{ener}^2\left(4\,h^2 + 4\,hy^2 + \left(4\,ky^2 + px^2 + py^2\right)vD^2 - 2\left(4\,ky^2 - px^2 + py^2\right)vD\,vR + \left(4\,ky^2 + px^2 + py^2\right)vR^2 + 4\,hy\,px\,(vD + vR) + 4\,kx^2\,(vD + vR)^2\right) + 4\left(ky\,py\,(vD - vR)^2 + 2\,hy\,kx\,(vD + vR) + kx\,px\,(vD + vR)^2\right)^2\right) \Big/ \left(\text{ener}\left(-\text{ener}^2 + 4\,h^2 + 4\,hy^2 + py^2\,(vD - vR)^2 + 4\,hy\,px\,(vD + vR) + px^2\,(vD + vR)^2\right)\right)$$

Figure 6.1: Computer code written in *Mathematica* with the purpose of finding the function $f(\mathbf{k}, \mathbf{K}, h_z, h_y, v_R, v_D, E)^{-1}$ defined in Appendix II.

- **This routine derives the expression for effective mass tensors and calculates the integrals. The expression in the derivative function is taken as the result of code at Appendix II. eb represents the energy eigenvalue. $t \to k^2/m$ represents the kinetic energy, which will be replaced after deriving the expressions. This method is messy, but I have chosen this method to see the whole expression, thus to avoid making clerical mistakes along the way. Also the integration is obviously faster comparing to numerical calculation of derivatives directly from expression.**

```
ener = t + px^2/(4 m) + py^2/(4 m) + pz^2/(4 m) - eb;
```

- **Derive the derivative with respect to energy eigenvalue (eb) at zero center of mass limit.**

```
FullSimplify[D[-(ener (-ener^2 + 4 h^2 + 4 hy^2 + py^2 (vD - vR)^2 + 4 hy px (vD + vR) + px^2 (vD + vR)^2))/
    (ener^4 - ener^2 (4 h^2 + 4 hy^2 + (4 ky^2 + px^2 + py^2) vD^2 - 2 (4 ky^2 - px^2 + py^2) vD vR +
        (4 ky^2 + px^2 + py^2) vR^2 + 4 hy px (vD + vR) + 4 kx^2 (vD + vR)^2) +
      4 (ky py (vD - vR)^2 + 2 hy kx (vD + vR) + kx px (vD + vR)^2)^2), eb] /. {px -> 0, py -> 0, pz -> 0}]
```

- **Derive the second derivative with respect to K_x (center-of-mass momentum) around zero center of mass limit.**

```
FullSimplify[D[-(ener (-ener^2 + 4 h^2 + 4 hy^2 + py^2 (vD - vR)^2 + 4 hy px (vD + vR) + px^2 (vD + vR)^2))/
    (ener^4 - ener^2 (4 h^2 + 4 hy^2 + (4 ky^2 + px^2 + py^2) vD^2 - 2 (4 ky^2 - px^2 + py^2) vD vR +
        (4 ky^2 + px^2 + py^2) vR^2 + 4 hy px (vD + vR) + 4 kx^2 (vD + vR)^2) +
      4 (ky py (vD - vR)^2 + 2 hy kx (vD + vR) + kx px (vD + vR)^2)^2), {px, 2}] /. {px -> 0, py -> 0, pz -> 0}]
```

- **Derive the second derivative with respect to K_y (center-of-mass momentum) around zero center of mass limit.**

```
FullSimplify[D[-(ener (-ener^2 + 4 h^2 + 4 hy^2 + py^2 (vD - vR)^2 + 4 hy px (vD + vR) + px^2 (vD + vR)^2))/
    (ener^4 - ener^2 (4 h^2 + 4 hy^2 + (4 ky^2 + px^2 + py^2) vD^2 - 2 (4 ky^2 - px^2 + py^2) vD vR +
        (4 ky^2 + px^2 + py^2) vR^2 + 4 hy px (vD + vR) + 4 kx^2 (vD + vR)^2) +
      4 (ky py (vD - vR)^2 + 2 hy kx (vD + vR) + kx px (vD + vR)^2)^2), {py, 2}] /. {px -> 0, py -> 0, pz -> 0}]
```

Figure 6.2: Mathematica code to find the effective mass tensors in Appendix VI, part 1.

- **These are the expressions after t was replaced with kinetic energy and scaled with recoil energy/momentum from above commands.**
  DerE → Derivative for eb
  DerPx → Derivative for K_x
  DerPy → Derivative for K_y

```
DerE[x_, y_, z_, hy_, hz_, v_, vD_, eb_] :=
 -(2 (eb - 2 (x^2 + y^2 + z^2))^2 (4 hy^2 + 4 hz^2 + 16 v^2 x^2 + 16 vD^2 y^2 - 2 (eb - 2 (x^2 + y^2 + z^2))^2)
      (-4 hy^2 - 4 hz^2 + (eb - 2 (x^2 + y^2 + z^2))^2) + 2 (eb - 2 (x^2 + y^2 + z^2))^2
      (64 hy^2 v^2 x^2 - 4 (hy^2 + hz^2 + 4 v^2 x^2 + 4 vD^2 y^2) (eb - 2 (x^2 + y^2 + z^2))^2 + (eb - 2 (x^2 + y^2 + z^2))^4) +
     (-4 hy^2 - 4 hz^2 + (eb - 2 (x^2 + y^2 + z^2))^2)
      (64 hy^2 v^2 x^2 - 4 (hy^2 + hz^2 + 4 v^2 x^2 + 4 vD^2 y^2) (eb - 2 (x^2 + y^2 + z^2))^2 + (eb - 2 (x^2 + y^2 + z^2))^4)) /
   (64 hy^2 v^2 x^2 - 4 (hy^2 + hz^2 + 4 v^2 x^2 + 4 vD^2 y^2) (eb - 2 (x^2 + y^2 + z^2))^2 + (eb - 2 (x^2 + y^2 + z^2))^4)^2
DerPx[x_, y_, z_, hy_, hz_, v_, vD_, eb_] :=
 (16 hy v (-eb + 2 (x^2 + y^2 + z^2)) (128 hy v^3 x^2 - 8 hy v (eb - 2 (x^2 + y^2 + z^2))^2)
      (64 hy^2 v^2 x^2 - 4 (hy^2 + hz^2 + 4 v^2 x^2 + 4 vD^2 y^2) (eb - 2 (x^2 + y^2 + z^2))^2 + (eb - 2 (x^2 + y^2 + z^2))^4) +
     (64 hy^2 v^2 x^2 - 4 (hy^2 + hz^2 + 4 v^2 x^2 + 4 vD^2 y^2) (eb - 2 (x^2 + y^2 + z^2))^2 + (eb - 2 (x^2 + y^2 + z^2))^4)^2
      (-4 hy^2 - 4 hz^2 + (eb - 2 (x^2 + y^2 + z^2))^2 + 2 (-eb + 2 (x^2 + y^2 + z^2)) (-eb + 2 (-2 v^2 + x^2 + y^2 + z^2))) +
     (-eb + 2 (x^2 + y^2 + z^2)) (-4 hy^2 - 4 hz^2 + (eb - 2 (x^2 + y^2 + z^2))^2)
      (2 (128 hy v^3 x^2 - 8 hy v (eb - 2 (x^2 + y^2 + z^2))^2)^2 - 4 (64 hy^2 v^2 x^2 - 4 (hy^2 + hz^2 + 4 v^2 x^2 + 4 vD^2 y^2)
           (eb - 2 (x^2 + y^2 + z^2))^2 + (eb - 2 (x^2 + y^2 + z^2))^4) (32 v^4 x^2 - 2 v^2 (eb - 2 (x^2 + y^2 + z^2))^2 -
           2 (hy^2 + hz^2 + 4 v^2 x^2 + 4 vD^2 y^2) (-eb + 2 (x^2 + y^2 + z^2)) + (-eb + 2 (x^2 + y^2 + z^2))^3))) /
   (64 hy^2 v^2 x^2 - 4 (hy^2 + hz^2 + 4 v^2 x^2 + 4 vD^2 y^2) (eb - 2 (x^2 + y^2 + z^2))^2 + (eb - 2 (x^2 + y^2 + z^2))^4)^3
DerPy[x_, y_, z_, hy_, hz_, v_, vD_, eb_] :=
 (-4 hy^2 - 4 hz^2 + (eb - 2 (x^2 + y^2 + z^2))^2 + 2 (-eb + 2 (x^2 + y^2 + z^2)) (-eb + 2 (-2 vD^2 + x^2 + y^2 + z^2))) /
   (64 hy^2 v^2 x^2 - 4 (hy^2 + hz^2 + 4 v^2 x^2 + 4 vD^2 y^2) (eb - 2 (x^2 + y^2 + z^2))^2 + (eb - 2 (x^2 + y^2 + z^2))^4) +
  ((-eb + 2 (x^2 + y^2 + z^2)) (-4 hy^2 - 4 hz^2 + (eb - 2 (x^2 + y^2 + z^2))^2)
      (32768 hy^2 v^2 vD^4 x^2 y^2 - 4 (64 hy^2 v^2 x^2 - 4 (hy^2 + hz^2 + 4 v^2 x^2 + 4 vD^2 y^2) (eb - 2 (x^2 + y^2 + z^2))^2 +
           (eb - 2 (x^2 + y^2 + z^2))^4) (32 vD^4 y^2 - 2 vD^2 (eb - 2 (x^2 + y^2 + z^2))^2 -
           2 (hy^2 + hz^2 + 4 v^2 x^2 + 4 vD^2 y^2) (-eb + 2 (x^2 + y^2 + z^2)) + (-eb + 2 (x^2 + y^2 + z^2))^3))) /
   (64 hy^2 v^2 x^2 - 4 (hy^2 + hz^2 + 4 v^2 x^2 + 4 vD^2 y^2) (eb - 2 (x^2 + y^2 + z^2))^2 + (eb - 2 (x^2 + y^2 + z^2))^4)^3
```

Figure 6.3: Mathematica code to find the effective mass tensors in Appendix VI, part 2.

- **These are the integration routines.**
  efmassx → Returns the effective mass tensor m_{xx}/m
  efmassy → Returns the effective mass tensor m_{yy}/m

```
dE[hy_, hz_, v_, vD_, eb_] := NIntegrate[DerE[x, y, z, hy, hz, v, vD, eb], {x, 0, 10000},
  {y, 0, 10000}, {z, 0, 10000}, Method → "MultidimensionalRule", AccuracyGoal → 6]
dPx[hy_, hz_, v_, vD_, eb_] := NIntegrate[DerPx[x, y, z, hy, hz, v, vD, eb], {x, 0, 10000},
  {y, 0, 10000}, {z, 0, 10000}, Method → "MultidimensionalRule", AccuracyGoal → 6]
dPy[hy_, hz_, v_, vD_, eb_] := NIntegrate[DerPy[x, y, z, hy, hz, v, vD, eb], {x, 0, 10000},
  {y, 0, 10000}, {z, 0, 10000}, Method → "MultidimensionalRule", AccuracyGoal → 6]
efmassx[hy_, hz_, v_, vD_, eb_] := -2 dE[hy, hz, v, vD, eb] / dPx[hy, hz, v, vD, eb]
efmassy[hy_, hz_, v_, vD_, eb_] := -2 dE[hy, hz, v, vD, eb] / dPy[hy, hz, v, vD, eb]
```

Figure 6.4: Mathematica code to find the effective mass tensors in Appendix VI, part 3.

REFERENCES

[1] R. A. Williams, M. C. Beeler, L. J. LeBlanc, K. Jiménez-García, I. B. Spielman, Raman-Induced Interactions in a Single-Component Fermi Gas Near an *s*-Wave Feshbach Resonance, Phys. Rev. Lett. **111**, 095301 (2013).

[2] C. Chin et al., Feshbach resonances in ultracold gases, Reviews of Modern Physics **82**, 1225 (2010).

[3] M. Greiner, C. A. Regal, D. S. Jin, Emergence of a molecular BoseEinstein condensate from a Fermi gas, Nature **426**, 537 (2003).

[4] I. Bloch, J. Dalibard, W. Zwerger, Many-body physics with ultracold gases, Reviews of Modern Physics **80**, 885 (2008).

[5] Y-J. Lin, K. Jiménez-García, I. B. Spielman, Spin-orbit-coupled Bose-Einstein condensates, Nature **471**, 83 (2011).

[6] P. Wang et al., Spin-orbit coupled degenerate Fermi gases, Phys. Rev. Lett. **109**, 095301 (2012).

[7] Yu A. Bychkov, E. I. Rashba, Oscillatory effects and the magnetic susceptibility of carriers in inversion layers, J. Phys. C: Solid State Phys. **17**, 6039 (1984).

[8] G. Dresselhaus, Spin-Orbit Coupling Effects in Zinc Blende Structures, Phys. Rev. **100**, 580 (1955).

[9] M. Z. Hasan, C. L. Kane, Colloquium: topological insulators. Reviews of Modern Physics **82**, 3045 (2010).

[10] X.-L. Qi, S.-C. Zhang, Topological insulators and superconductors, Reviews of Modern Physics **83**, 1057 (2011).

[11] Y.-J. Lin et al., Synthetic magnetic fields for ultracold neutral atoms, Nature **462**, 628 (2009).

[12] M. Chapman, C.A.R. Sá de Melo, Atomic physics: Atoms playing dress-up, Nature **471**, 41 (2011).

[13] I. B. Spielman, private communication.

[14] D. L. Campbell, G. Juzelinas, I. B. Spielman, Realistic Rashba and Dresselhaus spin-orbit coupling for neutral atoms, Phys. Rev. A **84**, 025602 (2011).

[15] C. A. Regal, JILA, Doctoral Thesis (2006).

[16] S. D. Sarma, M. Freedman, C. Nayak, Topologically Protected Qubits from a Possible Non-Abelian Fractional Quantum Hall State, Phys. Rev. Lett. **94**, 166802 (2005).

[17] Z.-Q. Yu, H. Zhai, Spin-Orbit Coupled Fermi Gases across a Feshbach Resonance, Phys. Rev. Lett. **107**, 195305 (2011) .

[18] T. Busch, B.-G. Englert, K. Rzaewski, M. Wilkens, Two Cold Atoms in a Harmonic Trap, Foundations of Physics, **28**, 549 (1998).

[19] S. N. Bose, Plancks law and the light quantum hypothesis, Z. Phys **26** (1924).

[20] A. Einstein, Quantentheorie des einatomigen idealen Gases, Preuss, Akad. Wiss. Berlin Ber. **22**, 261 (1924).

[21] M.P.A. Fisher et al., Boson localization and the superfluid-insulator transition, Phys. Rev. B **40**, 546 (1989).

[22] A. J. Leggett, Cooper pairing in spin-polarized fermi systems, J. Phys. Colloq. **41**, 19 (1980).

[23] P. Nozières, S. Schmitt-Rink, Bose condensation in an attractive fermion gas: From weak to strong coupling superconductivity, Journal of Low Temperature Physics **59**, 195 (1985).

[24] C.A.R. Sá De Melo, M. Randeria, J. R. Engelbrecht, Crossover from BCS to Bose superconductivity: Transition temperature and time-dependent Ginzburg-Landau theory, Phys. Rev. Lett. **71**, 3202 (1993).

[25] C. J. Myatt et al., Production of two overlapping Bose-Einstein condensates by sympathetic cooling, Phys. Rev. Lett. **78**, 586 (1997).

[26] I. J. Bonalde et al., Spin-polarized Hydrogen in a High Field Trap: Towards a Two-Component Bose Gas, J. Low Temp. Phys. **113**, 211 (1998).

[27] X. Zhang, M. Bishof, S. L. Bromley, C. V. Kraus, M. S. Safronova, P. Zoller, A. M. Rey, J. Ye, Spectroscopic observation of SU(N)-symmetric interactions in Sr orbital magnetism, Science **345**, 1467 (2014).

[28] J.-Y. Zhang et al., Collective dipole oscillations of a spin-orbit coupled Bose-Einstein condensate, Phys. Rev. Lett. **109**, 115301 (2012).

[29] T.-L. Ho, S. Zhang, Bose-Einstein Condensates with Spin-Orbit Interaction, Phys. Rev. Lett. **107**, 150403 (2011).

[30] Y. Li, L. P. Pitaevskii, S. Stringari, Quantum tri-criticality and phase transitions in spin-orbit coupled Bose-Einstein condensates, Phys. Rev. Lett. **108**, 225301 (2012).

[31] T. Ozawa and G. Baym, Condensation Transition of Ultracold Bose Gases with Rashba Spin-Orbit Coupling, Phys. Rev. Lett. **110**, 085304 (2013).

[32] S.-C. Ji, J.-Y. Zhang, L. Zhang, Z.-D. Du, W. Zheng, Y.-J. Deng, H. Zhai, S. Chen, J.-W. Pan, Experimental Determination of the Finite-Temperature Phase Diagram of a Spin-Orbit Coupled Bose Gas, Nature Physics **10**, 314 (2014).

[33] Gong, Ming, S. Tewari, C. Zhang, BCS-BEC crossover and topological phase transition in 3D spin-orbit coupled degenerate Fermi gases, Phys. Rev. Lett. **107**, 195303 (2011).

[34] Z.-Q. Yu, H. Zhai, Spin-orbit coupled Fermi gases across a Feshbach resonance, Phys. Rev. Lett. **107**, 195305 (2011).

[35] H. Hu et al., Probing anisotropic superfluidity in atomic Fermi gases with Rashba spin-orbit coupling, Phys. Rev. Lett. **107**, 195304 (2011).

[36] L. Han, C.A.R. Sá de Melo. Evolution from BCS to BEC superfluidity in the presence of spin-orbit coupling, Phys. Rev. A **85**, 011606 (2012).

[37] K. Seo, L. Han, C.A.R. Sá de Melo, Emergence of Majorana and Dirac particles in ultracold fermions via tunable interactions, spin-orbit effects, and Zeeman fields, Phys. Rev. Lett. **109**, 105303 (2012).

[38] P. Wang et al., Spin-orbit coupled degenerate Fermi gases, Phys. Rev. Lett. **109**, 095301 (2012).

[39] L. W. Cheuk et al., Spin-injection spectroscopy of a spin-orbit coupled Fermi gas, Phys. Rev. Lett. **109**, 095302 (2012).

[40] Z. Fu et al., Production of Feshbach molecules induced by spin-orbit coupling in Fermi gases, Nature Physics **10**, 110 (2014).

[41] C.A.R. Sá de Melo et al., When fermions become bosons: Pairing in ultracold gases, Physics Today **61**, 45 (2008).

[42] M. Iavarone, G. Karapetrov, A. E. Koshelev, W. K. Kwok, G. W. Crabtree, D. G. Hinks, W. N. Kang, E.-M. Choi, H. J. Kim, H.-J. Kim, S. I. Lee, Two-Band Superconductivity in MgB_2, Phys. Rev. Lett. **89**, 187002 (2002).

[43] Y. Maeno, T. M. Rice, M. Sigrist, The intriguing superconductivity of strontium ruthenate, Physics Today **54**, 42 (2001).

[44] Y. Kamihara et al., Iron-based layered superconductor: LaOFeP, Journal of the American Chemical Society **128**, 10012 (2006).

[45] W. Pauli, The connection between spin and statistics, Phys. Rev. **58**, 716 (1940).

[46] G. Cardano, *The Rules of Algebra (Ars Magna)* Dover, (2007).

[47] I. Y. Pomeranchuk, Zh. Eskp. Teor. Fiz.**35**, 524 (1958).

[48] J. M. Luttinger, Fermi surface and some simple equilibrium properties of a system of interacting fermions, Phys. Rev. **119**, 1153 (1960).

[49] I. M. Lifshitz, Zh. Eksp. Teor. Fiz. **38**, 1569 (1960).

VITA

Doga Murat Kurkcuoglu was born in Ordu, Turkey. After finishing the high-school in Samsun in Ataturk Anatolian High-School, he started Physics program at Marmara University in Istanbul. There, he enjoyed many physics discussions with Zikri Altun as well as MIT OCW, which he also followed MIT syllabus along with the program at Marmara University. He enjoyed many summer schools in theoretical physics at Feza Gursey Institute, just before graduating from Marmara University. He then started PhD School at Georgia Institute of Technology in 2009, and started working with Carlos Sá de Melo in 2010. Along with the PhD in theoretical physics at Georgia Insitute of Technology, he completed minor program in Computer Science. His hobbies are rock climbing, nature sports and violin.